Method Development for Higher Order Transitions in Homonuclear Diatomic Molecules

Wilfrid S. Somogyi

University College London

Department of Physics and Astronomy

Submitted to University College London (UCL) in partial fulfilment of the requirements for the award of the degree of Doctor of Philosophy.

Primary supervisor: Sergey N. Yurchenko

Secondary supervisor: Jonathan P. Tennyson

Examiners:
Professor Stephen Hogan

Professor David Tew

Thesis submission date: 22nd March 2025

Declaration

I, Wilfrid S. Somogyi, confirm that the work presented in this thesis is my own. Where information has been derived from other sources, I confirm that this has been indicated in the thesis.

Wilfrid S. Somogyi
London, United Kingdom
22nd March 2025

Abstract

The central aim of this thesis is to develop a new computational methodology for calculating linestrengths, Einstein coefficients and absorption intensities of electric quadrupole and magnetic dipole transition moments in diatomic molecules. The system chosen to demonstrate this methodology is the $^{16}O_2$ molecule, and specifically the atmospheric and infrared transitions.

A unified treatment of the electric quadrupole and magnetic dipole moments has been developed *a priori* from the molecular Hamiltonian in the Born-Oppenheimer approximation. Using this treatment, expressions for the line strengths, Einstein coefficients and absorption intensities for transitions generated by these multipole interactions have been derived and implemented in computer code as an extension to the Duo program. This implementation has been tested and demonstrated for a range of homonuclear and heteronuclear diatomic molecules.

Using symmetry properties of these transition moments, and a reduction to the irreducible tensor representation, straightforward expressions have been given for the transformation from the basis of Abelian symmetry groups to the of Hund's case (a) basis. A set of potential energy, quadrupole moment, electronic angular momentum and spin-orbit coupling curves have been produced using high-level electronic structure calculations for seven electronic states of $^{16}O_2$. A property-based procedure for diabatising electronic structure properties has been presented and successfully used to transform electronic structure properties of some highly excited Π states of molecular oxygen to the adiabatic representation. This is a key step in accurately reproducing the complicated rotational structure of the electric quadrupole absorption bands.

This diabatic model has subsequently been used to produce the first complete rovibronic line list for transitions between the three lowest lying electronic states ($X\,^3\Sigma_g^-$, $a\,^1\Delta_g$, and $b\,^1\Sigma_g^+$) using the extended ExoMol methodology for higher order transition moments. This line list has been produced through empirical refinement of the spectroscopic model and is widely applicable for a range of temperatures and in the wavenumber range 0–20 000 cm^{-1}.

Impact Statement

Molecular oxygen plays an important role across many areas of physics. The absorption characteristics of $^{16}O_2$ are crucial for atmospheric modelling and remote sensing, and hence for characterising weather and climate patterns and monitoring greenhouse gases in Earth's atmosphere. Beyond our own atmosphere, molecular oxygen is also a key target molecule for exoplanetary retrievals, acting as a bio-signature for habitable planets and helping to understand the geochemistry of hot rocky exoplanets. Results published during the course of this doctoral study have already been used in exoplanetary retrievals to characterise the atmospheres of the exoplanets WASP 39b and HAT-P-26 b [1, 2] and to model oxygen-rich AGB stars [3]. Further work presented in this thesis provides a complete spectroscopic model for the infrared and atmospheric bands of $^{16}O_2$, along with an associated line list. This line list will facilitate the detection of molecular oxygen in exoplanetary atmospheres and enable a deeper understanding of the geophysical and geochemical process that govern their formation and dynamics. It also allows for the possibility of detecting abiotic sources of $^{16}O_2$ and establishing the existence of life beyond our own solar system.

The general framework for calculating the electric quadrupole and magnetic dipole absorption spectra of diatomic molecules developed as part of this thesis will also find general utility in producing similar line lists for other molecules. This is especially true for homonuclear diatomic molecules, where these higher-order interaction mechanisms dominate, but is also relevant for heteronuclear diatomic molecules with a strongly asymmetric electron distribution. The software developed and implemented within the Duo program may be used to provide new insight into the infrared absorption and emission spectra of molecules such as S_2, N_2 and C_2, which are also important molecules for exoplanetary studies.

The electronic structure calculations for $^{16}O_2$ presented in this thesis represent the most accurate and complete *ab initio* calculation of the permanent quadrupole moment to date, and the first prediction of other permanent and transition quadrupole moments for excited electronic states. These results will be of interest to the chemical community as they play an important role the molecular dynamics and chemical reactions. The spin-orbit interaction be-

tween the lowest lying electronic states also plays a role in oxidative metabolic processes of living organisms and in enzymatic reaction pathways. Better understanding the magnetic and electric properties of this molecules will help to more accurately model these biological processes.

Acknowledgements

I would like to express my sincere gratitude to my supervisor, Professor Sergey Yurchenko. He has been an inexhaustable source of wisdom, enthusiasm, and support over the course of the last five years. Without his dedication none of the work contained herein would have been possible. I would like also to thank all the members of ExoMol who accompanied me on this journey. I only wish I could have spent more time with them.

My parents Emma and Arnold, my sister Poppy, and all my family are owed a great debt of gratitude for the confidence they have placed in me. Their love and encouragement has been invaluable throughout my academic journey. Paddy, my beloved cat, has been my friend through many early mornings, and made the writing process incalculably more bearable.

Above all, I would like to thank my partner Kerry, who has been there with me at every step of this journey. My ability to complete this doctorate was due in no small part to her love, reassurance, and infinite patience.

UCL Research Paper Declaration Form: referencing the doctoral candidates own published work(s)

1. **1. For a research manuscript that has already been published** (if not yet published, please skip to section 2)**:**

   (a) **What is the title of the manuscript?**
   Calculation of electric quadrupole linestrengths for diatomic molecules: Application to the H_2, CO, HF, and O2 molecules

   (b) **Please include a link to or doi for the work:**
   10.1063/5.0063256

   (c) **Where was the work published?**
   Journal of Physical Chemistry

   (d) **Who published the work?**
   AIP Publishing

   (e) **When was the work published?**
   December 2021

   (f) **List the manuscript's authors in the order they appear on the publication:**
   Somogyi, Wilfrid and Yurchenko, Sergey N. and Yachmenev, Andrey

   (g) **Was the work peer reviewd?**
   Yes

   (h) **Have you retained the copyright?**
   Yes

   (i) **Was an earlier form of the manuscript uploaded to a preprint server (e.g. medRxiv)? If Yes, please give a link or doi**
   Yes, https://arxiv.org/abs/2111.05840
   If No, please seek permission from the relevant publisher and check the box next to the below statement:

   ☐ *I acknowledge permission of the publisher named under 1d to include in this thesis portions of the publication named as included in 1c.*

2. **For a research manuscript prepared for publication but that has not yet been published** (if already published, please skip to section 3)**:**

   (a) **What is the current title of the manuscript?**

(b) **Has the manuscript been uploaded to a preprint server 'e.g. medRxiv'?**
If 'Yes', please please give a link or doi:

(c) **Where is the work intended to be published?**

(d) **List the manuscript's authors in the intended authorship order:**

(e) **Stage of publication:**

3. **For multi-authored work, please give a statement of contribution covering all authors** (if single-author, please skip to section 4)**:**
Somogyi, Wilfrid: Writing, derivations, programmatic implementation, *ab initio* calculations for O_2 and HF, line list calculations and analysis
Yurchenko, Sergey N.: guidance, writing
Yachmenev, Andrey: guidance, *ab initio* calculations for CO

4. **In which chapter(s) of your thesis can this material be found?**
Chapters 2 and 4

e-Signatures confirming that the information above is accurate (this form should be co-signed by the supervisor/ senior author unless this is not appropriate, e.g. if the paper was a single-author work)**:**

Candidate:
Wilfrid Somogyi
Date: 15th October 2024

Supervisor :
Sergey Yurchenko
Date: 15th October 2024

UCL Research Paper Declaration Form: referencing the doctoral candidates own published work(s)

1. **1. For a research manuscript that has already been published** (if not yet published, please skip to section 2)**:**

   (a) **What is the title of the manuscript?**
   An ab initio spectroscopic model of the molecular oxygen atmospheric and infrared bands

   (b) **Please include a link to or doi for the work:**
   10.1039/D4CP02619E

   (c) **Where was the work published?**
   Physical Chemistry Chemical Physics

   (d) **Who published the work?**
   Royal Society of Chemistry

   (e) **When was the work published?**
   October 2024

   (f) **List the manuscript's authors in the order they appear on the publication:**
   Somogyi, Wilfrid and Yurchenko, Sergey N. and Kim, Gap-Sue

   (g) **Was the work peer reviewd?**
   Yes

   (h) **Have you retained the copyright?**
   Yes

   (i) **Was an earlier form of the manuscript uploaded to a preprint server (e.g. medRxiv)? If Yes, please give a link or doi**
   No
   If No, please seek permission from the relevant publisher and check the box next to the below statement:

   ☒ *I acknowledge permission of the publisher named under 1d to include in this thesis portions of the publication named as included in 1c.*

2. **For a research manuscript prepared for publication but that has not yet been published** (if already published, please skip to section 3)**:**

   (a) **What is the current title of the manuscript?**

(b) **Has the manuscript been uploaded to a preprint server 'e.g. medRxiv'?**
If 'Yes', please please give a link or doi:

(c) **Where is the work intended to be published?**

(d) **List the manuscript's authors in the intended authorship order:**

(e) **Stage of publication:**

3. **For multi-authored work, please give a statement of contribution covering all authors** (if single-author, please skip to section 4)**:**
Somogyi, Wilfrid: Writing, derivations, programmatic implementation, final *ab initio* calculations line list calculations and analysis
Yurchenko, Sergey N.: guidance
Kim, Gap-Sue: guidance, preliminary *ab initio* calculations

4. **In which chapter(s) of your thesis can this material be found?**
Chapters 3 and 5

e-Signatures confirming that the information above is accurate (this form should be co-signed by the supervisor/ senior author unless this is not appropriate, e.g. if the paper was a single-author work)**:**

Candidate:
Wilfrid Somogyi
Date: 15th October 2024

Supervisor :
Sergey Yurchenko
Date: 15th October 2024

UCL Research Paper Declaration Form: referencing the doctoral candidates own published work(s)

1. **1. For a research manuscript that has already been published** (if not yet published, please skip to section 2)**:**

   (a) **What is the title of the manuscript?**

   (b) **Please include a link to or doi for the work:**

   (c) **Where was the work published?**

   (d) **Who published the work?**

   (e) **When was the work published?**

   (f) **List the manuscript's authors in the order they appear on the publication:**

   (g) **Was the work peer reviewd?**

   (h) **Have you retained the copyright?**

   (i) **Was an earlier form of the manuscript uploaded to a preprint server (e.g. medRxiv)? If Yes, please give a link or doi**
   If No, please seek permission from the relevant publisher and check the box next to the below statement:

   ☐ *I acknowledge permission of the publisher named under 1d to include in this thesis portions of the publication named as included in 1c.*

2. **For a research manuscript prepared for publication but that has not yet been published** (if already published, please skip to section 3)**:**

   (a) **What is the current title of the manuscript?**
   ExoMol line lists: Empirical magnetic dipole and electric quadrupole spectra of the infrared bands of Oxygen (O_2)

   (b) **Has the manuscript been uploaded to a preprint server 'e.g. medRxiv'?**
   If 'Yes', please please give a link or doi:
   No

   (c) **Where is the work intended to be published?**
   Journal of Quantitative Spectroscopy and Radiative Transfer

   (d) **List the manuscript's authors in the intended authorship order:**

Somogyi, Wilfrid and Yurchenko, Sergey N. and Tennyson, Jonathan

(e) **Stage of publication:**
In preparation

3. **For multi-authored work, please give a statement of contribution covering all authors** (if single-author, please skip to section 4)**:**
Somogyi, Wilfrid: writing, *ab initio* calculations, empirical refinement, line list calculation
Yurchenko, Sergey: guidance, empirical refinement
Tennyson, Jonathan: guidance
4. **In which chapter(s) of your thesis can this material be found?**
Chapter 5

e-Signatures confirming that the information above is accurate (this form should be co-signed by the supervisor/ senior author unless this is not appropriate, e.g. if the paper was a single-author work)**:**

Candidate:
Wilfrid Somogyi
Date: 15th October 2024

Supervisor :
Sergey Yurchenko
Date: 15th October 2024

Contents

Table of Acronyms

Notation	Description
PEC	Potential ennergy curve.
SOC	Spin-orbit curve.
EAMC	Electronic angular momentum curve.
QMC	Electric quadrupole moment curve.
(E)QMC	Electric quadrupole moment curve.
DMC	Electric dipole moment curve.
E1	Electric dipole moment.
E2	Electric quadrupole moment.
M1	Magnetic dipole moment.
CCSD	Coupled cluster single and double.
CCSD(T)	Coupled cluster single and double with perturbative triple.
CI	Configuration interaction.
MRCI	Multi-reference configuration interaction.
(ic)MRCI	(Internally contracted) multi-reference configuration interaction.
ACPF	Averaged coupled-pair functional.
MLR	Morse long-range.
UV	Ultra-violet.
DVR	Discrete variable representation.
NAC	Non-adiabatic coupling.
DC	Diabatic coupling.
CRDS	Cavity ring-down spectroscopy.
ZPE	Zero-point energy.
EFGIB	Electric-field-gradient-induced birefringence.
MBERS	Molecular-beam electric-resonance spectroscopy.
RKR	Rydberg-Klein-Rees.
BOB	Born-Openheimer Breakdown.
CAS	Complete active space.

Notation	Description
MCSCF	Multiconfigurational self-consistent field.
TRF	Trust region reflective.
SN	Spectroscopic network.

List of Figures

List of Tables

Chapter 1

General Introduction

In recent decades, the discovery and detection of exoplanets has been a core focus of numerous astronomical surveys. As a result, there are over 5,000 known exoplanets across more than 4,000 planetary systems. At present there is an increasing focus on characterising the bulk and atmospheric compositions of these exoplanets, with a particular interest in the Earth-like class of rocky exoplanets [16–19]. A new generation of space telescopes is already being deployed to serve this mission, with CHEOPS, JWST, Twinkle, PLATO and Ariel among the best placed to perform these observations [20–24]. In each case these missions rely on transit spectroscopy - a method by which light from the host star is observed as it passes through the planet's atmosphere - to characterise exoplanetary atmospheres. The proportion of light absorbed in this way at a given wavelength is dependent on the constituent molecules in the atmosphere. Thus, given an observed spectrum and a list of candidate molecules, astronomers can infer the most likely composition using statistical methods - a technique known as atmospheric retrieval.

In order to support this ongoing body of exoplanetary research, a considerable wealth of spectroscopic data is needed for the numerous molecules of interest. The ExoMol project was created with the specific aim of producing such a database of 'line lists' for diatomic and small polyatomic molecules. A large number of molecular systems have already been studied, and this database of molecular opacities has already enabled the detection of numerous novel species in the atmospheres of extrasolar planets [25]. However, there is a unique and important class of molecules for which much of the necessary data is still outstanding. Specifically, these are systems for which transitions are forbidden in the electric dipole approximation of molecular spectroscopy. In particular, the $^{16}O_2$ molecule is of critical importance in exoplanetary studies due to it's potential to act as a biosignature in the atmospheres of habitable exoplanets.

Molecular oxygen has long been proposed as a potential biosignature due to its role as an electron donor in photosythensis reactions. An oxygenic biosig-

nature is favoured in the search for life because the key ingredients (CO_2 and H_2O) are thought to be present in large quantities on many habitable planets [26]. Chemotrophic life is, on the other hand, limited by the availability of alternative electron donors such as H_2 or Fe^{2+}. Moreover, the substantial abundance of $^{16}O_2$ in Earth's atmosphere is a result of oxygenic photosythensis, with very few known non-biological sources [27–29]. The primary non-biological source for persistent $^{16}O_2$ is photodissociation of oxygen-bearing species such as CO_2, but this is largely dependent on the spectral energy distribution of the host star [30–35]. As a result, the detection of a persistent abundance of $^{16}O_2$ in an exoplanetary atmosphere (primarily in the presence of O_3 and CH_4) along with an accurate characterisation of the host star's spectral flux, could provide a strong indication for the presence of life [36–38].

Beyond its role as a biosignature, detecting the presence or absence of oxygen in the proto-atmospheres of early Earth-like rocky planets also plays an important role in understanding their formation and geological evolution. It affects magma ocean cooling, rock melting and oxidation rates [39–41], and plays an important role in determining the abundance of other key atmospheric species such as H_2O, CO_2 and H_2 [42, 43, 39, 44, 45]. The next generation of space and ground-based telescopes will, in principle, enable detection of $^{16}O_2$ in exoplanetary atmospheres [46–48]. However, atmospheric retrieval relies on knowledge of the candidate molecule's absorption spectrum across a wide range of wavelengths. Molecular oxygen plays an important role in Earth's own atmosphere, with several key absorption bands used to in atmospheric modelling to characterise weather and climate patterns or monitor greenhouse gases [49–54]. The absorption spectrum for oxygen is well characterised in the narrow wavelength regions relevant to Earth-based applications, but knowledge of the temperature dependence of these bands, and of the absorption strength of other bands in the infrared region is currently insufficient for accurate exoplanetary retrieval methods. While experiment can provide accurate absorption strengths for a few spectral lines in the narrow bandwidth of the available instrumentation, and at a handful of temperatures, they cannot provide the broad spectral coverage required for the statistical methods employed by retrieval codes such as TauREx [55]. The large-scale line list production required for these applications is usually performed using computational methods that can accurately simulate the quantum mechanical interactions of molecules with electromagnetic radiation at arbitrary wavelengths and temperatures.

The transitions probabilities themselves are determined by both the eigenstates of the molecule and by various multipole interactions that allow the molecule to absorb and emit photons of electromagnetic radiation. Pure rotation and vibration transitions, which account for the *infrared* spectra of diatomic molecules, are forbidden for homonuclear diatomic molecules in the electric dipole approximation as a result of molecular symmetry. Similarly,

transitions between electronic states of the same symmetry are also forbidden. This means the lowest energy electric dipole moment transitions for many homonuclear diatomic molecules fall in the UV region of the spectrum, which cannot be observed in astronomical contexts due to absorption by interstellar dust. Broadly speaking, all homonuclear diatomic molecules (including N_2, S_2, and crucially O_2) fall into this class - with only a few notable exceptions such as C_2, where closely spaced electronic states of different symmetries allow for electric dipole moment transitions with wavelengths longer than UV or visible light.

The infrared and visible spectra of most homonuclear diatomic molecules are instead dominated by higher order electric quadrupole and magnetic dipole moment transitions. These transitions moments arise from higher order terms in the multipole expansion of the light-matter interaction. Typically they are several orders of magnitude weaker than electric dipole transitions, but can nonetheless form the dominant contributions to absorption cross-sections in the absence of electric dipole radiation. In many cases, the relative strengths of the electric quadrupole and magnetic dipole moments are similar and so both sources of absorption must be considered simultaneously in the production of a line list. In the case of $^{16}O_2$ the magnetic dipole transitions generally provide the strongest contributions, and are responsible for the well-known atmospheric δ, γ, B, and A-bands. However, electric quadrupole transitions have also been observed in atmospheric and solar spectra [56–58]. Rovibrational transitions in the $X\,^3\Sigma_g^-$ ground electronic state of $^{16}O_2$ are likely to be the most important for exoplanetary retrieval. In particular, the $X\,^3\Sigma_g^-$ ($v = 1 \rightarrow 0$) band lies firmly within the spectral range of specialist telescopes such as ARIEL, and contains contributions of approximately equal strength from both electric quadrupole and magnetic dipole moments [59, 60].

Producing a line list requires numerically solving the Schrödinger equation for the molecular Hamiltonian to obtain the rotational, vibrational and electronic (rovibronic) wavefunctions and energy levels of the molecule. This information can in turn be used to calculate transition probabilities between these same energy levels. Typically the Schrödinger equation for the *electronic* degrees of freedom is solved first, at a range of internuclear geometries, to produce a set of electronic potential energy curves (or potential energy surfaces in the case of polyatomic molecules). These potential energy curves can subsequently be used to solve the nuclear Schrödinger equation and obtain the vibrational and rotational energy levels and wavefunctions. Knowledge of the rotational, vibrational and electronic wavefunctions allows one to calculate transition probabilities and absorption intensities for transitions between these combined 'rovibronic' levels.

Generally, the electronic Schrödinger equation is solved, and the electronic structure properties obtained, using quantum chemistry codes such as Mol-

PRO, GAUSSIAN, or CFOUR [61–63]. Meanwhile the nuclear Schrödinger equation and transition probabilities can be solved using programs such as DUO, which was also produced as part of the ExoMol project [64]. This nuclear motion code is capable of solving the molecular Hamiltonian with an arbitrary number of couplings between electronic states, including spin-orbit, spin-rotation, spin-spin and other coupling terms.

Like many spectroscopic treatments, the DUO program has, until now, produced molecular spectra by assuming the validity of the electric dipole approximation. In this thesis, I introduce significant extensions to the DUO program that enable the calculation of higher order transition probabilities, and thus facilitate the production of line lists for homonuclear molecules, as well as other electronic systems for which transitions are forbidden by the electric dipole moment selection rules. This forms part of a novel computational methodology for calculating both electric quadrupole and magnetic dipole transition probabilities, which is subsequently used to produce a high-resolution line list for molecular oxygen across a large range of wavelengths.

The outline of this thesis is as follows. In the first chapter I introduce the electric dipole approximation and provide a rigorous theoretical basis for the higher order electric quadrupole and magnetic dipole interactions. I also derive the form of the operators that govern the strength of these interactions and relate them to the Einstein A-coefficients for spontaneous emission. I then introduce the irreducible representation for these tensor operators, which plays an important role in the determining expressions for the matrix elements and hence intensities of the magnetic dipole and electric quadrupole moments. In the final part of this chapter I introduce the rotational, vibrational and electronic basis sets used by the DUO program, and use them to derive explicit expressions for the absorption intensity. These expressions have been implemented programmatically in the DUO program. In the second chapter I provide background on the method for producing a spectroscopic model of a homonuclear molecule. I begin by introducing the Born-Oppenheimer approximation, which underpins the spectroscopic approach, and dictates how the Schrödinger equation for the molecular Hamiltonian is solved, first by solving for the electronic degrees of freedom, and then for the nuclear degrees of freedom. I also outline the adiabatic approximation, and the implication this has on the solution to the nuclear motion, and how I account for the effects of non-adiabatic interactions between the electronic states of a diatomic molecule. In this chapter I also introduce the representation of the electronic structure properties and how it is transformed after solving the electronic degrees of freedom in order to facilitate the nuclear solution.

In the subsequent chapter I bring the theoretical elements together to provide a spectroscopic model and a computational line list for the $^{16}O_2$ molecule. I start by outlining the structure of the infrared bands, and the electronic states

and couplings that form their major contributions. I then detail the electronic structure calculations that form the basis of the spectroscopic model. At the end of this chapter I outline the nuclear motion calculations performed with Duo and present the line list for the infrared and visible spectrum of $^{16}O_2$ for use in astronomical applications. Initially I present the *ab initio* line list as a direct result of the electronic structure calculations. This line list is then empirically refined by fitting analytic representations of several electronic structure properties to experimentally measured state energies. In the appendix I present additional spectroscopic calculations that were performed during the production of this thesis. Including the infrared spectrum of H_2, CO, and HF, which were used as initial validations of the implemented quadrupole code for pure rotation-vibration transitions and for electronic transitions, respectively. Lastly I present calculations of the infrared electric quadrupole spectra for HF and CO. Although these are both heteronuclear diatomic molecules with allowed electric dipole transitions, they are also examples of heteronuclear systems with strong quadrupole moments. They therefore serve to represent the generality of the implementation beyond homonuclear diatomics.

I conclude the thesis by outlining potential directions for future on this subject matter, and outlining some of the outstanding points that remain unresolved.

Chapter 2

Transition Moments

2.1 Introduction

In the treatment of molecular spectra, the mechanism by which electrons absorb or emit a photon of light is usually approximated to first order. This is known as the electric dipole approximation, and in most cases proves sufficient for modelling molecular spectra. Higher order mechanisms such as the electric quadrupole or magnetic dipole interactions are orders of magnitude weaker and therefore ordinarily contribute negligibly to the absorption cross-section of a molecule. In the case of homonuclear molecules however the electric dipole selection rules (which govern the pairs of quantum states between which a molecule can transition) forbid transitions between rotational or vibrational states of a molecule, or electronic transitions between states of the same symmetry. As a result, these higher order mechanisms become the dominant means by which molecules absorb and emit light.

Such transitions are often challenging to measure in the laboratory, owing to their weaker relative intensity and the longer path lengths required for appreciable absorption [65, 66]. Nevertheless, they are often present in atmospheric spectra where sufficiently long path lengths are regularly achievable [57, 67, 60, 68, 58, 69]. In many spectroscopic contexts, such as the HITRAN database, the higher order moments are treated using effective Hamiltonians, with the rotational line intensities modelled via Hönl-London factors. However, a variational methodology that provides a complete description of the molecular eigenstates is preferred for accurate high-resolution line lists, and this is the approach adopted by the ExoMol project.

In order to treat electric quadrupole and magnetic dipole absorption, I have derived explicit expressions for the intensity of these transitions in terms of the rovibronic basis states and electronic structure properties. In this chapter I will present the full derivation of these expressions, as well as the final form that has been implemented programmatically in Duo.

2.2 Origin of the Higher Order Moments

In this section I briefly outline the theoretical basis for the higher order transition moments. Starting from the full molecular Hamiltonian in the presence of an external electromagnetic field, and employing the Schrödinger-Pauli equation I derive expressions for the electric dipole, electric quadrupole and magnetic dipole moment operators. I then show how these are linked to the transition linestrengths and Einstein A-coefficients via the corresponding rate equations.

2.2.1 Electromagnetic Interaction

I start by defining the electromagnetic field in terms of the scalar and vector potentials ϕ and $\vec{A}$, with electric and magnetic components $\vec{E} = -\nabla\phi - \frac{\partial \vec{A}}{\partial t}$ and $\vec{B} = \nabla \times \vec{A}$ respectively. The molecular electron has mass m_e, charge $-e$, and is subject to a molecular potential $V(\vec{r}, \vec{R})$ that depends on the position of the electron $\vec{r}$ and the molecular geometry $\vec{R}$. The Schrödinger-Pauli equation for this system takes the form

$$\left[\frac{\left(\hat{p} + e\vec{A}\right)^2}{2m_e} + \frac{e\hbar}{2m_e}\vec{\sigma}\cdot\vec{B} - e\phi + V(\vec{r},\vec{R})\right]|\Psi\rangle = i\hbar\frac{\partial}{\partial t}|\Psi\rangle \tag{2.2.1}$$

where $\vec{\sigma}$ is the vector of Pauli operators acting on the electronic spin angular momentum. The first term of Eq. (2.2.1) can the be expanded to obtain the Hamiltonian as a power series in the vector potential $\vec{A}$

$$H = \frac{\vec{p}^2}{2m_e} - \frac{e\vec{A}\cdot\vec{p}}{m_e} + \frac{e^2\vec{A}^2}{2m_e} - \frac{e}{m_e}\vec{S}\cdot\vec{B} - e\phi + V(\vec{r},\vec{R}) \tag{2.2.2}$$

where $\hat{S} = \frac{\hbar}{2}\vec{\sigma}$ is the spin operator. If the field strength is weak, then the second order term ($\vec{A}^2$) can be neglected. Note also that the electromagnetic field can be expressed as a linear combination of monochromatic plane waves with polarisation $\hat{\varepsilon}$ and wave vector $\vec{k}$. In this case we can make a choice of gauge such that $\phi = 0$, and the Hamiltonian can be written as a sum of field-free and field-dependent terms

$$H_0 = \frac{\vec{p}^2}{2m_e} + V(\vec{r},\vec{R}) \tag{2.2.3}$$

$$H_1 = -\frac{e\vec{A}\cdot\vec{p}}{m_e} - \frac{e}{m_e}\vec{S}\cdot\vec{B} \tag{2.2.4}$$

this is known as the Weyl gauge, and gives a vector potential of the form

$$\vec{A}(\vec{r},t) = \int_{-\infty}^{\infty}\frac{A_0(\omega)\hat{\varepsilon}}{2}\left(\exp\left[i(\vec{k}\cdot\vec{r}-\omega t)\right] + \exp\left[-i(\vec{k}\cdot\vec{r}-\omega t)\right]\right)\mathrm{d}\omega \tag{2.2.5}$$

Initially let us consider only the first term in Eq. (2.2.4), which gives rise to the electric dipole, electric quadrupole and magnetic dipole moments via a Taylor expansion of the plane wave components. Later, in Sec. 2.2.3, we will see how the second term also generates an additional contribution to the magnetic dipole transition moment.

Perturbation theory gives the probability that a monochromatic plane wave of frequency ω_{ba} induces a transition between two states of a quantum system a and b as [70, 71]:

$$P_{ba}(t) = |C_{ba}(t)|^2 \tag{2.2.6}$$

where

$$C_{ba}(t) = \frac{i}{\hbar}\int_0^t H_{ba}(t')\exp[i\omega_{ba}t']\,\mathrm{d}t' \tag{2.2.7}$$

where H_{ba} is the Hamiltonian (2.2.2) in the presence of a time-dependent electromagnetic field. Substituting in the first term of Eq. (2.2.4) we obtain

$$\begin{aligned} C_{ba}(t) =& \frac{ieA_0}{2\hbar m_e}\int_0^t \langle b|\exp\Big[i(\vec{k}\cdot\vec{r}-\omega t')\Big]\hat{\varepsilon}\cdot\vec{p}|a\rangle\exp[i\omega_{ba}t'] \\ &+ \langle b|\exp\Big[-i(\vec{k}\cdot\vec{r}-\omega t')\Big]\hat{\varepsilon}\cdot\vec{p}|a\rangle\exp[i\omega_{ba}t']\,\mathrm{d}t' \end{aligned} \tag{2.2.8}$$

$$\begin{aligned} =& \frac{ieA_0}{2\hbar m_e}\int_0^t \langle b|\exp\Big[i(\vec{k}\cdot\vec{r})\Big]\hat{\varepsilon}\cdot\vec{p}|a\rangle\exp[-i\omega t']\exp[i\omega_{ba}t'] \\ &+ \langle b|\exp\Big[-i(\vec{k}\cdot\vec{r})\Big]\hat{\varepsilon}\cdot\vec{p}|a\rangle\exp[i\omega t']\exp[i\omega_{ba}t']\,\mathrm{d}t' \end{aligned} \tag{2.2.9}$$

Then, integrating this expression with the initial condition $P_{ba}(t=0)=0$,

$$\begin{aligned} C_{ba}(t) = \frac{iA_0(\omega)t^2}{2\hbar}\Bigg(& M_{ba}\exp\Big[-i(\omega-\omega_{ba})\frac{t}{2}\Big]\,\mathrm{sinc}\left[(\omega-\omega_{ba})\frac{t}{2}\right] \\ &+M_{ba}^{\dagger}\exp\Big[i(\omega+\omega_{ba})\frac{t}{2}\Big]\,\mathrm{sinc}\left[(\omega+\omega_{ba})\frac{t}{2}\right]\Bigg) \end{aligned} \tag{2.2.10}$$

Where we have separated the expression in Eq. (2.2.6) into the sum of absorption and emission terms and defined the transition matrix element

$$M_{ba} = \frac{e}{m_e}\langle b|\exp\Big[i\vec{k}\cdot\vec{r}\Big]\hat{\varepsilon}\cdot\vec{p}|a\rangle \tag{2.2.11}$$

This matrix element is the characteristic quantity that determines the strength of the light-matter interaction.

Thus, for an arbitrary time-independent electromagnetic field, we can write the transition probability at time t as

$$P_{b\leftarrow a}(t) = \int_{-\infty}^{\infty}\frac{|A_0(\omega)|^2t^2}{4\hbar^2}\left|M_{ba}\right|^2\mathrm{sinc}^2\left[(\omega-\omega_{ba})\frac{t}{2}\right]\mathrm{d}\omega \tag{2.2.12}$$

$$P_{b\to a}(t) = \int_{-\infty}^{\infty}\frac{|A_0(\omega)|^2t^2}{4\hbar^2}\left|M_{ba}^{\dagger}\right|^2\mathrm{sinc}^2\left[(\omega+\omega_{ba})\frac{t}{2}\right]\mathrm{d}\omega \tag{2.2.13}$$

2.2.2 Electric Dipole Moment Approximation

In this section I will show how the general form of the matrix element given previously can be expanded to derive the electric dipole approximation, as well as the higher order interactions. The exponential term in the matrix element Eq. (2.2.11) can be expanded as a power series in the exponent:

$$\exp\left[i\vec{k}\cdot\vec{r}\right] = 1 + (i\vec{k}\cdot\vec{r}) + \frac{1}{2}(i\vec{k}\cdot\vec{r})^2 + ... \tag{2.2.14}$$

Truncation at the first term gives the matrix element M_{ba} as:

$$M_{ba}(\omega) \simeq \frac{e}{m_e}\langle b|\hat{\varepsilon}\cdot\vec{p}|a\rangle \tag{2.2.15}$$

$$= \frac{e}{m_e}\hat{\varepsilon}\cdot\langle b|-\frac{im_e}{\hbar}[\vec{r},H_0]|a\rangle \tag{2.2.16}$$

$$= -\frac{ie}{\hbar}\hat{\varepsilon}\cdot\Big(\langle b|\vec{r}H_0|a\rangle - \langle b|H_0^\dagger\vec{r}|a\rangle\Big) \tag{2.2.17}$$

$$= -\frac{ie}{\hbar}\hat{\varepsilon}\cdot(\langle b|\vec{r}E_a|a\rangle - \langle b|E_b\vec{r}|a\rangle) \tag{2.2.18}$$

$$= ie\omega_{ba}\hat{\varepsilon}\cdot\langle b|\vec{r}|a\rangle \tag{2.2.19}$$

Such that the transition probability becomes

$$P^{(\mathrm{E1})}_{b\leftarrow a}(t) = \int_{-\infty}^{\infty}\frac{|A_0(\omega)|^2t^2}{4\hbar^2}\omega_{ba}^2\left|\hat{\varepsilon}\cdot\vec{D}_{ba}\right|^2\mathrm{sinc}^2\left[(\omega-\omega_{ba})\frac{t}{2}\right]\mathrm{d}\omega \tag{2.2.20}$$

where $\vec{D}_{ba} = \langle b|\vec{D}|a\rangle = \langle b|e\vec{r}|a\rangle$ is the transition electric dipole (E1) moment between the two states. This truncation is known as the *electric dipole approximation*, and it gives the probability of a transition between an initial state $|a\rangle$ and a final state $|b\rangle$ in the presence of a moderate or weak electromagnetic field under the following conditions:

1. The electromagnetic field is sufficiently weak that it can be treated perturbatively, and second order field effects can be neglected.
2. The electric dipole moment, $\vec{D}_{ab}$ between the inital and final states is non-vanishing.

The electric dipole moment itself contains both permanent and induced moments

$$\vec{D} = \vec{D}^{(0)} + \vec{D}^{(1)} + \vec{D}^{(2)} + ... \tag{2.2.21}$$

The permanent electric dipole, $\vec{D}^{(0)}$, is due to the field-free charge distribution of the molecule, whilst the induced electric dipole moments arise as a result of the interaction between the molecule's charge distribution and the incident electric field, $\vec{E}(t)$. If the first condition above does not hold then we must

consider the first order induced dipole moment arising from the molecule's polarisability

$$\vec{D}_j^{(1)} = \alpha_{ij}\vec{E}_j(t) \tag{2.2.22}$$

or the second order induced dipole moment arising from the molecule's hyperpolarisability

$$\vec{D}_j^{(2)} = \beta_{ijk}\vec{E}_k(t)\vec{E}_j(t) \tag{2.2.23}$$

These time-dependent effects usually need only be considered when the field strength is strong or varies quickly with time, for example in the presence of laser radiation, and thus do not play a role in the production of an absorption line list.

2.2.3 Higher Order Moments

In general, any asymmetric molecule will have a non-zero dipole moment as a result of the differential charge distribution that results from atomic centres with varying degrees of electronegativity. Conversely, the permanent dipole moment vanishes in molecules like O_2, N_2, S_2, H_2 and other homonuclear diatomic molecules because the electron distribution is symmetric around both atomic centres. To describe the spectra of such molecules, we must therefore look to the second term of the expansion (2.2.14), which generates the matrix elements of the magnetic dipole moment and electric quadrupole moment.

$$M_{ba} = \frac{e}{m_e}\langle b|(i\vec{k}\cdot\vec{r})(\hat{\varepsilon}\cdot\vec{p})|a\rangle \tag{2.2.24}$$

The electric quadrupole moment is generally non-zero even for homonuclear molecules, due to the spherically asymmetric charge distribution that results from the molecular bond. Similarly, the magnetic dipole moment is non-zero for molecules with electronic angular momentum. In this section I will derive independent expressions for the magnetic dipole operator and the electric quadrupole moment operators.

First, consider briefly the commutator $\left[\hat{H}_0, (\hat{\varepsilon}\cdot\vec{r})(\vec{k}\cdot\vec{r})\right]$, which we can expand as

$$\begin{aligned}
\frac{im_e}{\hbar}\left[\hat{H}, (\hat{\varepsilon}\cdot\vec{r})(\vec{k}\cdot\vec{r})\right] &= \frac{im_e}{\hbar}\varepsilon_i k_j\left[\hat{H}, r_i r_j\right] && (2.2.25)\\
&= \frac{im_e}{\hbar}\varepsilon_i k_j\left(r_i\left[\hat{H}, r_j\right] + \left[\hat{H}, r_i\right] r_j\right) && (2.2.26)\\
&= \varepsilon_i k_j(r_i p_j + p_i r_j) && (2.2.27)\\
&= (\hat{\varepsilon}\cdot\vec{r})\left(\vec{k}\cdot\vec{p}\right) + (\vec{k}\cdot\vec{r})(\vec{\varepsilon}\cdot\vec{p}) && (2.2.28)
\end{aligned}$$

where the canonical commutation relation $\vec{p} = [\hat{H}_0, \vec{r}]$ has been used in Eq. (2.2.27). Next, using the identity $(\vec{k}\cdot\vec{r})(\hat{\varepsilon}\cdot\vec{p}) = (\vec{k}\times\hat{\varepsilon})\cdot(\vec{r}\times\vec{p}) + (\hat{\varepsilon}\cdot\vec{r})(\vec{k}\cdot\vec{p})$,

we can re-write the matrix element (2.2.24) as

$$M_{ba}(\omega) = \frac{ie}{m_e}\Big(\langle b|(\vec{k}\times\hat{\varepsilon})\cdot(\vec{r}\times\vec{p})|a\rangle + \langle b|(\hat{\varepsilon}\cdot\vec{r})(\vec{k}\cdot\vec{p})|a\rangle\Big) \tag{2.2.29}$$

Then rearranging Eq.(2.2.28) and substituting the result in place of the second term in the expression above we can write

$$\begin{aligned} M_{ba}(\omega) = \frac{ie}{m_e}\Big(&\langle b|(\vec{k}\times\hat{\varepsilon})\cdot(\vec{r}\times\vec{p})|a\rangle \\ &+ \langle b|\frac{im_e}{\hbar}\Big[\hat{H},(\hat{\varepsilon}\cdot\vec{r})(\vec{k}\cdot\vec{r})\Big]|a\rangle - \langle a|(\hat{\varepsilon}\cdot\vec{r})(\vec{k}\cdot\vec{p})|a\rangle\Big) \end{aligned} \tag{2.2.30}$$

$$= \frac{ie}{2m_e}\langle b|(\vec{k}\times\hat{\varepsilon})\cdot(\vec{r}\times\vec{p})|a\rangle - \frac{1}{2\hbar}\langle b|\Big[\hat{H}_0,(\hat{\varepsilon}\cdot\vec{r})(\vec{k}\cdot\vec{r})\Big]|a\rangle \tag{2.2.31}$$

where we have also used Eq. (2.2.24) to obtain the factor of ½ in Eq. (2.2.31). The final step is to write the commutator explicitly, and apply the Hamiltonian in the same way as for the electric dipole moment in Eq. (2.2.19),

$$M_{ba}(\omega) = \frac{ie}{2m_e}\langle b|(\vec{k}\times\hat{\varepsilon})\cdot(\vec{r}\times\vec{p})|a\rangle - \frac{ie\omega_{ba}}{2\hbar}\langle b|(\hat{\varepsilon}\cdot\vec{r})(\vec{k}\cdot\vec{r})|a\rangle \tag{2.2.32}$$

This expression for the matrix element arising due to the second order term in the expansion of the electromagnetic field contains two terms, which I will now show can be identified as the magnetic dipole moment and electric quadrupole moment respectively.

Magnetic Dipole Moment

The first term can be identified as the magnetic dipole moment by substituting $\vec{l} = \vec{r}\times\vec{p}$ and $(\vec{k}\times\hat{\varepsilon}) = k\hat{b}$ (with $k = |\vec{k}|$ the wavenumber)

$$P^{(\mathrm{M1})}_{b\leftarrow a} = \int_{-\infty}^{\infty}\frac{|A_0(\omega)|^2t^2}{4\hbar^2}\frac{\omega_{ba}^2}{4\pi^2c^2}\left|\hat{b}\cdot\vec{d}_{ba}\right|^2\mathrm{sinc}^2\left[(\omega-\omega_{ba})\frac{t}{2}\right]\mathrm{d}\omega \tag{2.2.33}$$

where $\hat{b}$ is the magnetic unit vector. The magnetic dipole (M1) moment due to the molecule's angular momentum as has thus been defined as

$$\hat{d} = -\frac{e}{2m_e}\hat{l} \tag{2.2.34}$$

An additional contribution to the magnetic dipole moment arises from the second term in Eq. (2.2.4). From the definition of the magnetic field $\vec{B} = \nabla\times\vec{A}$, we can write an expression for $\vec{B}$ of similar form to Eq. (2.2.5)

$$\vec{B}(\vec{r},t) = \int_{-\infty}^{\infty}\frac{iA_0\omega\hat{b}}{c}\Big(\exp\Big[i(\vec{k}\cdot\vec{r}-\omega t)\Big] - \exp\Big[-i(\vec{k}\cdot\vec{r}-\omega t)\Big]\Big)\,\mathrm{d}\omega \tag{2.2.35}$$

where $\hat{b}$ is the magnetic field polarisation. Following the same procedure as outlined for the first term in Eq. (2.2.4) produces a Taylor expansion, of which the zeroth order term has the form

$$\hat{d} = -\frac{e}{2m_e} g_s \hat{s} \tag{2.2.36}$$

Thus, for a spin-1/2 particle, the total magnetic dipole moment becomes the sum of orbital and spin contributions

$$\hat{d} = -\frac{e}{2m_e} \left(\hat{l} + g_s \hat{s} \right) \tag{2.2.37}$$

where g_s is the Landé g-factor. The total magnetic dipole moment operator for a system of n electrons is, by extension, therefore

$$\hat{d} = -\frac{e}{2m_e} \sum_i^n \left(\hat{l}_i + g_s \hat{s}_i \right) = -\frac{e}{2m_e} \left(\hat{L} + g_s \hat{S} \right) \tag{2.2.38}$$

We have thus obtained, from the Hamiltonian for a molecular electron in the presence of an electromagnetic field, an expression for the magnetic dipole moment of a system of n electrons.

Electric Quadrupole Moment

To derive an expression for the electric quadrupole moment operator we turn to the second term in Eq. (2.2.32), which can be expressed using Einstein's notation as

$$(\hat{\varepsilon} \cdot \vec{r})(\vec{k} \cdot \vec{r}) = \varepsilon_i k_j r_i r_j \tag{2.2.39}$$

The definition of the electromagnetic field ensures that the electric field vector, $\hat{\varepsilon}$, and the wave vector, $\vec{k}$, are orthogonal, such that

$$\hat{\varepsilon} \cdot \vec{k} = \varepsilon_i k_i = \varepsilon_x k_x + \varepsilon_y k_y + \varepsilon_z k_z = 0 \tag{2.2.40}$$

We now deliberately chose to make a trivial subtraction of this zero-value quantity $\hat{\varepsilon} \cdot \vec{k}$ in order to define the electric quadrupole moment as a traceless quantity, which will later prove to be useful in transforming it between rotational reference frames,

$$(\hat{\varepsilon} \cdot \vec{r})(\vec{k} \cdot \vec{r}) = (\hat{\varepsilon} \cdot \vec{r})(\vec{k} \cdot \vec{r}) - \hat{\varepsilon} \cdot \vec{k} \tag{2.2.41}$$

$$= \varepsilon_i k_j r_i r_j - \frac{1}{3} \varepsilon_i k_j (r_x r_x + r_y r_y + r_z r_z) \delta_{ij} \tag{2.2.42}$$

$$= \varepsilon_i \left(r_i r_j - \delta_{ij} \frac{1}{3} ||\vec{r}||^2 \right) k_j \tag{2.2.43}$$

This second second rank tensor is then defined as the electric quadrupole moment

$$Q = -\frac{e}{2}\left(r_i r_j - \delta_{ij}\frac{1}{3}||\vec{r}||^2\right) \tag{2.2.44}$$

In Sec. 2.3 we will see that defining the quadrupole in this way, such that its trace is zero, simplifies considerably the calculation of its matrix elements. The transition probability for the electric quadrupole moment is

$$P^{(\mathrm{E2})}_{b\leftarrow a} = \int_{-\infty}^{\infty} \frac{|A_0(\omega)|^2 t^2}{4\hbar^2}\frac{\omega_{ba}^4}{4\pi^2 c^4}\left|\hat{\varepsilon}\cdot Q_{ba}\cdot\hat{k}\right|^2 \mathrm{sinc}^2\left[(\omega-\omega_{ba})\frac{t}{2}\right]\mathrm{d}\omega \tag{2.2.45}$$

where $\hat{k}$ is the unit wave vector and Q_{ba}, the transition electric quadrupole (E2) moment. The total quadrupole operator for a system of electrons is, by extension, defined as

$$\hat{Q} = -\frac{e}{2}\sum_{l=0}^{n} r_{il}r_{jl} - \delta_{ij}\frac{1}{3}||\vec{r}_l||^2 \tag{2.2.46}$$

where l indexes over the n electrons, with position vectors $\vec{r}_l$. Different sources employ definitions of the quadrupole operator with varying constant pre-factors [61–63, 4, 72]. The definition of the quadrupole operator given by Eq. (2.2.44) is the natural quadrupole moment. An equivalent definition derived by Buckingham [73], and quoted throughout the literature is larger by a factor of three

$$\hat{Q} = -\frac{e}{2}\sum_{l=0}^{n}\left(3r_{il}r_{jl} - \delta_{ij}||\vec{r}_l||^2\right) \tag{2.2.47}$$

In which case the integrand in Eq. (2.2.45) contains an additional constant factor of $1/9$. Hereafter, we use the convention of Buckingham [73], which is the definition employed by many, such as Werner et al. [74] in the quantum chemistry program Molpro.

2.3 The Irreducible Representation

Inherent in the description of molecular mechanics is the need to transform between molecule-fixed, and laboratory-fixed reference frames. The vibrational and electronic motions of a molecule are most straightforwardly described in the molecule-fixed reference frame, while the rotational motion must be considered in the laboratory-fixed frame. One must therefore be able to transform the relevant tensor operators between the two reference frames. In the case of rank one tensor operators, such as the electric and magnetic dipole moments, this transformation is relatively straightforward. Rank one (vector) operators

transform as the Euclidean basis vectors. However, transforming the second rank electric quadrupole moment is more complicated and requires an understanding of the so-called irreducible representation.

In this section I will outline the requisite theoretical elements for performing this transformation. I will begin by introducing the Clebsch-Gordan coefficients, and the related Wigner 3-j symbols, which allow us to relate the spherical components of a tensor operator to the irreducible tensor components. These irreducible components can in turn be straightforwardly transformed between rotating reference frames by applying the Wigner D-matrices. I will then employ elements of group theory for the three-dimensional rotation group $SO(3)$ to derive the relationship between the Cartesian and spherical elements of the electric quadrupole moment. I will then combine these two elements to obtain a final expression for the irreducible components of the electric quadrupole moment in terms of the Cartesian elements defined in Eq. (2.2.47), and show how these irreducible components can be transformed between the molecule-fixed and space-fixed reference frames.

2.3.1 Clebsch-Gordan Coefficients

The Clebsch-Gordan coefficients are a set of numbers that arise when dealing with coupled angular momenta in quantum mechanics. They allow one to decompose coupled angular momenta from a reducible representation to an irreducible representation, where the total angular momentum can be represented as a tensor product of two uncoupled angular momenta. Similarly, they allow us to relate the components of a spherical rank two tensor operator to the irreducible spherical components of that same operator. An equivalent set of quantities are the Wigner 3-j symbols, which are often employed in place of the Clebsch-Gordan coefficients because of their simple symmetry properties.

In this section I will briefly outline the derivation of the Clebsh-Gordan coefficients, and establish their relation to the 3-j symbols. To begin, note that a combined system of two angular momenta, j_1 and j_2, can be expressed in terms of the direct product between uncoupled representations [75, 76]:

$$|j_1 m_1, j_2 m_2\rangle = |j_1 m_1\rangle \, |j_2 m_2\rangle \tag{2.3.1}$$

where $j_i = 0, 1, 2, \ldots$ and $-j_i \leq m_i \leq j_i$, with $i = 1, 2$. The same system can also be described in terms of the coupled representation $|j_3 m_3\rangle$, where:

$$|j_1 - j_2| \leq j_3 \leq j_1 + j_2 \quad \text{and} \quad -j_3 \leq m_3 \leq j_3 \tag{2.3.2}$$

These representations both occupy a vector space of dimension $(2j_1+1)(2j_2+1)$

and the two can be related by inserting the resolution of identity:

$$|j_3 m_3\rangle = \sum_{m_1=-j_1}^{j_1} \sum_{m_2=-j_2}^{j_2} |j_1 m_1, j_2 m_2\rangle\langle j_1 m_1, j_2 m_2| \, |j_3 m_3\rangle \tag{2.3.3}$$

$$= \sum_{m_1=-j_1}^{j_1} \sum_{m_2=-j_2}^{j_2} C(j_1, j_2, j_3; m_1, m_2, m_3) \, |j_1 m_1, j_2 m_2\rangle \tag{2.3.4}$$

where the coefficients introduced in the second line

$$C(j_1, j_2, j_3; m_1, m_2, m_3) = \langle j_1 m_1, j_2 m_2 | j_3 m_3\rangle = \langle j_3 m_3 | j_1 m_1, j_2 m_2\rangle \tag{2.3.5}$$

are the Clebsch-Gordan coefficients. The Clebsch-Gordan coefficients can be calculated explicitly through a series of recursion relations that are well documented in the literature. The Wigner 3-j symbols are a closely related set of quantities that are defined in relation to the Clebsch-Gordan coefficients as

$$C(j_1, j_2, j_3; m_1, m_2, m_3) = (-1)^{-j_1+j_2-m_3}(2j_3+1)^{\frac{1}{2}} \begin{pmatrix} j_1 & j_2 & j_3 \\ m_1 & m_2 & -m_3 \end{pmatrix} \tag{2.3.6}$$

Although the Clebsch-Gordan coefficients and the Wigner 3-j symbols are equivalent, the latter have simpler symmetry properties and are therefore more straightforward to use. Namely the 3-j symbols are invariant under cyclic permutations of their columns

$$\begin{pmatrix} j_1 & j_2 & j_3 \\ m_1 & m_2 & m_3 \end{pmatrix} = \begin{pmatrix} j_3 & j_1 & j_2 \\ m_3 & m_1 & m_2 \end{pmatrix} = \begin{pmatrix} j_2 & j_3 & j_1 \\ m_2 & m_3 & m_1 \end{pmatrix} \tag{2.3.7}$$

and are zero unless the following conditions are met

$$m_1 + m_2 + m_3 = 0 \tag{2.3.8}$$

$$|j_1 - j_2| \leq j_3 \leq j_1 + j_2 \tag{2.3.9}$$

2.3.2 Irreducible Tensor Components

I now turn to the representation of the tensor operator itself. The first step is to establish the definition of the quadrupole moment operator in the spherical basis. The spherical basis itself can be related to the Cartesian basis as follows

$$\vec{e}_{+1} = -\frac{1}{\sqrt{2}} (\vec{e}_x + i\vec{e}_y) \tag{2.3.10}$$

$$\vec{e}_{-1} = \frac{1}{\sqrt{2}} (\vec{e}_x - i\vec{e}_y) \tag{2.3.11}$$

$$\vec{e}_0 = \vec{e}_z \tag{2.3.12}$$

In Sec. 2.2.3, the quadrupole moment operator was defined as a second rank tensor in the Cartesian basis, formed from the product of two Cartesian rank one tensor (i.e vector) operators, namely the position operator $\vec{r}$. We can similarly define a rank two tensor in the spherical basis as the product of two rank one spherical tensors

$$T_{\lambda\mu} = (-1)^{\mu} V_{\lambda} W_{\mu} \tag{2.3.13}$$

with $\lambda, \mu \in \{-1, 0, +1\}$. The signed factor in this expression is necessitated by the use of the Condon-Shortley phase factor in definition of the spherical basis above. The relationship between the spherical quadrupole components and the Cartesian components defined in Eq. (2.2.47) can be obtained by substituting the relations (2.3.10) - (2.3.12) and identifying products of the rank one tensor elements with the Cartesian components of the quadrupole operator

$$V_{\rho} W_{\sigma} \coloneqq Q_{\rho\sigma} \tag{2.3.14}$$

with $\rho, \sigma \in \{x, y, z\}$. Consider, for example, the case where $\lambda = -1$ and $\mu = +1$,

$$\begin{aligned} Q_{-1+1} &= V_{-1} W_{+1} && (2.3.15)\\ &= \frac{1}{2}(V_x - iV_y)(W_x + iW_y) && (2.3.16)\\ &= \frac{1}{2}(V_x W_x + iV_x W_y - iV_y W_x + V_y W_y) && (2.3.17)\\ &= \frac{1}{2}(Q_{xx} + Q_{yy} + iQ_{xy} - iQ_{yx}) && (2.3.18) \end{aligned}$$

Following this procedure all the nine spherical components, we obtain a set of relations that transform between the Cartesian and spherical components of

the quadrupole moment operator.

$$Q_{-1-1} = -\frac{1}{2}(Q_{xx} - Q_{yy} - iQ_{xy} - iQ_{yx}) \tag{2.3.19}$$

$$Q_{-10} = \frac{1}{\sqrt{2}}(Q_{xz} - iQ_{yz}) \tag{2.3.20}$$

$$Q_{-1+1} = \frac{1}{2}(Q_{xx} + Q_{yy} + iQ_{xy} - iQ_{yx}) \tag{2.3.21}$$

$$Q_{0-1} = -\frac{1}{\sqrt{2}}(Q_{zx} - iQ_{zy}) \tag{2.3.22}$$

$$Q_{00} = Q_{zz} \tag{2.3.23}$$

$$Q_{0+1} = \frac{1}{\sqrt{2}}(Q_{zx} + iQ_{zy}) \tag{2.3.24}$$

$$Q_{+1-1} = \frac{1}{2}(Q_{xx} + Q_{yy} - iQ_{xy} + iQ_{yx}) \tag{2.3.25}$$

$$Q_{+10} = -\frac{1}{\sqrt{2}}(Q_{xz} + iQ_{yz}) \tag{2.3.26}$$

$$Q_{+1+1} = -\frac{1}{2}(Q_{xx} - Q_{yy} + iQ_{xy} + iQ_{yx}) \tag{2.3.27}$$

The spherical basis vectors, Eqs. (2.3.10) - (2.3.12), transform under rotation as the angular momentum states $|1\lambda\rangle$ and, by extension, the spherical tensor components $Q_{\lambda\mu}$ transform under rotation as the product of two angular momentum states $|1\lambda\rangle\,|1\mu\rangle$. Thus, from Eq. (2.3.4), we can define the irreducible components of the quadrupole moment in terms of the spherical components [77, 76]

$$Q_m^{(k)} = \sum_{\lambda=-1}^{1}\sum_{\mu=-1}^{1} C(1,1,k;\lambda,\mu,m)Q_{\lambda\mu} \tag{2.3.28}$$

where the possible values of k are 0, 1 and 2, with $-k \leq m \leq k$. Equivalently, by using Eq. (2.3.6), we can express the same transformation in terms of the Wigner 3-j symbols

$$Q_m^{(k)} = \sum_{\lambda=-1}^{1}\sum_{\mu=-1}^{1} (-1)^{-1+1-m}(2k+1)^{\frac{1}{2}} \begin{pmatrix} 1 & 1 & k \\ \lambda & \mu & -m \end{pmatrix} Q_{\lambda\mu} \tag{2.3.29}$$

In general, any second rank tensor can be reduced in this manner and represented in terms of three irreducible tensors of zeroth, first and second rank. Explicit calculation of the transformation above relates the nine irreducible components to the nine Cartesian components via the following expressions

[76, 78].

$$Q_0^{(0)} = -\frac{1}{\sqrt{3}}\left(Q_{xx} + Q_{yy} + Q_{zz}\right) \tag{2.3.30}$$

$$Q_0^{(1)} = \frac{i}{\sqrt{2}}\left(Q_{xy} - Q_{yx}\right) \tag{2.3.31}$$

$$Q_{\pm 1}^{(1)} = -\frac{1}{2}\left[Q_{xz} - Q_{zx} \pm i\left(Q_{zy} - Q_{yz}\right)\right] \tag{2.3.32}$$

$$Q_0^{(2)} = \frac{1}{\sqrt{6}}\left(2Q_{zz} - Q_{xx} - Q_{yy}\right) \tag{2.3.33}$$

$$Q_{\pm 1}^{(2)} = \frac{1}{2}\left[\mp\left(Q_{xz} + Q_{zx}\right) - i\left(Q_{yz} + Q_{zy}\right)\right] \tag{2.3.34}$$

$$Q_{\pm 2}^{(2)} = \frac{1}{2}\left[\left(Q_{xx} - Q_{yy}\right) \pm i\left(Q_{xy} + Q_{yx}\right)\right] \tag{2.3.35}$$

2.3.3 Rotation Transformations

The irreducible representation of a tensor operator is particularly important because the irreducible components transform under rotation according to the Wigner D-matrices [76, 77]. This allows one to write the irreducible components of the quadrupole moment operator in the laboratory-fixed frame in terms of the components in the molecule-fixed frame as

$$Q_m^{(k)} = \sum_{m'=-k}^{k} (-1)^{m-m'} Q_{m'}^{(k)} D_{-m-m'}^{(k)} \tag{2.3.36}$$

where $D_{-m,-m'}^{(k)}$ are the Wigner D-matrices, and $Q_m^{(k)}$ and $Q_{m'}^{(k)}$ (with $k = 0, 1, 2, ...,$ and $-k \leq m, m' \leq k$) are the spherical irreducible tensor components in the laboratory and molecular reference frames, respectively. The same transformation can be applied to the magnetic dipole moment, which is a rank one tensor. However, the irreducible components of a rank one tensor are more straightforward to define, as they are identical to the spherical components defined by Eqs. (2.3.11) - (2.3.12). In other words we can simply write

$$d_m = \sum_{m'=-1}^{1} (-1)^{m-m'} d_{m'} D_{-m-m'}^{(1)} \tag{2.3.37}$$

with the spherical components of the magnetic dipole moment defined as

$$d_{\pm 1} = \mp\frac{1}{\sqrt{2}}\left(d_x \pm d_y\right) \qquad d_0 = d_z \tag{2.3.38}$$

2.4 Matrix Elements and Intensities

In Sec. 2.2 I established the theoretical basis for the higher order transition moments that to describe the infrared spectrum of many homonuclear molecules. In Sec. 2.2 I presented general expressions for the matrix elements in terms of arbitrary initial and final states. It now remains to evaluate these matrix elements in a concrete basis of molecular eigenstates. In this section I do precisely this, using the basis of rovibronic states available in the Duo program to develop concrete expressions for the absorption intensities that can be implemented programmatically to produce line lists for these higher order transition moments.

I begin by introducing the basis functions used in the Duo program to represent the solution to the rovibronic Schrödinger equation of the molecular Hamiltonian. I will then define the absorption intensity in terms of the matrix elements derived in Sec. 2.2.3, before combining the elements of theory outlined in Secs. 2.2.3 and 2.3 to derive explicit expressions for matrix elements in Eqs. (2.2.33) and (2.2.45).

2.4.1 Rovibronic Wavefunctions in Duo

The original Duo program and its methodology is detailed extensively by Yurchenko et al. [64]. The essential approach is to solve the molecular Schrödinger equation using the Born-Oppenheimer approximation. The electronic Schrödinger equation is assumed to have been solved *a priori*, such that a set of electronic potential energy curves, associated couplings and transition moment curves have been obtained for the electronic states of interest. The nuclear vibrational motion is then solved for each uncoupled electronic state on a discrete spatial grid using the so-called sinc-DVR (discrete variable representation) to obtain a truncated vibrational basis [79–82]. At the same time, the vibrational matrix elements of any coupling functions between electronic states are computed by quadrature integration on the vibrational grid. The rotational motion of the molecule in the laboratory-fixed frame is described by the symmetric top states, which are functions of the Euler angles [83]. The complete coupled rovibronic wavefunction is then represented as an expansion in Hund's case (a) basis states

$$|\phi_i\rangle = |\xi\Lambda\rangle\,|S\Sigma\rangle\,|\xi v\rangle\,|J\Omega M\rangle \tag{2.4.1}$$

where i is an index over all basis states, J is the total angular momentum quantum number, M is the projection of the total angular momentum $\vec{J}$ on the laboratory Z-axis, S is the total electronic spin angular momentum quantum number, Σ is the projection of the electronic spin angular momentum vector $\vec{S}$ on the molecular z-axis, ξ indexes the electronic states, Λ is the projection

of the electronic orbital angular momentum vector on the molecular z-axis, $\Omega = \Lambda + \Sigma$ is the projection of the total angular momentum vector on the molecular z-axis, and v is the vibrational quantum number.

The full molecular Hamiltonian, including any coupling terms between electronic states, is then built in the basis of Eq. (2.4.1), and subsequently diagonalised to obtain the final eigenstates, corresponding to the rotational, vibrational and electronic energy levels of the molecule as linear combinations of the basis states

$$|\Psi_{JM\tau}\rangle = \sum_{\xi\Lambda S\Sigma v\Omega} C_{J\tau}(\xi\Lambda S\Sigma v\Omega)\,|\xi\lambda\rangle\,|S\Sigma\rangle\,|\xi v\rangle\,|J\Omega M\rangle \tag{2.4.2}$$

where $C_{J\tau}(\xi\Lambda S\Sigma v\Omega) = C_{J\tau}(\phi)$ are the expansion coefficients obtained through the variational solution to the coupled Schrödinger equation. In the case of heteronuclear diatomic molecules, τ represents the parity $\tau = -$ (odd) or $\tau = +$ (even) of the wavefunction with respect to an inversion or, equivalently, a reflection through the molecule-fixed xz plane. For homonuclear molecules, the symmetry τ also describes the parity with respect to a permutation of the nuclei, and includes the g/u parity (molecule-fixed inversion), where g and u stand for "gerade" and "ungerade", respectively. In general, the good quantum numbers are J, τ and the g/u parity, however other quantum numbers are assigned on the basis of the largest coefficient $C_{J\tau}(\phi)$ in the expansion (2.4.2) [64].

2.4.2 Einstein *A* Coefficients

I begin by relating the matrix elements derived in Sec. 2.2.3 to the absorption intensity of the transitions they produce. The derivation of this relationship has been treated extensively in the literature, in the present context it suffices to note that the intensity of a transition, regardless of the mechanism that generates that transition, can be related to the Einstein A coefficient for spontaneous emission by the following expression

$$I_{\text{fi}} = \frac{1}{8\pi c}\frac{e^{-E_i\beta}\left(1 - e^{-hc\nu_{\text{fi}}\beta}\right)}{\nu_{\text{fi}}^2 Q(T)} g_{\text{ns}}(2J_f + 1)A_{\text{fi}} \tag{2.4.3}$$

where ϕ_f and ϕ_i are defined as in Eq. 2.4.2, and index the basis states that contribute to a given J, τ eigenstate, E_i and E_f are the energies of the initial and final states, respectively, $\nu_{fi} = (E_f - E_i)/hc$ is the transition wavenumber, $\beta = 1/k_{\text{B}}T$ with the k_{B} the Boltzmann factor and T the temperature, $Q(T)$ is the partition function and g_{ns} is the nuclear spin statistical weight factor. In particular, note that Eq.(2.4.3) illustrates the temperature-dependent nature of molecular absorption. Briefly, in order for a population of molecules to absorb a photon of energy with frequency ν_{fi} by transitioning from some initial

state to some higher energy final state, there must be some of that population occupying the initial state prior to the absorption. Thus the intensity of a transition depends on the initial distribution of molecules across the various molecular eigenstates. In general this distribution can be shown to have a statistical dependence on temperature, via the Boltzmann distribution, and also depends on the multiplicity of states with a given energy.

The Einstein coefficients are particularly useful because they are given in units of s^{-1} and so are invariant in all systems of units. The form of the Einstein A-coefficient in Eq. (2.4.3) can be obtained in terms of the transition moments given by Eqs. (2.2.20), (2.2.33), and (2.2.45) from a quantum electrodynamic treatment [84].

$$A_{\text{fi}}^{(\text{E1})} = \frac{\omega_{\text{fi}}^3}{3\pi\varepsilon_0\hbar c^3}\left|\vec{D}_{\text{fi}}\right|^2 = \frac{16\pi^3\nu_{\text{fi}}^3}{3\varepsilon_0 hc^3}\frac{1}{(2J_f+1)}S_{\text{fi}}^{(\text{E1})} \tag{2.4.4}$$

$$A_{\text{fi}}^{(\text{M1})} = \frac{\mu_0\omega_{\text{fi}}^3}{3\pi\hbar c^3}\left|\vec{d}_{\text{fi}}\right|^2 = \frac{16\pi^3\mu_0\nu_{\text{fi}}^3}{3hc^3}\frac{1}{(2J_f+1)}S_{\text{fi}}^{(\text{M1})} \tag{2.4.5}$$

$$A_{\text{fi}}^{(\text{E2})} = \frac{\omega_{\text{fi}}^5}{40\pi\varepsilon_0\hbar c^5}\left|Q_{\text{fi}}\right|^2 = \frac{8\pi^5\nu_{\text{fi}}^5}{5\varepsilon_0 hc^5}\frac{1}{(2J_f+1)}S_{\text{fi}}^{(\text{E2})} \tag{2.4.6}$$

Here we have introduced the linestrength S_{fi} which is equal to the the square of the transition moment. We have now established all the requisite elements for evaluating the matrix elements and deriving expressions for the linestrengths in Eqs. (2.4.5) and (2.4.6). I derive first the expression for the electric quadrupole linestrength, and then subsequently that for the magnetic dipole.

2.4.3 Electric Quadrupole Linestrengths

To begin, we take the matrix element and substitute in the rovibronic eigenstates of Eq. (2.4.2), simultaneously replacing the Cartesian Q_{ij} for the irreducible $Q_m^{(2)}$

$$\langle\Psi_f|\hat{Q}|\Psi_i\rangle = \sum_{\phi_f} C^*_{J_f\tau_f}(\phi_f)\sum_{\phi_i} C_{J_i\tau_i}(\phi_i)\sum_{\rho,\sigma}\sum_{k,m} T_{\rho\sigma,km}\,\langle\phi_f|Q_m^{(k)}|\phi_i\rangle \tag{2.4.7}$$

where the coefficients $T_{\rho\sigma,km}$ are the transformation coefficients defined by Eqs. (2.3.19) - (2.3.27). The next step is to rotate the quadrupole operator from the space-fixed frame to the molecule-fixed frame using the transformation in terms of the Wigner D-matrices defined by Eq. (2.3.36). The quadrupole operator acts only on the electronic coordinates, whilst the Wigner D-matrices are rotational operators that act on the angular momentum states. Thus, the matrix element can be separated into a product of its molecule-fixed and space-

fixed components

$$\langle \Psi_f | \hat{Q} | \Psi_i \rangle = \sum_{\varphi_f} C^*_{J_f \tau_f}(\varphi_f) \sum_{\varphi_i} C_{J_i \tau_i}(\varphi_i) \sum_{\rho,\sigma} \sum_{k,m} T_{km,\rho\sigma} \sum_{m'} \delta_{S_f S_i} \delta_{\Sigma_f \Sigma_i} (-1)^{m-m'} \langle v_f | \langle \xi_f \Lambda_f | Q^{(k)}_{m'} | \xi_i \Lambda_i \rangle | v_i \rangle \langle J_f M_f \Omega_f | D^{(k)}_{-m-m'} | J_i M_i \Omega_i \rangle \quad (2.4.8)$$

The electronic matrix element is obtained *a priori* from electronic structure calculations and provided as input to the Duo program in the form of a quadrupole moment coupling curve that depends on the nuclear bond length.

$$\langle \xi_f \Lambda_f | Q^{(k)}_{m'} | \xi_i \Lambda_i \rangle \coloneqq Q^{(k)}_{m'}(R; \xi_f, \Lambda_f, \xi_i, \Lambda_i) \quad (2.4.9)$$

The vibrational matrix elements are obtained by integrating this function over the vibrational basis. The action of the Wigner D-matrices on the angular momentum eigenstates is

$$|JM\Omega\rangle = (-1)^{M-\Omega} \left(\frac{2J+1}{8\pi^2} \right)^{\frac{1}{2}} D^{(J)}_{-M-\Omega} \quad (2.4.10)$$

$$\langle JM\Omega| = \left(\frac{2J+1}{8\pi^2} \right)^{\frac{1}{2}} D^{(J)}_{M\Omega} \quad (2.4.11)$$

Thus the rotational component of the matrix element can be written as the product of two Wigner 3-j matrices

$$\langle \Psi_f | \hat{Q} | \Psi_i \rangle = \sum_{\varphi_f} C^*_f(\varphi_f) \sum_{\varphi_i} C_i(\varphi_i) \sum_{\rho,\sigma} \sum_{k,m} T_{km,\rho\sigma} \sum_{m'} \delta_{S_f S_i} \delta_{\Sigma_f \Sigma_i} (-1)^{m-m'} (-1)^{M_i - \Omega_i} \langle v_f | \langle \xi_f \Lambda_f | Q^{(k)}_{m'} | \xi_i \Lambda_i \rangle | v_i \rangle [(2J_f+1)(2J_i+1)]^{\frac{1}{2}} \begin{pmatrix} J_i & J_f & k \\ -M_i & M_f & -m \end{pmatrix} \begin{pmatrix} J_i & J_f & k \\ -\Omega_i & \Omega_f & -m' \end{pmatrix} \quad (2.4.12)$$

where the following property has been used [77]

$$\int D^C_{cc'} D^A_{aa'} D^B_{bb'} \sin\beta \, \mathrm{d}\beta \, \mathrm{d}\alpha \, \mathrm{d}\gamma = 8\pi^2 \begin{pmatrix} A & B & C \\ a & b & c \end{pmatrix} \begin{pmatrix} A & B & C \\ a' & b' & c' \end{pmatrix} \quad (2.4.13)$$

with α, β, and γ the Euler angles. This in turn allows us to define the selection rules for electric quadrupole transitions from the properties of the Wigner 3j-symbols, Eqs. (2.3.8) - (2.3.9)

$$\Delta J = J_f - J_i = 0, \pm 1, \pm 2 \quad (2.4.14)$$

and $\Delta S = \Delta\Sigma = 0$, such that

$$\Delta\Lambda = \Lambda_f - \Lambda_i = -m = 0, \pm 1, \pm 2 \quad (2.4.15)$$

In addition to the following symmetry selection rules,

$$+ \leftrightarrow +, \quad - \leftrightarrow - \tag{2.4.16}$$

$$g \leftrightarrow g, \quad u \leftrightarrow u, \tag{2.4.17}$$

which are enforced due to the symmetry of the quadrupole moment operator under coordinate inversion (see Eq. (2.2.47)), and the requirement that the total matrix element is also symmetric under coordinate inversion.

Independent Quadrupole Components

In Sec. 2.3.2 we derived the transformation from the nine Cartesian components of a second rank tensor to the nine irreducible components of the same tensor. These relations hold in general, for any rank two tensor. However, in the present case of the quadrupole moment tensor we can make additional simplifications to reduce the number of independent components. The quadrupole moment was defined in Eq. (2.2.47) as rank two tensor, it is straightforward to see by exchanging the indices i, j that the quadrupole moment is a symmetric tensor

$$Q_{ij} = Q_{ji} \tag{2.4.18}$$

Additionally, the quadrupole was defined in such a way as to ensure that it has zero trace

$$Q_{xx} + Q_{yy} + Q_{zz} = 0 \tag{2.4.19}$$

Thus, there are only five linearly independent Cartesian components. Moreover, we can substitute these properties into Eqs. (2.3.30) - (2.3.35) to show that

$$Q_0^{(0)} = Q_m^{(1)} = 0 \tag{2.4.20}$$

In other words, only the second rank components of the irreducible representation, $Q_m^{(2)}$, are non-zero. So that Eq. (2.4.12) can be reduced to

$$\begin{aligned}\langle \Psi_f | \hat{Q} | \Psi_i \rangle = &\sum_{\varphi_f} C_f^*(\varphi_f) \sum_{\varphi_i} C_i(\varphi_i) \sum_{\rho,\sigma} \sum_m T_{2m,\rho\sigma} \\ &\sum_{m'} \delta_{S_f S_i} \delta_{\Sigma_f \Sigma_i} (-1)^{m-m'} (-1)^{M_i - \Omega_i} \langle v_f | \langle \xi_f \Lambda_f | Q_{m'}^{(2)} | \xi_i \Lambda_i \rangle | v_i \rangle \\ &[(2J_f+1)(2J_i+1)]^{\frac{1}{2}} \begin{pmatrix} J_i & J_f & 2 \\ -M_i & M_f & -m \end{pmatrix} \begin{pmatrix} J_i & J_f & 2 \\ -\Omega_i & \Omega_f & -m' \end{pmatrix}\end{aligned} \tag{2.4.21}$$

With the second rank irreducible tensor components expressed simply in terms of the five independent Cartesian components as

$$Q_0^{(2)} = \frac{3}{\sqrt{6}} Q_{zz} \tag{2.4.22}$$

$$Q_{\pm 1}^{(2)} = \mp Q_{xz} - i Q_{yz} \tag{2.4.23}$$

$$Q_{\pm 2}^{(2)} = \pm i Q_{xy} + Q_{xx} \tag{2.4.24}$$

Laboratory Frame Components

Before turning to the magnetic dipole moment linestrengths, it is worth noting that the expression given by Eq. (2.4.12) can be simplified considerably when explicit knowledge of the value of the matrix elements in the molecule frame is not required. The following standard property implies the 3-j symbols containing M_i, M_f and m, which arise as a result of Eq. (2.4.13), can be summed over M_f, M_i and m and eliminated from Eq. (2.4.21)

$$\sum_{m=-k}^{k} \sum_{M'=-J'}^{J'} \sum_{M''=-J''}^{J''} \begin{pmatrix} J'' & k & J' \\ M'' & m & -M' \end{pmatrix}^2 = 1 \tag{2.4.25}$$

This simplifies the line strength expression to the following

$$S_{\mathrm{fi}}^{(\mathrm{E2})} = g_{\mathrm{ns}}(2J_i+1)(2J_f+1) \left| \sum_{\varphi_f} C^*_{J_i\tau_i}(\varphi_f) \sum_{\varphi_i} C_{J_f\tau_f}(\varphi_i) \sum_{m'} \delta_{S_fS_i}\delta_{\Sigma_f\Sigma_i} \right.$$
$$\left. \times (-1)^{m'+\Omega_i} \langle v_f| \langle \xi_f\Lambda_f|Q^{(2)}_{m'}|\xi_i\Lambda_i\rangle |v_i\rangle \begin{pmatrix} J_i & J_f & 2 \\ -\Omega_i & \Omega_f & -m' \end{pmatrix} \right|^2 \tag{2.4.26}$$

Note that some applications, such as molecular dynamics calculations with e.g RichMol require explicit knowledge of the space-fixed frame contributions to the matrix elements in Eq. (2.4.12) [85, 86]. In order to support these applications, Duo can perform separate calculations of the space-fixed and molecule-fixed matrix elements, without applying this simplification.

2.4.4 Magnetic Dipole Linestrengths

A treatment of the magnetic dipole moment is considerably simpler, as all rank one tensors are irreducible. Thus we need only transform from the Cartesian to the spherical basis in order to perform a rotation on the magnetic dipole moment, as the spherical components transform directly under rotation according to Eq. (2.3.36). Following Eqs. (2.3.10)-(2.3.12), the spherical components of the magnetic dipole moment are related to the Cartesian components by the following transformations

$$d_{\pm 1} = \mp \frac{1}{\sqrt{2}}(d_x \pm i d_y) \tag{2.4.27}$$

$$d_0 = d_z \tag{2.4.28}$$

A similar treatment to that outlined above for the electric quadrupole moment then results in the following expression for the magnetic dipole matrix elements

$$\begin{aligned}\langle\Psi_f|\hat{d}|\Psi_i\rangle = &\sum_{\varphi_f} C_f^*(\varphi_f)\sum_{\varphi_i} C_i(\varphi_i)\sum_{\rho}\sum_{m} T_{m,\rho}\sum_{m'}\delta_{S_f S_i}\delta_{\Sigma_f\Sigma_i}\\ &(-1)^{m-m'}(-1)^{M_i-\Omega_i}\langle S_f\Sigma_f|\langle v_f|\langle\varepsilon_f\Lambda_f|\hat{L}_{m'}+g_s\hat{S}_{m'}|\varepsilon_i\Lambda_i\rangle|v_i\rangle|S_i\Sigma_i\rangle\\ &[(2J_f+1)(2J_i+1)]^{\frac{1}{2}}\begin{pmatrix}J_i & J_f & 1\\ -M_i & M_f & -m\end{pmatrix}\begin{pmatrix}J_i & J_f & 1\\ -\Omega_i & \Omega_f & -m'\end{pmatrix}\end{aligned} \tag{2.4.29}$$

which can be reduced to the following linestrength expression,

$$\begin{aligned}S_{\mathrm{fi}}^{(\mathrm{M1})} =& g_{ns}(2J_i+1)(2J_f+1)\left|\sum_{\varphi_f} C^*_{J_f\tau_f}(\varphi_f)\sum_{\varphi_i} C_{J_i\tau_i}(\varphi_i)\sum_{m'}(-1)^{m'+\Omega_i}\times\right.\\ &\left.\langle S_f\Sigma_f|\langle v_f|\langle\varepsilon_f\Lambda_f|\hat{L}_{m'}+g_s\hat{S}_{m'}|\varepsilon_i\Lambda_i\rangle|v_i\rangle|S_i\Sigma_i\rangle\begin{pmatrix}J_i & J_f & 1\\ -\Omega_i & \Omega_f & -m'\end{pmatrix}\right|^2\end{aligned} \tag{2.4.30}$$

The key distinction here is that the magnetic dipole matrix elements are functions of the spin wavefunction as well as the electronic states. It is straightforward to separate the matrix element into spin and orbital angular momentum contributions.

$$\begin{aligned}&\langle S_f\Sigma_f|\langle v_f|\langle\varepsilon_f\Lambda_f|\hat{L}_{+1}+g_s\hat{S}_{+1}|\varepsilon_i\Lambda_i\rangle|v_i\rangle|S_i\Sigma_i\rangle\\ &\quad=-\frac{1}{\sqrt{2}}\Big[\langle v_f|\hat{L}_+(r;\xi_i,\xi_f)|v_i\rangle\,\delta_{\Sigma_f\Sigma_i}\delta_{\Lambda_f\Lambda_i+1}\\ &\qquad+g_s\left[S_i(S_i+1)-\Sigma_i(\Sigma_i+1)\right]^{\frac{1}{2}}\delta_{v_fv_i}\delta_{\xi_f\xi_i}\delta_{\Lambda_f\Lambda_i}\delta_{\Sigma_f\Sigma_i+1}\Big]\delta_{S_fS_i}\end{aligned} \tag{2.4.31}$$

$$\begin{aligned}&\langle S_f\Sigma_f|\langle v_f|\langle\varepsilon_f\Lambda_f|\hat{L}_{-1}+g_s\hat{S}_{-1}|\varepsilon_i\Lambda_i\rangle|v_i\rangle|S_i\Sigma_i\rangle\\ &\quad=-\frac{1}{\sqrt{2}}\Big[\langle v_f|\hat{L}_-(r;\xi_i,\xi_f)|v_i\rangle\,\delta_{\Sigma_f\Sigma_i}\delta_{\Lambda_f\Lambda_i-1}\\ &\qquad+g_s\left[S_i(S_i+1)-\Sigma_i(\Sigma_i-1)\right]^{\frac{1}{2}}\delta_{v_fv_i}\delta_{\xi_f\xi_i}\delta_{\Lambda_f\Lambda_i}\delta_{\Sigma_f\Sigma_i-1}\Big]\delta_{S_fS_i}\end{aligned} \tag{2.4.32}$$

$$\begin{aligned}&\langle S_f\Sigma_f|\langle v_f|\langle\varepsilon_f\Lambda_f|\hat{L}_0+g_s\hat{S}_0|\varepsilon_i\Lambda_i\rangle|v_i\rangle|S_i\Sigma_i\rangle\\ &\quad=(\Lambda_i+g_s\Sigma_i)\delta_{v_fv_i}\delta_{\xi_f\xi_i}\delta_{\Lambda_f\Lambda_i}\delta_{S_fS_i}\delta_{\Sigma_f\Sigma_i}\end{aligned} \tag{2.4.33}$$

Here we have taken the additional step of replacing the spherical operators $\hat{L}_{\pm1}$ and $\hat{S}_{\pm1}$ with the raising and lowering operators $\hat{L}_\pm$ and $\hat{S}_\pm$, as well as the diagonal operators $\hat{L}_0$ and $\hat{S}_0$ with the projection operators on the molecular z-axis. A difference emerges here in the way the orbital and spin angular momentum contributions to the total magnetic dipole moment are treated. The former is obtained from electronic structure calculations, as a function of the internuclear distance in the same way as other coupling curves and potential energy curves are obtained. The latter can be evaluated analytically in the Hund's case (a) basis.

Chapter 3

Line List Methodology

3.1 Introduction

In the previous chapter I derived expressions for the matrix elements, line strengths, and absorption intensities of electric quadrupole and magnetic dipole transitions in diatomic molecules. In this section I will outline the overall methodology for producing a molecular line list within the framework of the Duo program. I will begin by outlining the Born-Oppenheimer approximation, which is applied in order to separate the nuclear and electronic degrees of freedom. This allows us to solve the electronic Schrödinger equation independently of the nuclear motion. The electronic Schrödinger equation can be solved in this way for a range of nuclear geometries to construct the so-called electronic potential energy curves (PECs), which describe the electronic energy as a function of nuclear geometry. These potential energy curves can subsequently be used to solve the nuclear Schrödinger equation and obtain the rotational and vibrational energy levels. This is usually done by assuming that the nuclear motion evolves on a single non-interacting electronic potential, which is known as the adiabatic approximation.

In this chapter I will also briefly outline how to obtain the adiabatic approximation and will subsequently highlight the conditions under which this approximation breaks down for the case of diatomic molecules. I will detail the method used in this thesis to treat the avoided crossings that arise from the associated non-adiabatic behaviour. In particular, how transforming the electronic structure properties, including PECs, EQMCs, EAMCs and SOCs, to the diabatic representation allows the Duo program to solve the nuclear Schrödinger equation on non-interacting PECs, even in the presence of an avoided crossing. Subsequently, I will detail the method by which the electronic structure properties obtained from quantum chemistry programs can be transformed to a representation compatible with the Hund's case (a) basis employed by the Duo program. For the particular case of the quadrupole moment oper-

ator I will apply symmetry properties and selection rules to reduce the number of components of the quadrupole moment operator that must be calculated to just one independent component for a given pair of electronic states. Finally I will briefly outline the method of solving the nuclear Schrödinger equation employed by the Duo program before detailing the structure of the input to the Duo program required to calculate the electric quadrupole and magnetic dipole moment intensities, with concrete examples of the program control.

3.2 Solving the Schrödinger Equation

In general the wavefunction for a diatomic molecule with N_e electrons contains $3N_e + 6$ degrees of freedom, and is therefore computationally intractable for most systems of interest. Separation of the nuclear and electronic degrees of freedom allows one to solve the electronic Schrödinger equation independently of the nuclear motion, and to reduce the computational complexity further by introducing additional approximations for the electronic structure calculations. The nuclear Schrödinger equation can then be solved using a potential energy surface obtained by solving the electronic Schrödinger equation at various nuclear geometries. This separation of the nuclear and electronic degrees of freedom is only possible because the motion of the more massive nuclei occurs on a timescale that is orders of magnitude slower than that of the lighter electrons. This means that the nuclear motion can be approximated as occuring on a single potential energy surface that evolves adiabatically as the nuclear coordinates are varied. If the nuclei are sufficiently massive, the non-adiabatic interactions can be neglected entirely.

3.2.1 Born-Oppenheimer Approximation

I start by outlining the Born-Oppenheimer approximation that gives rise to the adiabatic representation of the electronic properties, beginning with the Schrödinger equation with the rovibronic molecular Hamiltonian

$$\hat{H}_{\text{tot}} |\Psi\rangle = E_{\text{tot}} |\Psi\rangle \tag{3.2.1}$$

The rotational-vibrational-electronic (rovibronic) motion of a diatomic molecule in the absence of an external electromagnetic field, and neglecting nuclear spin contributions is described by a Hamiltonian of the form [87–90]:

$$\begin{aligned}\hat{H}_{\text{tot.}} = &-\frac{\hbar^2}{2m_e}\sum_{i=1}^{N_e}\nabla_i^2 - \frac{\hbar^2}{2}\sum_{\alpha=1}^{2}\frac{1}{M_\alpha}\nabla_\alpha^2 + \frac{1}{4\pi\epsilon_0}\sum_{i=1}^{N_e}\sum_{j=1}^{i-1}\frac{e^2}{|\hat{r}_i - \hat{r}_j|} \\ &+ \frac{e^2}{4\pi\epsilon_0}\frac{Z_1 Z_2}{|\hat{R}_1 - \hat{R}_2|} - \frac{e^2}{4\pi\epsilon_0}\sum_{i=1}^{N_e}\sum_{\alpha=1}^{2}\frac{Z_\alpha}{|\hat{r}_i - \hat{R}_\alpha|}\end{aligned} \tag{3.2.2}$$

The first term is the kinetic energy of the N_e electrons, the second term is that of the two nuclei, with masses M_i and atomic numbers Z_i, and the remaining three Coulombic terms are the electron-electron repulsion, the electron-nucleus attraction and the nucleus-nucleus repulsion, with $\hat{r}_i$ and $\hat{R}_i$ the position operators acting on the electron coordinates and the nuclear coordinates, respectively.

$$\hat{T}_{\mathrm{e}} = -\frac{\hbar^2}{2m_e}\sum_{i=1}^{N_e}\nabla_i^2 \tag{3.2.3}$$

$$\hat{T}_{\mathrm{n}} = -\frac{\hbar^2}{2}\sum_{\alpha=1}^{2}\frac{1}{M_\alpha}\nabla_\alpha^2 \tag{3.2.4}$$

$$\hat{V}_{\mathrm{ee}} = \frac{1}{4\pi\epsilon_0}\sum_{i=1}^{N_e}\sum_{j=1}^{i-1}\frac{e^2}{|\hat{r}_i - \hat{r}_j|} \tag{3.2.5}$$

$$\hat{V}_{\mathrm{nn}} = \frac{e^2}{4\pi\epsilon_0}\frac{Z_1 Z_2}{|\hat{R}_1 - \hat{R}_2|} \tag{3.2.6}$$

$$\hat{V}_{\mathrm{ne}} = -\frac{e^2}{4\pi\epsilon_0}\sum_{i=1}^{N_e}\sum_{\alpha=1}^{2}\frac{Z_i}{|\hat{r}_i - \hat{R}_\alpha|} \tag{3.2.7}$$

The eigenstates of this Hamiltonian represent an exact solution to the interacting many-body problem, and precisely specify the exact molecular wavefunction. In its complete form, the nuclear-electron Coulomb interaction $\hat{V}_{\mathrm{ne}}$ ensures that the electronic and nuclear degrees of freedom are coupled, such that the molecular Hamiltonian is not separable into a sum of electronic and nuclear components. However, due to the orders-of-magnitude difference between the masses of the nuclei and electrons, a good approximation is to treat the nuclei as fixed in space on the timescale of electronic dynamics. In this limit of fixed nuclear coordinates the position operators $\hat{R}_\alpha$ are replaced by constant position vectors $\vec{R}_\alpha$,[91]

$$\hat{V}_{\mathrm{nn}} \longrightarrow \frac{e^2}{4\pi\epsilon_0}\frac{Z_1 Z_2}{|\vec{R}_1 - \vec{R}_2|} \tag{3.2.8}$$

$$\hat{V}_{\mathrm{ne}} \longrightarrow -\frac{e^2}{4\pi\epsilon_0}\sum_{i=1}^{N_e}\sum_{j=1}^{2}\frac{Z_i}{|\hat{r}_i - \vec{R}_j|} \tag{3.2.9}$$

The potential energy terms $\hat{V}_{nn}$ and $\hat{V}_{ne}$ thus become only *parametrically* dependent on the nuclear coordinates. The total Hamiltonian can then be separated into nuclear and electronic terms

$$\hat{H}_{\mathrm{tot.}} = \hat{H}_{\mathrm{elec.}} \otimes \hat{H}_{\mathrm{nucl.}} \longrightarrow \hat{H}_{\mathrm{elec.}} + \hat{H}_{\mathrm{nucl.}} \tag{3.2.10}$$

with the electronic Hamiltonian given by the sum of the potential energy and kinetic energy terms,

$$\hat{H}_{\mathrm{elec.}} = \hat{T}_e + \hat{V}_{ee} + \hat{V}_{nn} + \hat{V}_{ne} = \hat{T}_e + V(\vec{r};\vec{R}) \tag{3.2.11}$$

where $\vec{R} = \{\vec{R}_\alpha\}$ is the complete set of nuclear coordinates, $\vec{r} = \{\vec{r}_i\}$ the complete set of electronic coordinates. In the limit of clamped nuclei the $\hat{V}_{\text{nn}}$ term becomes an additive constant energy that plays no part in the dynamic problem and so can be absorbed into the potential energy term without loss of generality. The eigenfunctions of $\hat{H}_{\text{elec.}}$ are the stationary electronic eigenstates, $\{|\phi_k\rangle\}$. For a given nuclear configuration (i.e a fixed value of $\vec{R}$) the Schrödinger equation for the electronic motion is

$$\hat{H}_{\text{elec.}}(\vec{R})\,|\phi_k;\vec{R}\rangle = E_k(\vec{R})\,|\phi_k;\vec{R}\rangle \tag{3.2.12}$$

where the parametric dependence of the $|\phi_k\rangle$ has been made explicit, and n is a running index over the electronic states. When the dependence of the electronic eigenstates on $\vec{R}$ is parametric, it is straightforward to show that the operators $\hat{R} = |\hat{R}_1 - \hat{R}_2|$ and $\hat{H}_{\text{elec.}}$ commute, such that the basis states of the total molecular Hamiltonian can be written as

$$|\vec{R},\phi_k;\vec{R}\rangle = |\vec{R}\rangle\left|\phi_k;\vec{R}\right\rangle \tag{3.2.13}$$

where $|\vec{R}\rangle$ are the eigenstates of $\hat{R}$. Using this fact, we can obtain the nuclear eigenstates by projecting the total wavefunction Ψ, onto real space

$$\begin{aligned}
\Psi(\vec{r},\vec{R}) &= \langle\vec{r},\vec{R}|\Psi\rangle && (3.2.14)\\
&= \sum_k \langle\vec{r},\vec{R}|\phi_k;\vec{R}\rangle\left\langle\phi_k;\vec{R}\middle|\Psi\right\rangle && (3.2.15)\\
&= \sum_k \left\langle\vec{r}\middle|\phi_k;\vec{R}\right\rangle\langle\vec{R}|\,\langle\phi_k;\vec{R}|\Psi\rangle && (3.2.16)\\
&= \sum_k \left\langle\vec{r}\middle|\phi_k;\vec{R}\right\rangle\langle\vec{R},\phi_k;\vec{R}|\Psi\rangle && (3.2.17)\\
&= \sum_k \phi_k(\vec{r};\vec{R})\chi_k(\vec{R}) && (3.2.18)
\end{aligned}$$

where the resolution of identity $\sum_n \left|\phi_k;\vec{R}\right\rangle\!\!\left\langle\phi_k;\vec{R}\right|$ has been used. In other words, we have expanded the total molecular wavefunction in the basis of eigenfunctions of the electronic Hamiltonian, and defined

$$\langle\vec{r}|\phi_k;R\rangle = \phi_k(\vec{r};R) \tag{3.2.19}$$

$$\langle\vec{R},\phi_k;R|\Psi\rangle = \chi_n(\vec{R}) \tag{3.2.20}$$

We can identify $|\chi_k\rangle$ as the eigenstates of the nuclear Schrödinger equation. Hereafter we drop the explicit dependence on the nuclear and electronic coordinates from the notation for convenience. Substituting the molecular wavefunction above into Eq. (3.2.1), and applying $\langle\phi|_{k'}$ we obtain the Schrödinger equation in the following form

$$\langle\phi_{k'}|\left[\hat{H}_{\text{elec.}} + \hat{T}_{\text{nucl.}}\right]\sum_k |\phi_k\rangle\,|\chi_k\rangle = E_{\text{tot.}}\sum_k \langle\phi_{k'}|\phi_k\rangle\,|\chi_k\rangle \tag{3.2.21}$$

Since the nuclear Hamiltonian acts on both the nuclear and electronic coordinates, we must apply the chain rule to obtain the action of $\hat{T}_{\text{nucl.}}$

$$\hat{T}_{\text{nucl.}} |\phi_k\rangle |\chi_k\rangle = -\frac{\hbar^2}{2} \sum_{\alpha=1}^{2} \frac{1}{M_\alpha} \left(|\phi_k\rangle \nabla_\alpha^2 |\chi_k\rangle + 2\nabla_\alpha |\phi_k\rangle \nabla_\alpha |\chi_k\rangle + |\chi_k\rangle \nabla_\alpha^2 |\phi_k\rangle \right) \tag{3.2.22}$$

Given that the electronic eigenfunctions are orthonormal such that $\langle \phi_{k'} | \phi_k \rangle = \delta_{k'k}$, we can write for the electronic Hamiltonian

$$\langle \phi_{k'} | \hat{H}_{\text{elec.}} | \phi_k \rangle |\chi_k\rangle = E_{\text{elec.},k'} \delta_{k'k} |\chi_{k'}\rangle \tag{3.2.23}$$

Substituting these into Eq.(3.2.21), we obtain

$$\sum_k \Bigg[E_{\text{elec.},k'} \delta_{k'k} |\chi_{k'}\rangle - \frac{\hbar^2}{2} \sum_{\alpha=1}^{2} \frac{1}{M_\alpha} \Big(\delta_{k'k} \nabla_\alpha^2 |\chi_k\rangle + 2 \langle \phi_{k'} | \nabla_\alpha | \phi_k \rangle \nabla_\alpha |\chi_k\rangle + \langle \phi_{k'} | \nabla_\alpha^2 | \phi_k \rangle |\chi_k\rangle \Big) \Bigg] = E_{\text{tot}} \sum_k \delta_{k'k} |\chi_{k'}\rangle \tag{3.2.24}$$

Which allows us to define a system of coupled eigenvalue equations that describe the nuclear motion

$$\left[E_{\text{elec.},k'} + \frac{\hbar^2}{2M_\alpha} \nabla_\alpha^2 - \frac{\hbar^2}{2} \sum_k \sum_\alpha \frac{1}{M_\alpha} \left(2 \langle \phi_{k'} | \nabla_\alpha | \phi_k \rangle \nabla_\alpha + \langle \phi_{k'} | \nabla_\alpha^2 | \phi_k \rangle \right) \right] |\chi_{k'}\rangle = E_{\text{tot.}} |\chi_{k'}\rangle \tag{3.2.25}$$

Through the Born-Oppenheimer approximation, we have thus separated the electronic and nuclear equations of motion, Eqs. (3.2.12) and (3.2.25) respectively. The adiabatic approximation allows us to further simplify the solution to the nuclear Schrödinger equation by decoupling the system of equations defined by Eq. (3.2.25).

3.2.2 Adiabatic Approximation

To derive the adiabatic approximation we start by noting that the derivative terms on the left-hand side of Eq. (3.2.25) couple different electronic eigenstates and thus give rise to the non-adiabatic evolution of the nuclear wavefunction. The vector term is known as the (first-order) *derivative coupling*, whilst the scalar term is known as the (second-order) *kinetic coupling*

$$d_{k'k}^\alpha = \langle \phi_{k'} | \nabla_\alpha | \phi_k \rangle \tag{3.2.26}$$

$$D_{k'k}^\alpha = \langle \phi_{k'} | \nabla_\alpha^2 | \phi_k \rangle \tag{3.2.27}$$

These form the elements of two square matrices with dimension equal to the number of electronic eigenstates. The kinetic coupling can be written in terms of the derivative coupling as [92, 91, 93]

$$D^{\alpha}_{k'k} = \sum_{l} d^{\alpha}_{k'l} d^{\alpha}_{lk} + \nabla d^{\alpha}_{k'k} \tag{3.2.28}$$

The adiabatic approximation is made by setting these terms equal to zero, in which case the Schrödinger equation describes a system in which the nuclear motion evolves on a single electronic potential energy surface $V_k(\vec{R}) = E_{\text{elec., k}}$, which depends on the nuclear coordinates

$$\left(\hat{T}_{\text{nucl.}} + V_k(\vec{R})\right) |\chi_k\rangle = E_{\text{tot.}} |\chi_k\rangle \tag{3.2.29}$$

This approximation is valid when the non-adiabatic coupling (NAC) is vanishingly small. Re-writing the first order coupling term, $d^{\alpha}_{k'k}$, in terms of the eigenvalues of the electronic Hamiltonian we obtain the following [94]

$$d^{\alpha}_{k'k} = \frac{\langle \phi_{k'} | \left[\nabla_{\alpha}, \hat{H}_{\text{elec.}}\right] | \phi_k \rangle}{E_k - E_{k'}} \tag{3.2.30}$$

It is immediately apparent from Eqs. (3.2.28) and (3.2.30) that the adiabatic coupling terms are small, and hence the approximation is valid, when two eigenstates are well separated in energy.

Conversely, when two states of the same symmetry and spin multiplicity lie close in energy, such that $E_{k'} \sim E_k$, the Born-Oppenheimer approximation breaks down and the non-adiabatic behaviour must be accounted for. This can be done by explicitly calculating the derivative coupling term, often referred to as the 'non-adiabatic coupling' (NAC) correction [95–97]. In this regime the electronic states become mixed in such a way that the nuclear motion cannot be considered to evolve on a single PEC [98, 94]. In some cases the electronic energies of two states converge and become completely degenerate. In diatomic molecules this results in a so-called 'avoided crossing', where the PECs (and indeed any coupling courves obtained from electronic structure calculations) exhibit strong cusp-like behaviour. Moreover, the NAC becomes singular at the point of the avoided crossing. This poses significant challenges to solving the nuclear equations of motion, and it is often more convenient to transform to the *diabatic basis*, where the avoided crossings can be elminated entirely.

3.2.3 Diabatic Representation

The key advantage of the diabatic representation is that it removes avoided crossings. In the diabatic basis the non-adiabatic behaviour appears in the form of off-diagonal diabatic coupling terms, which are generally broader than

the sharply-peaked NACs. This alleviates the problem of singular values and cusp-like behaviour of NACs in the potential energy operator that couple electronic states [97, 99, 100, 98]. These so-called *diabatic couplings* (DC) can be introduced when constructing the full molecular Hamiltonian after solving the nuclear problem for uncoupled electronic states.

For a diatomic molecule, the diabatisation procedure consists of diagonalising the nuclear kinetic energy operator through the transformation [101, 92],

$$U(R) = \begin{pmatrix} \cos\beta(R) & -\sin\beta(R) \\ \sin\beta(R) & \cos\beta(R) \end{pmatrix} \tag{3.2.31}$$

where $\beta(R)$ is the so-called *mixing angle*. This transformation rotates the adiabatic PECs $\phi_i(\vec{r};R)$ obtained from electronic structure calculations to the diabatic PECs $\varphi_i(\vec{r};R)$ according to

$$\begin{pmatrix} \varphi_1(\vec{r};R) \\ \varphi_2(\vec{r};R) \end{pmatrix} = \begin{pmatrix} \cos\beta(R) & -\sin\beta(R) \\ \sin\beta(R) & \cos\beta(R) \end{pmatrix} \begin{pmatrix} \phi_1(\vec{r};R) \\ \phi_2(\vec{r};R) \end{pmatrix} \tag{3.2.32}$$

The nuclear kinetic energy is diagonal when the derivative couplings with respect to the diabatic eigenstates vanish, i.e [102–104, 101]

$$\tilde{d}^{\alpha}_{k'k} = \langle \varphi_{k'}(\vec{r};R) | \nabla_\alpha | \varphi_k(\vec{r};R) \rangle = 0 \tag{3.2.33}$$

Inserting the φ_i obtained from Eq. (3.2.32) and recognising that $d^{\alpha}_{k'k} = -d^{\alpha}_{kk'}$, we obtain the condition

$$\tilde{d}^{\alpha}_{k'k} = d^{\alpha}_{k'k} - \nabla_\alpha \beta(R) = 0 \tag{3.2.34}$$

and hence the mixing angle can be computed as a function of by integrating the non-adiabatic coupling term over the bond length

$$\beta(R) = \int_{-\infty}^{R} d^{\alpha}_{k'k}(R')\,\mathrm{d}R' \tag{3.2.35}$$

This allows one to reconstruct the transformation matrix given by Eq. (3.2.31). This matrix can subsequently be used to transform the wavefunctions and electronic structure properties (transition moments and potential energy curves) of the two states.

It is worth mentioning at this point that Baer [102] showed that a solution to Eq. (3.2.34) exists only if the curl of $d^{\alpha}_{k'k}$ vanishes. Mead and Truhlar [104] subsequently showed that this is not generally the case for systems with more than one nuclear coordinate, i.e polyatomic molecules with more than two atoms. In this case, exactly diabatic states cannot be obtained, and only a quasi-diabatic transformation is possible.

The Duo program accepts molecular Hamiltonians in either the adiabatic or diabatic representation, and recent work within the ExoMol group has shown that the results obtained in either case are numerically equivalent [105].

3.2.4 Diabatisation Procedure

The diabatisation described in Sec. 3.2.3 can in principal be achieved using a variety of methods. The most obvious approach is to use electronic structure methods to explicitly calculate the NAC given by Eq. (3.2.26) and compute the mixing angle by integrating the NAC according to Eq. (3.2.35). The integration can in turn be performed either by applying a quadrature method to a dense grid of *ab initio* values, or by fitting an analytical form to a smaller sample of points and integrating the fitted curve. In either case, cumbersome and computationally expensive calculations of the NACs at various geometries are required. The alternative is to pursue approximate diabatisation schemes that do not require explicit calculation of the NAC.

One such method relies on reconstructing the NAC through an optimisation procedure that maximises the overlap between the *ab initio* wavefunctions at neighbouring nuclear geometries. This can be achieved directly by maximising the overlap of the computed orbitals [106–111]. This approach is often cumbersome, and requires highly accurate *ab initio* calculations of the so-called 'diabatic molecular orbitals'. An alternative method allows one to maximise the overlap indirectly by requiring the adiabatic electric dipole and quadrupole moments to be smooth functions of the nuclear coordinates [112–115]. The principal drawback of this approach is that it relies on knowledge of both these electronic structure properties.

Recently Baeck and An [116] developed a similar technique that relies only on knowledge of the adiabatic potential energy curves. In their work, the NAC is assumed to have a Lorentzian profile, and the width of the Lorentzian function is then related to the energy separation of the adiabatic potentials at the crossing point of the true diabatic potentials. This crossing point is in turn determined by maximising an approximation of the NAC derived using the linear vibronic coupling model. The advantage of this method is that it requires no additional electronic structure calculations beyond the adiabatic potential energy curves which are, in principal, already computed. This method was shown to be effective in characterising the NAC of several molecules, including the diatomics LiF and C_2. In this thesis I will develop a similar, but numerically simpler, method derived from the assumption that the NAC which maximally diabatises the electronic structure properties is that which minimises the sum over geometries of the second derivatives of those properties in the diabatic representation. The procedure is straightforward and moreover, allows one to diabatise any given electronic structure property without the requirement of auxiliary information.

Firstly a trial form of the NAC function is assumed. For example, a Lorentzian function with some initial width Γ_0 and centre R_0

$$F(R) = \frac{1}{\pi} \frac{{}^1\!/\!_2\Gamma_0}{(R - R_0)^2 + ({}^1\!/\!_2\Gamma_0)^2} \tag{3.2.36}$$

The mixing angle $\beta(R)$ is then calculated according to Eq. (3.2.35) at each nuclear geometry for which the diabatisation is to be applied, which in turn allows one to generate the transformation matrix in Eq. (3.2.32) as a function of nuclear geometry. The diabatic electronic structure properties are then obtained by applying this transformation and the parameters of the NAC are iteratively optimised with the cost function

$$\mathcal{L}(\vec{\theta}) = \sum_{R} \frac{\mathrm{d}^2 d_{k'k}(R;\vec{\theta})}{\mathrm{d}R^2} \tag{3.2.37}$$

the sum of second derivatives for a NAC function parameterised by set of parameters $\vec{\theta}$. This sum can be taken across either some region around the avoided crossing, or over all geometries for which the electronic structure properties have been computed. This method has the advantage of being agnostic to the analytic form of the NAC function, and also of placing no constraints on the position of the crossing.

Diabatisation of Electronic Structure Properties

In the interest of completeness, it is worth expounding how different electronic structure properties transform under the diabatisation described above. The PECs transform between the adiabatic and diabatic representations in the same way as the eigenstates, according to Eq. (3.2.32). However, for electronic structure properties that are obtained as matrix elements of some operator the adiabatic representation at a given nuclear geometry will either form a vector or a matrix, depending on the property in question. When properties are obtained as the matrix element of an operator between two electronic states, and only one of those states exhibits an avoided crossing, the transformation is given by

$$\begin{pmatrix} \langle \psi^{\mathrm{d}} | M | \phi_1^{\mathrm{d}} \rangle \\ \langle \psi^{\mathrm{d}} | M | \phi_2^{\mathrm{d}} \rangle \end{pmatrix} = U \begin{pmatrix} \langle \psi^{\mathrm{a}} | M | \phi_1^{\mathrm{a}} \rangle \\ \langle \psi^{\mathrm{a}} | M | \phi_2^{\mathrm{a}} \rangle \end{pmatrix} \tag{3.2.38}$$

where $|\phi_1\rangle$ and $|\phi_2\rangle$ are the mixed electronic states that we wish to diabatise, and $|\psi\rangle$ is a third state which does not contain an avoided crossing. When the quantity is a matrix element of an operator that couples two states, which both exhibit an avoided crossing the transformation becomes

$$\begin{pmatrix} \langle \psi_1^{\mathrm{d}} | M | \phi_1^{\mathrm{d}} \rangle & \langle \psi_1^{\mathrm{d}} | M | \phi_2^{\mathrm{d}} \rangle \\ \langle \psi_2^{\mathrm{d}} | M | \phi_1^{\mathrm{d}} \rangle & \langle \psi_2^{\mathrm{d}} | M | \phi_2^{\mathrm{d}} \rangle \end{pmatrix} = U^{\dagger} \begin{pmatrix} \langle \psi_1^{\mathrm{a}} | M | \phi_1^{\mathrm{a}} \rangle & \langle \psi_1^{\mathrm{a}} | M | \phi_2^{\mathrm{a}} \rangle \\ \langle \psi_2^{\mathrm{a}} | M | \phi_1^{\mathrm{a}} \rangle & \langle \psi_2^{\mathrm{a}} | M | \phi_2^{\mathrm{a}} \rangle \end{pmatrix} U \tag{3.2.39}$$

This is also the transformation that must be applied to expectation value properties of states with an avoided crossing. In this case the $|\psi\rangle$ in 3.2.39 is replaced by the same $|\phi\rangle$ that forms the ket component.

3.3 Electronic Structure Properties

In the previous section I derived the Born-Oppenheimer approximation and showed how electronic structure properties can be transformed between the adiabatic and diabatic representations. These electronic structure properties form the basis of a molecular line list, and are pre-requisites for solving the nuclear Schrödinger equation within the Duo program. the Born-Oppenheimer approximation, the first step in the production of a molecular line list is to obtain the various electronic properties required to solve the nuclear Schrödinger equation. Namely the potential energy curves and the coupling curves of the various electronic states. The potential energy curves describe the electronic potential energy over a range of nuclear geometries, while the coupling curves describe energy contributions to the Hamiltonian due to various correction terms. These contributions can include various interactions and couplings of electronic states, such as spin-orbit, spin-spin and spin-rotation [64]. Such curves can be obtained empirically, or from *ab initio* electronic structure calculations. The usual procedure is to obtain initial potential energy and coupling curves from *ab initio* calculations, and subsequently refine an analytic form by empirically fitting the calculated state energies to accurate energies obtained by experimental methods. In addition to the potential energy and coupling curves, which determine the electronic energy levels of the molecule, line list calculations also require knowledge of the transition moments, which are similarly calculated *ab initio*.

3.3.1 Transforming to the Hund's Case (a) Basis

In general, the quantum chemistry programs used to perform the electronic structure calculations leverage Abelian point group symmetry to simplify calculations by accounting for the symmetry of the molecular system. The result is that the wavefunctions are expressed in the Cartesian basis with indices corresponding to the generators of the irreducible Abelian point group of that electronic state. The use of Abelian point groups also allows the wavefunction to be expressed in terms of real-valued components, which is often desireable for electronic structure calculations.

In this section I will briefly outline the procedure used to transform to matrix elements of tensor operators between the representation of these electronic properties used by electronic structure programs, and that used by the Duo program to calculate the line strengths as given by Eqs. 2.4.26 and Eqs. 2.4.30. I will also derive explicit expressions for the matrix elements of the irreducible spherical tensor components in terms of the Cartesian matrix elements commonly produced by quantum chemistry programs.

The potential energy curves, quadrupole moment curves, and other elec-

tronic structure properties are expressed in the Cartesian basis

$$F|_{\vec{R}} = \langle \rho\Sigma|\hat{F}|\sigma\Sigma'\rangle\,|_{\vec{R}} \tag{3.3.1}$$

where $\vec{R}$ is a given nuclear geometry, and ρ, σ denote the Cartesian components of the electronic wavefunction, for example $|\Pi_x\rangle$ and $|\Pi_y\rangle$ for $|\Lambda| = 1$ states or $|\Delta_{xx}\rangle$ and $|\Delta_{xy}\rangle$ for $|\Lambda| = 2$ states. The Duo program, by contrast, expects a Hund's case (a) representation of the wavefunction [64]

$$F|_{\vec{R}} = \langle \Lambda\Sigma|\hat{F}|\Lambda'\Sigma'\rangle\,|_{\vec{R}} \tag{3.3.2}$$

The Duo wavefunctions are eigenstates of the $\hat{L}_z$ operator, and hence have well-defined values of the orbital electronic angular momentum projection on the z-axis

$$|\pm|\Lambda|\Sigma\rangle = C_\rho^{\pm|\Lambda|}\,|\rho\Sigma\rangle \pm C_\sigma^{\pm|\Lambda|}\,|\sigma\Sigma\rangle \tag{3.3.3}$$

The coefficients $C_\rho^{\pm|\Lambda|}$ and $C_\sigma^{\pm|\Lambda|}$, and hence transformation of the electronic structure properties from the Cartesian representation to the so-called Λ representation can be obtained by diagonalizing the $\hat{L}_z$ operator in the Cartesian basis. In order to preserve the relative phases of the electronic wavefunctions and electronic structure properties the Cartesian components $|\rho\Sigma\rangle$ and $|\sigma\Sigma\rangle$ can be chosen such that the $\hat{L}_z$ operator has the following form, up to an arbitrary phase for states with $|\Lambda| > 0$

$$\hat{L}_z^{\text{Cartesian}} = \begin{pmatrix} \langle\rho\Sigma|\hat{L}_z|\rho\Sigma\rangle & \langle\rho\Sigma|\hat{L}_z|\sigma\Sigma\rangle \\ \langle\sigma\Sigma|\hat{L}_z|\rho\Sigma\rangle & \langle\sigma\Sigma|\hat{L}_z|\sigma\Sigma\rangle \end{pmatrix} = \begin{pmatrix} 0 & -i\hbar|\Lambda| \\ i\hbar|\Lambda| & 0 \end{pmatrix} \tag{3.3.4}$$

The corresponding unitary matrix that diagonalizes this operator is

$$U = \frac{1}{\sqrt{2}}\begin{pmatrix} 1 & i \\ 1 & -i \end{pmatrix} \tag{3.3.5}$$

$$F^\Lambda = U^\dagger F^{\text{Cartesian}} U \tag{3.3.6}$$

Thus, the potential energy and coupling curves obtained from electronic structure calculations can be expressed in the Λ representation by applying the basis transformation described by U at each nuclear geometry.

3.3.2 Independent Components of the Electric Quadrupole

In Sec. 2.3.2 we established the relationship between the Cartesian components and the irreducible components of the quadrupole moment tensor. Now, by applying the properties of the Abelian symmetry groups, we can identify the non-zero Cartesian components that couple electronic states of different symmetries. We first note that the irreducible Abelian representation of a matrix element of a given operator coupling electronic states i and f, each with

irreducible Abelian representations G_i and G_f respectively, must be contained within the Abelian group given by the direct product $G_i \times G_f$ [78]. This allows us to form the product tables 3.1 and 3.2.

Then by identifying the irreducible representation of the different electronic states, we can make the following identifications for relationship between the Cartesian and Λ representations of the electric quadrupole moments

$$\begin{aligned}\langle \pm|\Lambda||Q_0^{(2)}|\pm|\Lambda|\rangle &= \frac{3}{2\sqrt{6}}\big[\,\langle\alpha|Q_{zz}|\alpha\rangle + \langle\beta|Q_{zz}|\beta\rangle\,\big] \\ &= \frac{3}{\sqrt{6}}\langle\alpha|Q_{zz}|\alpha\rangle\,,\end{aligned} \tag{3.3.7}$$

$$\begin{aligned}\left\langle \Sigma^+\middle|Q_{\pm1}^{(2)}\middle|\mp\Pi\right\rangle &= \mp\frac{1}{\sqrt{2}}\big[\,\left\langle \Sigma^+\middle|Q_{xz}\middle|\Pi_x\right\rangle + \left\langle \Sigma^+\middle|Q_{yz}\middle|\Pi_y\right\rangle\,\big] \\ &= \mp\sqrt{2}\left\langle \Sigma^+\middle|Q_{xz}\middle|\Pi_x\right\rangle,\end{aligned} \tag{3.3.8}$$

$$\begin{aligned}\left\langle \Sigma^-\middle|Q_{\pm1}^{(2)}\middle|\mp\Pi\right\rangle &= -\frac{i}{\sqrt{2}}\big[\,\left\langle \Sigma^-\middle|Q_{xz}\middle|\Pi_y\right\rangle + \left\langle \Sigma^-\middle|Q_{yz}\middle|\Pi_x\right\rangle\,\big] \\ &= -i\sqrt{2}\left\langle \Sigma^-\middle|Q_{xz}\middle|\Pi_y\right\rangle,\end{aligned} \tag{3.3.9}$$

$$\begin{aligned}\left\langle \Sigma^+\middle|Q_{\pm2}^{(2)}\middle|\mp\Delta\right\rangle &= +\frac{1}{\sqrt{2}}\big[\,\left\langle \Sigma^+\middle|Q_{xx}\middle|\Delta_{xx}\right\rangle + \left\langle \Sigma^+\middle|Q_{xy}\middle|\Delta_{xy}\right\rangle\,\big] \\ &= +\sqrt{2}\left\langle \Sigma^+\middle|Q_{xx}\middle|\Delta_{xx}\right\rangle,\end{aligned} \tag{3.3.10}$$

$$\begin{aligned}\left\langle \Sigma^-\middle|Q_{\pm2}^{(2)}\middle|\mp\Delta\right\rangle &= \pm\frac{i}{\sqrt{2}}\big[\,\left\langle \Sigma^-\middle|Q_{xx}\middle|\Delta_{xy}\right\rangle + \left\langle \Sigma^-\middle|Q_{xy}\middle|\Delta_{xx}\right\rangle\,\big] \\ &= \pm i\sqrt{2}\left\langle \Sigma^-\middle|Q_{xx}\middle|\Delta_{xy}\right\rangle,\end{aligned} \tag{3.3.11}$$

$$\begin{aligned}\langle\mp\Pi|Q_{\pm1}^{(2)}|\mp\Delta\rangle &= \mp\frac{1}{2}\big[\,\langle\Pi_x|Q_{xz}|\Delta_{xx}\rangle + \langle\Pi_x|Q_{yz}|\Delta_{xy}\rangle - \\ &\qquad \langle\Pi_y|Q_{yz}|\Delta_{xx}\rangle + \langle\Pi_y|Q_{xz}|\Delta_{xy}\rangle\,\big] \\ &= \mp 2\,\langle\Pi_x|Q_{xz}|\Delta_{xx}\rangle\,,\end{aligned} \tag{3.3.12}$$

Here we have made use of the 3-j symbol in Eq. (2.4.26), which ensures that each irreducible quadrupole component couples electronic states with $\Delta\Lambda = m'$. The first lines in the expressions above are obtained from Eqs. (2.3.33)-(2.3.35) by substituting the symmetric components $Q_{zx} = Q_{xz}$, $Q_{zx} = Q_{yz}$, $Q_{xy} = Q_{yx}$, and $Q_{xx} = -Q_{yy}$. The second line in each expression is obtained by setting matrix elements that do not satisfy the selection rule in Eq. (2.4.15) (e.g $\langle\Sigma^+|Q_{\mp1}^{(2)}|\mp\Pi\rangle$, $\langle\Sigma^+|Q_{\mp2}^{(2)}|\mp\Delta\rangle$, etc.) equal to zero and rearranging to obtain relations between different Cartesian components of the matrix elements. In the case of D_{2h} symmetry, the corresponding equations (3.3.7)-(3.3.12) are identical except for the addition of the relevant g/u parity label.

	A_1	A_2	B_1	B_2
A_1	s	xy	xz	yz
A_2	xy	s	yz	xz
B_1	xz	yz	s	xy
B_2	yz	xz	xy	s

Table 3.1: Product table for the quadratic functions that transform as the product of different irreducible representations for the C_{2v} point group.

	A_g	B_{1g}	B_{2g}	B_{3g}	A_u	B_{1u}	B_{2u}	B_{3u}
A_g	s	xy	xz	yz				
B_{1g}	xy	s	yz	xz				
B_{2g}	xz	yz	s	xy				
B_{3g}	yz	xz	xy	s				
A_u					s	xy	xz	yz
B_{1u}					xy	s	yz	xz
B_{2u}					xz	yz	s	xy
B_{3u}					yz	xz	xy	s

Table 3.2: Product table for the quadratic functions that transform as the product of different irreducible representations for the D_{2h} point group.

Symmetry	Components
A_g	Σ_g^+, $(\Delta_g)_{xx}$
B_{1g}	Σ_g^-, $(\Delta_g)_{xy}$
B_{2g}	$(\Pi_g)_x$
B_{3g}	$(\Pi_g)_y$
A_u	Σ_u^-, $(\Delta_u)_{xy}$
B_{1u}	Σ_u^+, $(\Delta_u)_{xx}$
B_{2u}	$(\Pi_u)_y$
B_{3u}	$(\Pi_u)_x$

Table 3.3: Irreducible representations for homonuclear symmetry groups, and corresponding components of electronic states.

Symmetry	Components
A_1	Σ^+, Δ_{xx}
A_2	Σ^-, Δ_{xy}
B_1	Π_x
B_2	Π_y

Table 3.4: Irreducible representations for heteronuclear symmetry groups, and corresponding components of electronic states.

Chapter 4

Quadrupole Line Lists for Heteronuclear Diatomics

4.1 Introduction

The heteronuclear molecules CO and HF were selected as case studies for an initial demonstration of the methodology outlined in the previous chapter. The rovibrational spectra of the $^1\Sigma$ ground states of these heteronuclear molecules exemplify systems with large molecular quadrupole moments in which the consideration of E2 transitions is necessary to obtain accurate cross-sections. In this chapter I provide a demonstration of the methodology for creating a spectroscopic model of a given molecular system in the Duo program. This includes performing novel *ab initio* calculations of electronic structure properties to obtain quadrupole moment curves, and performing electric quadrupole calculations using the new computational methodology implemented in the Duo program.

4.2 Carbon Monoxide

Carbon monoxide is a heteronuclear diatomic molecule, and thus electric dipole transitions are allowed within its ground $X\ ^1\Sigma^+$ state. However, it also possesses a strong electric quadrupole moment,[12] and as a result, the electric dipole infrared spectrum is accompanied by weaker electric quadrupole lines. We show that many of the E2 spectral lines at room temperature lie higher in intensity than the minimum spectroscopic cutoff of 10^{-30} cm/molecule at the HITRAN reference temperature of $T = 296$ K, typically applied to E1 spectra. As a result, their inclusion or emission in spectroscopic databases has significant implications for applications where accurate cross-sections are required.

Numerous experimental and *ab initio* studies have been performed of the electric dipole moment spectra for the CO molecule. Amonst this work are the recent accurate calculations by Li et al. [5], who seek to resolve a long-standing uncertainty in the line intensities of CO E1 spectra. Namely, significant differences observed between the intensities predicted by the calculations of Goorvitch [117] and those of Huré and Roueff [118]. The former uses Chackerian's [119] semi-empirical dipole moment function, obtained from a nonlinear least-squared fit to vibrational states up to $v = 38$. The latter uses a purely *ab initio* electric dipole moment curve (DMC), computed by Langhoff and Bauschlicher via ACPF calculations on a 5Z basis set [120] List et al. [71] perform new CRDS measurements in order to produce an accurate DMC via a direct-fit. At long bond lengths, where experimental data is not attainable, they reproduce the calculations of Langhoff and Bauschlicher [120] but with a finer grid, and determine that the interpolation used on the original grid was insufficient to capture the full shape of the DMC. Their PEC of choice is the analytical MLR3 function obtained by Coxon and Hajigeorgiou [121] via a direct fit to 21559 spectroscopic lines[121].

Studies of the quadrupole moment of CO are somewhat sparser. Although several experimental measurements exist for the equilibrium molecular quadrupole moment, only a single study presents a QMC across a range of geometries. The early work by Truhlar [4] presents simple Hartree-Fock calculations of the quadrupole moment at just 6 internuclear geometries. The accuracy of the vibrational matrix elements calculated is low, particularly for weaker transitions corresponding to higher vibrational quantum numbers. In particular the methodology struggles to accurately describe the quadrupole moment at intermediate and long internuclear distances, which are necessary for calculating the vibrational overtones. Coriani et al. [11] compares the results of CCSD and CC3 calculations on the CO molecule with a variety of basis sets. The results show that the CCSD level of theory is insufficient to correctly describe the electric properties of the CO molecule, and that consideration of triple excitations is vital. They also study the convergence of such calculations with increasing basis set size, and find the results converge quickly for bases larger than DZ.

In the present work, following the success of Coriani et al. [11], the CCSD(T) method is employed with an aug-cc-pwCVQZ basis as implemented in the CFOUR program [63] to calculate the strength of the non-zero quadrupole component Q_{zz} for 100 nuclear geometries in the range 1.50–3.78 a_0. Divergent behaviour at large internuclear separations is attributed to CCSD(T)'s inability to account for multireference effects. The curve is therefore truncated at 3.0 a_0. The QMC obtained from these calculations is shown in Fig. 4.1.

The value of the electric quadrupole moment curve at equilibrium separa-

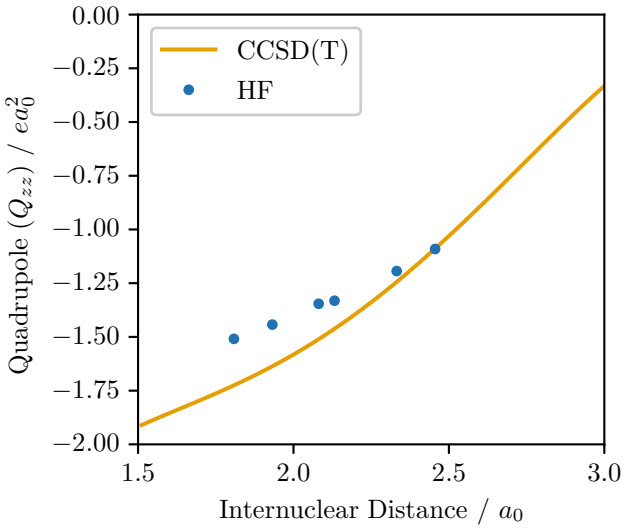

Figure 4.1: Electric quadrupole moments in a.u. (ea_0^2) for CO obtained in this work via CCSD(T) calculations compared to Hartree-Fock calculations by Truhlar [4].

tion $Q_{zz} = -1.45$ a.u. (a.u. $= ea_0^2$) agrees reasonably well with the Hartree-Fock calculations of Truhlar [4], which obtain $Q_{zz} = -1.33$ a.u.. Note that Truhlar [4] chooses a definition of the quadrupole moment which is a factor of two larger than the definition employed by MOLPRO and Duo, the value quoted here is adjusted accordingly. Importantly, we obtain very good agreement with experimental values of the ZPE-averaged quadrupole moment from the literature. From the CCSD(T) quadrupole moment shown in Fig. 4.1, Duo calculates $\langle v = 0|Q_{zz}|v = 0\rangle = -1.4522$ a.u. which agrees closely with the accurate MBERS measurement of Meerts et al. [122], the CC3 calculations of Coriani et al. [11], and EFGIB measurements from other sources. These comparisons are presented in Table 4.1.

Nuclear motion calculations are performed using the semi-empirical PEC of Meshkov et al. [125]. This accurate analytical representation of the PEC is chosen for the Duo solutions in order to improve the quality of the wavefunctions used to calculate the linestrengths. The Duo vibrational grid used for the calculation consists of 501 equally spaced points in the range 1.50–3.00 a_0, and the first 21 vibrational states are selected to form the contracted basis. These excitations correspond to energies within the spectroscopically relevant region ($E/hc < 40.000\,\mathrm{cm}^{-1}$) for the room temperature applications.

After solving the Schrödinger equation for rotational quantum numbers $0 \leq J \leq 50$, transitions with a vibrational transition quadrupole moment $\langle \xi_f v_f|Q_0^{(2)}|\xi_i v_i\rangle < 1 \times 10^{-5}$ a.u. are discarded. It was found by Medvedev et al.

Table 4.1: A comparison of various electric quadrupole moment values for CO in a.u. ($ea_0^2 = 4.486\,484(28) \times 10^{-40}\,\mathrm{C\,m^2}$ [10]) from the literature. All values are averaged over the vibrational ZPE and are given in the molecular centre of mass reference frame, $Q_{zz}^{(\mathrm{CM})} = 2R_z\mu + Q_{zz}^{(\mathrm{EQC})}$ with the displacement between the centre of mass and the electric quadrupole centre given by $R_z = -5.96\,\mathrm{a.u.}$ and a dipole moment $\mu = -0.043\,159\,\mathrm{a.u.}$ [11, 12]

Q_{zz} / a.u.	Method	Ref.
-1.4522	CCSD(T)	This work
-1.445(2)	CC3	[11]
-1.43(3)	MBERS	[122]
-1.440(69)	EFGIB	[12]
-1.382(31)	EFGIB	[123, 12]
-1.18(22)	EFGIB	[124, 12]

[126] that numerically computed transition dipole moments of high overtones corresponding to large changes in vibrational quanta can suffer from numerical instabilities and lead to unphysically large intensities. This results in the appearance of an intensity 'plateau' for vibrational bands arising from the high overtone transitions. This is noticeable in the case of $^{12}C^{16}O$ for the vibrational bands above $1000\,\mathrm{cm^{-1}}$. In the case of electric quadrupole transitions however, the intensity of these high overtone vibrational bands is sufficiently weak that absorption lines with transition quadrupole moments $\langle \xi_f v_f | Q_0^{(2)} | \xi_i v_i \rangle < 1 \times 10^{-5}\,\mathrm{a.u.}$ (corresponding to high overtone bands) can simply be excluded from the line list altogether.

The calculated state energies are substituted for those obtained by Li et al. [5] in a simultaneous direct-fit to experimentally determined energy levels. This improves the accuracy in the line positions of the final stick spectrum, obtained via ExoCross [127], but has no effect on the quadrupole Einstein coefficients or linestrengths. The energy level data of Li et al. [5] is made available through the HITRAN or ExoMol (exomol.com) databases[25].

The resultant room temperature ($T = 296$ K) line list for $^{12}C^{16}O$ with a cut-off intensity of $10^{-35}\,\mathrm{cm\,molecule^{-1}}$ consists of 6474 electric quadrupole transitions between rotational states up to $J_{\max} = 48$, and vibrational states $v = 7$. A synthetic room temperature E2 spectrum is illustrated in Fig. 4.2, where it is compared to the E1 spectrum of Li et al. [5]. The difference is approximately eight orders of magnitude. Nonetheless, many E2 lines - particularly for the $v = 0 \leftarrow 0$ and $v = 1 \leftarrow 0$ bands - lie above the typical cutoff intensity used in many spectroscopic databases ($\sim 10^{-30}\,\mathrm{cm^2\,molecule^{-1}}$

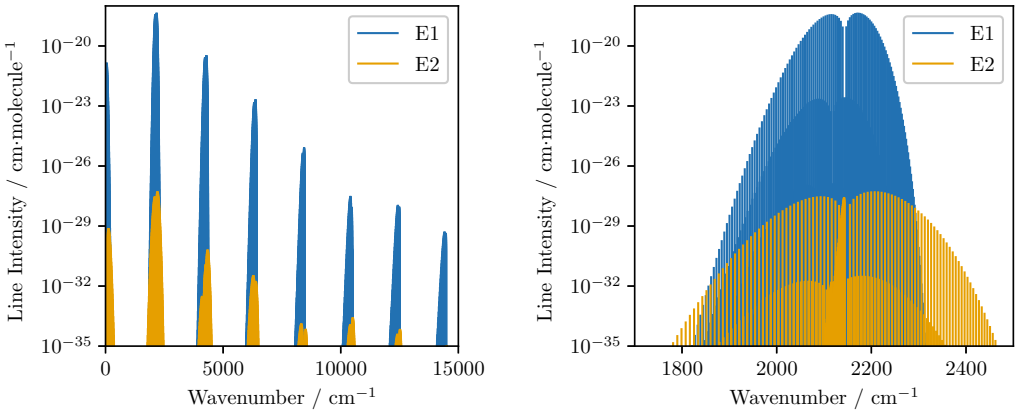

Figure 4.2: Vibrational bands (left) and rotational $v = 0 - 1$ transitions (right) of the E1 and E2 rovibrational spectra in the ground $X\ ^1\Sigma^+$ state of the $^{12}C^{16}O$ molecule. The E1 intensities are those of Li et al. [5], via the ExoMol database.

at $T = 296$ K).

The computed electric quadrupole Einstein A coefficients of $^{12}C^{16}O$ are combined with the ExoMol E1 line list Li2015 for CO in a form of an E2 Transition file, see an extract in Table 4.2. Apart from the Einstein A E2 coefficients (s^{-1}), the Transition file contains the upper and lower state counting numbers of the Li2015 State file, as illustrated in Table 4.3, which presents an extract from the ExoMol State file of the $^{12}C^{16}O$ line list Li2015. For more details on the ExoMol line list structure see Tennyson et al. [25].

4.3 Hydrogen Fluoride

Like the CO molecule, HF possesses a strong permanent electric dipole moment[129], it also possesses a strong permanent electric quadrupole moment[130]. Numerous *ab initio* studies have been performed for HF, including several which produce QMCs for the ground $X\ ^1\Sigma^+$ electronic state.[7, 6, 131] Piecuch et al. [7] use the orthogonally spin-adapted linear-response coupled-cluster (LRCC) theory with singly and doubly excited clusters (CCSD) and obtain quadrupole moments at 15 internuclear geometries in the range 1.126 32–12.1296 a_0 Their basis set of choice is that introduced by Sadlej for correlated calculations of molecular electric properties,[132] which they compare to standard basis sets at the TZ level. They also provide the results of full CI calculations on a DZ basis set. Maroulis [6] presents all-electron CCSD(T) calculations of the quadrupole moment at nine internuclear geometries in the range 0.9328–2.5328 a_0 For comparison, the quadrupole moment for the $X^1\Sigma^+$

f	i	A_{fi}	$\tilde{\nu}_{fi}$
94	10	1.0587E-17	10.591935
93	9	1.1546E-17	10.696876
92	8	1.2569E-17	10.801832
91	7	1.3657E-17	10.906802
90	6	1.4815E-17	11.011786
89	5	1.6043E-17	11.116781
88	4	1.7346E-17	11.221787
87	3	1.8725E-17	11.326802
86	2	2.0183E-17	11.431825
85	1	2.1722E-17	11.536856
136	52	1.7502E-16	17.652735

Table 4.2: Extract from the $^{12}C^{16}O$ electric quadrupole Transition file. It contains the upper (f) and lower (i) states counting numbers, Einstein A coefficients (s^{-1}) and transition wavenumbers (cm^{-1}).

Table 4.3: Extract from the Li2015 States file for $^{12}C^{16}O$.

i	E	g	J	v	τ
1	0.000000	1	0	0	e
2	2143.271100	1	0	1	e
3	4260.062200	1	0	2	e
4	6350.439100	1	0	3	e
5	8414.469300	1	0	4	e
6	10452.222200	1	0	5	e
7	12463.768600	1	0	6	e
8	14449.181300	1	0	7	e
9	16408.534600	1	0	8	e
10	18341.904400	1	0	9	e
11	20249.368200	1	0	10	e

i: State counting number.
$\tilde{E}$: State energy in cm^{-1}.
g_i: Total statistical weight, equal to $g_{\text{ns}}(2J+1)$.
J: Total angular momentum.
State: Electronic state.
v: State vibrational quantum number.
τ: Rotationless parity e/f [128].

state is computed via the MRCI method and an aug-cc-pVQZ basis set at 501 internuclear geometries in the range 1.32–6.99 a_0 using Molpro.

Table 4.4: A comparison of various *ab initio* electric quadrupole moment values for HF in a.u. (ea_0^2). All values are given in the molecular centre of mass reference frame, and at the equilibrium nuclear geometry.

Q_{zz} / a.u.	Method	Ref.
1.706	MRCI	This work
1.72	CCSD	[7]
1.72	CCSD(T)	[6]
1.66	CI	[7]

The electric quadrupole moments of HF obtained via these various methods are illustrated in Fig. 4.3. Although the four curves have the same general shape, significant variation is apparent between the value of Q_{zz} computed at intermediate bond lengths close to 3.8 a_0. Here the strength of the quadrupole moment is greatest, and difference of more than 0.5 a.u. is apparent between the full CI and CCSD methods. Table 4.4 shows the differences in the value of the quadrupole moment at the equilibrium internuclear distance for the four *ab initio* methods presented. All four calculations produce similar values for $Q_{zz}(R_e)$, but the coupled-cluster methods systematically overestimate the strength relative to experimental measurements. Importantly, when averaged over the vibrational ZPE, the MRCI results obtained in the present work give good agreement with the experimental MBERS measurement of de Leeuw and Dymanus [130]. They obtain $\langle v = 0|Q_{zz}(r)|v = 0\rangle = 1.75(2)$ a.u., whilst Duo calculates a value of 1.747 a.u., which is within the range of experimental uncertainty.

For the PEC, Coxon and Hajigeorgiou [8] provide a very accurate RKR-style analytical expression for the potential energy and Born-Oppenheimer breakdown functions of the $X^1\Sigma^+$ ground electronic state of various hydrogen halide isotopologues, including $^1H^{19}F$. They devise a novel analytical form (MLR3) of the diatomic electronic potential and perform a non-linear least squares fit to experimental energies.

Their analytical representation of the MLR3 potential has been newly implemented in Duo and for the present calculations, the HF MLR3 parameters obtained by Coxon and Hajigeorgiou [8] are employed, as well as their Born-Oppenheimer breakdown (BOB) function which is obtained from the Fortran source code provided in the supplementary material of Coxon and Hajigeorgiou [8].

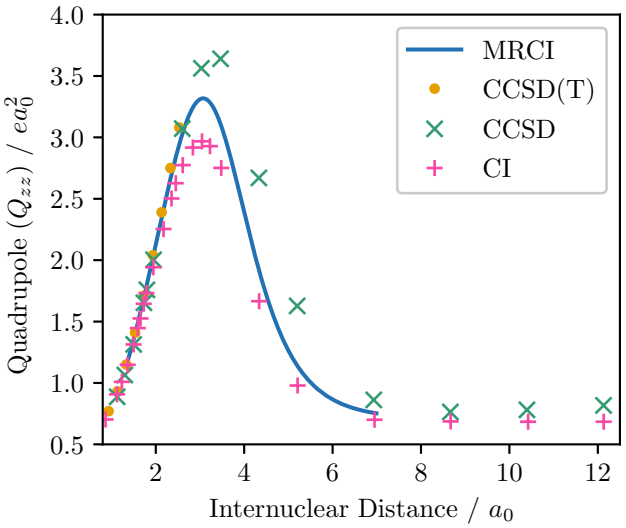

Figure 4.3: Comparison of the quadrupole moment curves in a.u. (ea_0^2) for HF obtained via various *ab initio* methods. The MRCI calculations presented in this work, CCSD(T) calculations of Maroulis [6], and CCSD and full-CI calculations of Piecuch et al. [7].

Fig. 4.4, shows a comparison of the potential energy curves obtained from our MRCI calculations, the CCSD calculations of Piecuch et al. [7] and the MLR3 potential of Coxon and Hajigeorgiou [8]. All three methods give similar results at short and intermediate bond lengths. The CCSD calculations overestimate the dissociation energy, relative to the empirical MLR3 potential, and the MRCI results predict a slightly lower dissociation energy. Fig. 4.5 illustrates the results of calculations from two spectroscopic models. In each case the potential energies are the same; the MLR3 and BOB curves of Coxon and Hajigeorgiou [8]; but one model uses the MRCI quadrupole moment presented in this work, and the other uses Piecuch's CCSD quadrupole moment. In both cases nuclear motion calculations are performed for rotational states $0 \leq J \leq 41$, the vibrational grid is defined for 501 equally spaced points in the range 0.76–4.40 a_0, and the first 20 vibrational states are chosen for the contracted basis.

For the first three vibrational bands, the absorption intensities predicted by both spectroscopic models are nearly identical. Higher order vibrational bands, however, exhibit significant discrepancies. The CCSD intensities begin to plateau above 20 000 cm^{-1}, we propose that this intensity plateau arises as a result of the same effect encountered in section 4.2 and detailed by Medvedev et al. [126]. Comparatively, the MRCI spectrum shows no such intensity plateau. This may be attributed in part to the fact that the MRCI

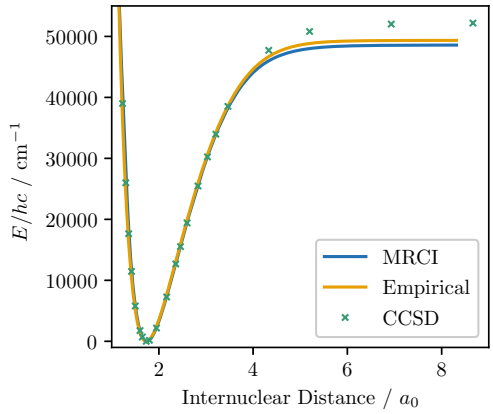

Figure 4.4: Comparison of the potential energy curves for the $X^1\Sigma^+$ ground state of HF. The MRCI calculations are from this work, empirically fitted MLR3 potential of Coxon and Hajigeorgiou [8], and the CCSD calculations of Piecuch et al. [7].

quadrupole moment is obtained on a considerably finer grid of internuclear distances, which more tightly constrains the interpolation performed by the Duo program. The gradient of CCSD quadrupole moment curve at distances $R > 3\,a_0$ is larger in magnitude than that of the MRCI calculations, which suggests that the CCSD calculations also over-estimate the intensity of transitions to high vibrational states, resulting in the apparent 'plateau'. This may be attributed to improved ability for MRCI calculations to account for electron correlation effects at long bond lengths. Fig. 4.6 shows the gradient of the two quadrupole moment functions computed using a central finite difference scheme on the Duo integration grid.

The MRCI spectrum exhibits a local minimum in intensity for the $v = 5 \leftarrow 0$ band. A similar abnormal intensity was observed by Medvedev et al. [126] for the same vibrational band of the electric dipole spectrum. Regardless, the expected E2 absorption intensities for the $v = 5 \leftarrow 0$ band is extremely weak, far weaker than typical spectroscopic cutoff intensity (10^{-30} cm/molecule at $T = 296$ K).

Intensities obtained using the MRCI quadrupole moment are chosen for the final ^{1}H^{19}F spectroscopic model and line list. This is combined with the ExoMol E1 line list Coxon-Hajig in the form of an E2 Transition file. Fig. 4.7 compares the E2 intensities obtained for room temperature calculations to the E1 intensities of Coxon and Hajigeorgiou [8]. It consists of 2716 electric quadrupole transitions between rotational states up to $J = 18$ and vibrational states up to $v = 9$ with a cutoff intensity of 10^{-35} cm molecule^{-1} ($T = 296$ K) and is available through the ExoMol database (www.exomol.com).

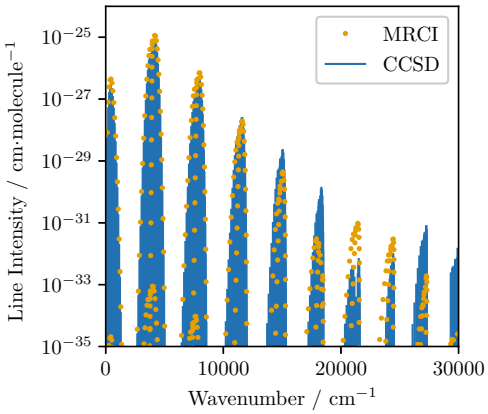

Figure 4.5: Comparison of the electric quadrupole absorption spectrum for $H^{19}F$ obtained via spectroscopic models using the CCSD and MRCI quadrupole moment curves illustrated in Fig. 4.3.

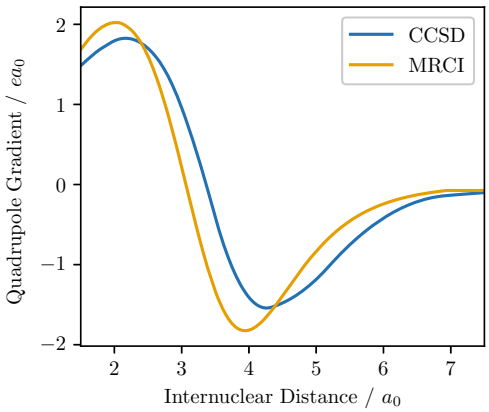

Figure 4.6: Central finite difference gradients of the HF quadrupole moment obtained via MRCI and CCSD methods with respect to internuclear distance.

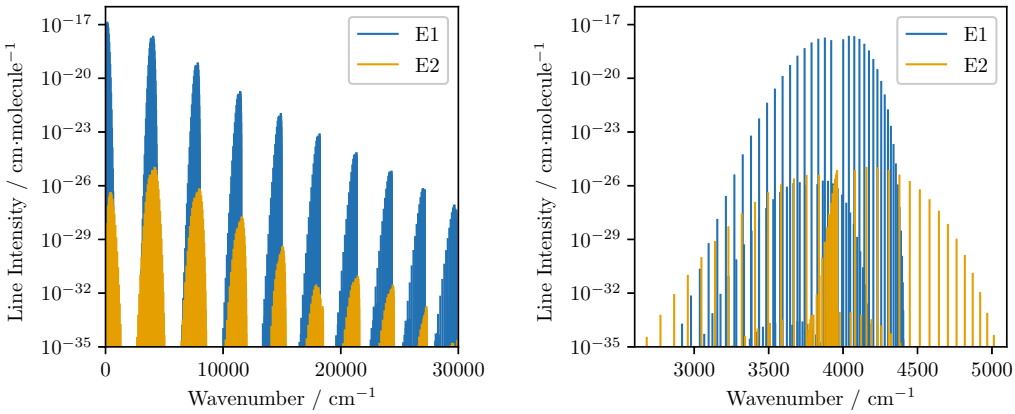

Figure 4.7: Vibrational bands (left) and rotational $v = 0 - 1$ transitions (right) of the E1 and E2 rovibrational spectra in the ground $X^1\Sigma^+$ state of the $H^{19}F$ molecule as line intensities (cm/-molecule). The E1 spectrum is that of Coxon and Hajigeorgiou [8], via the ExoMol database.

Chapter 5

Molecular Oxygen Line List

5.1 Introduction

In this chapter I will outline the electronic structure calculations that were performed in order to create a spectroscopic model of the $^{16}O_2$ molecule. I begin by outlining the structure of the electronic spectral bands of interest, namely those in the infrared region of the electromagnetic spectrum. This includes the electric quadrupole and magnetic dipole moments that generate the transitions, as well as the spin-orbit terms that couple electronic states and allow various electronic bands to 'borrow' intensity from other electronic bands. I will show how the numerous such couplings produce the complex spectral features, particularly those of the atmospheric A-, B, δ- and γ-bands, which arise from transitions between the ground $X\,^3\Sigma_g^-$ state and the excited $b\,^1\Sigma_g^+$ state.

Finally I will detail the electronic structure calculations that were performed in order to produce the seven potential energy curves and 27 coupling curves required to reproduce the three electronic bands of interest. I will also explain how these curves are post-processed following the electronic structure calculations in order to ensure a stable solution of the nuclear Schrödinger equation. This includes ensuring consistency between the phases of the various properties obtained across different nuclear geometries, as well as fitting analytic representations to ensure the functions are continuous and differentiable.

5.2 Oxygen Band Structure

The three lowest lying electronic states of molecular oxygen are the $X\,^3\Sigma_g^-$, $a\,^1\Delta_g$, and $b\,^1\Sigma_g^+$ states. All three states have *gerade* symmetry, and so transitions between them are forbidden in the electric dipole approximation.

The structure of the infrared bands has been expounded in detail throughout the literature [133–137]. In particular, we highlight the work of Minaev et al. [137], who provide a comprehensive account of contributions to the atmospheric $b\,^1\Sigma_g^+ - X\,^3\Sigma_g^-$ $a\,^1\Delta_g - X\,^3\Sigma_g^-$, and Noxon $b\,^1\Sigma_g^+ - a\,^1\Delta_g$ bands. The electric quadrupole transitions are, in general, weaker than magnetic dipole transitions, but nonetheless have been observed in both the laboratory [138–140] and in atmospheric solar spectra [58, 56]. They are present in both the $b\,^1\Sigma_g^+ - X\,^3\Sigma_g^-$, and $a\,^1\Delta_g - X\,^3\Sigma_g^-$ bands. Crucial to an account of the infrared bands are a set of highly excited Π states, namely the $1^1\Pi_g$, $2^1\Pi_g$, $1^3\Pi_g$, and $2^3\Pi_g$ states[141, 136]. The two pairs of states with the same spin multiplicity each exhibit avoided crossings, with the $2^3\Pi_g$ and $2^1\Pi_g$ states being pre-dissociative in nature. In order to treat this collection of Π states we transform to the diabatic representation [97] to produce the $II\,^1\Pi_g$, $I\,^1\Pi_g$, $II\,^3\Pi_g$, and $I\,^3\Pi_g$ states. The $II\,^1\Pi_g$ and $II\,^3\Pi_g$ states exhibit shallow potential wells with minima approximately $60\,000\,\mathrm{cm}^{-1}$ above the zero-point energy, which give rise to a small number of bound vibrational levels.

In order to elucidate the spectroscopic model required to produce the complete set of absorption intensities for $^{16}O_2$ it is worth explicitly stating the numerous electric quadrupole moments and magnetic dipole moments that contribute to this absorption. In this section I will illustrate how the various spin-orbit couplings between the seven electronic states ($X\,^3\Sigma_g^-$, $a\,^1\Delta_g$, $b\,^1\Sigma_g^+$, $I\,^1\Pi_g$, $II\,^1\Pi_g$, $I\,^3\Pi_g$, and $II\,^3\Pi_g$) allow the different electronic bands to 'borrow' intensity from one another to produce the complex band structure observed in the infrared spectrum of $^{16}O_2$. I will provide expressions for the perturbed matrix elements, which appear in the linestrength expressions (2.4.26) and (2.4.30), in terms of the unperturbed eigenfunctions and the spin-orbit coupling terms that mix them. In each case I consider contributions up to first order in the spin-orbit perturbation, and neglect any contributions that appear as a product of two or more spin-orbit couplings. Thus this does not represent a complete description of the atmospheric and infrared system, but merely provides an illustration of the major contributions.

5.2.1 Electric Quadrupole Transitions

The rovibrational electric quadrupole transitions within the $X\,^3\Sigma_g^-$ ground state are the simplest to attribute, since they arise as a result of the diagonal quadrupole moment of the ground electronic state. The $b\,^1\Sigma_g^+ - X\,^3\Sigma_g^-$ electric quadrupole intensities are comprised of two quadrupole moments corresponding to components of the irreducible quadrupole moment operator. The first is the $Q_0^{(2)}$ moment, which arises as a result of spin-orbit mixing between the $X\,^3\Sigma_g^-$ and $b\,^1\Sigma_g^+$ states, and generates two diagonal contributions to the total intensity for $\Delta\Omega = 0$ transitions. The second is the $Q_{\pm1}^{(2)}$ component, which

generates $\Delta\Omega = \pm 1$ transitions via spin-orbit coupling of the $\mathrm{X}\,^3\Sigma_g^-$ state and the excited $^1\Pi_g$ states. Here $\Omega = \Lambda + \Sigma$ is the projection of the total electronic angular momentum on the molecular axis, with Λ and Σ the orbital and spin angular momenta respectively. The $^1\Pi_g$ states lies far in energy above the $\mathrm{X}\,^3\Sigma_g^-$, and the thus primary contribution to the $\mathrm{b}\,^1\Sigma_g^+ - \mathrm{X}\,^3\Sigma_g^-$ band comes from the difference in permanent electric quadrupole moments of the two Σ states. Denoting the first-order SOC-perturbed expressions with a subscript p, we write

$$\left\langle \mathrm{b}^1\Sigma_g^+ \middle| Q_0^{(2)} \middle| \mathrm{X}^3\Sigma_{g,0}^- \right\rangle_p = \frac{\left\langle \mathrm{b}^1\Sigma_g^+ \middle| H_{\mathrm{SO}} \middle| \mathrm{X}^3\Sigma_{g,0}^- \right\rangle}{E(\mathrm{X}^3\Sigma_{g,0}^-) - E(\mathrm{b}^1\Sigma_g^+)} \left\langle \mathrm{b}^1\Sigma_g^+ \middle| Q_0^{(2)} \middle| \mathrm{b}^1\Sigma_g^+ \right\rangle + \frac{\left\langle \mathrm{X}^3\Sigma_{g,0}^- \middle| H_{\mathrm{SO}} \middle| \mathrm{b}^1\Sigma_g^+ \right\rangle^*}{E(\mathrm{b}^1\Sigma_g^+) - E(\mathrm{X}^3\Sigma_{g,0}^-)} \left\langle \mathrm{X}^3\Sigma_{g,0}^- \middle| Q_0^{(2)} \middle| \mathrm{X}^3\Sigma_{g,0}^- \right\rangle \tag{5.2.1}$$

$$= \alpha_0 \left\langle \mathrm{b}^1\Sigma_g^+ \middle| Q_0^{(2)} \middle| \mathrm{b}^1\Sigma_g^+ \right\rangle - \alpha_0 \left\langle \mathrm{X}^3\Sigma_{g,0}^- \middle| Q_0^{(2)} \middle| \mathrm{X}^3\Sigma_{g,0}^- \right\rangle \tag{5.2.2}$$

$$\left\langle \mathrm{b}^1\Sigma_g \middle| Q_{\pm 1}^{(2)} \middle| \mathrm{X}^3\Sigma_{g,1}^- \right\rangle_p = \sum_\zeta \frac{\left\langle \zeta^1\Pi_g \middle| H_{\mathrm{SO}} \middle| \mathrm{X}^3\Sigma_{g,\pm 1}^- \right\rangle}{E(\mathrm{X}^3\Sigma_{g,1}^-) - E(\zeta^1\Pi_g)} \left\langle \mathrm{b}^1\Sigma_g^+ \middle| Q_{\pm 1}^{(2)} \middle| \zeta^1\Pi_g \right\rangle \tag{5.2.3}$$

$$= \sum_\zeta \alpha_{\zeta,\mathrm{X}} \left\langle \mathrm{b}^1\Sigma_g^+ \middle| Q_{\pm 1}^{(2)} \middle| \zeta^1\Pi_g \right\rangle \tag{5.2.4}$$

where H_{SO} is the Breit-Pauli spin-orbit Hamiltonian [142–144] and the electronic wave functions are expressed in the Hund's case (a) basis.

We now turn to the $\mathrm{a}\,^1\Delta_g - \mathrm{X}\,^3\Sigma_g^-$ band, which arises primarily as the result of a $Q_{\pm 2}^{(2)}$ quadrupole component, and borrows strength from the Noxon band ($\mathrm{b}\,^1\Sigma_g^+ - \mathrm{a}\,^1\Delta_g$) via spin-orbit mixing of the $\mathrm{X}\,^3\Sigma_g^-$ with the $\mathrm{b}\,^1\Sigma_g^+$ state. There is an additional contribution to this transition from $^3\Pi_g - \mathrm{X}\,^3\Sigma_g^-$ moments due to spin-orbit mixing of the $\mathrm{a}\,^1\Delta_g$ state and the $^3\Pi_g$ states. This $^3\Pi_g - \mathrm{X}\,^3\Sigma_g^-$ magnetic moment also contributes to a second (weaker) component of the $\mathrm{a}\,^1\Delta_g - \mathrm{X}\,^3\Sigma_g^-$ intensities, via the $Q_{\pm 1}^{(2)}$ quadrupole component, together with the $\mathrm{a}\,^1\Delta_g - {}^1\Pi_g$ moment due to spin-orbit mixing between the $\mathrm{X}\,^3\Sigma_g^-$ and $^1\Pi_g$ states.

$$\left\langle \mathrm{a}^1\Delta_g \middle| Q^{(2)}_{\pm 2} \middle| \mathrm{X}^3\Sigma^-_{g,0} \right\rangle_p = \frac{\left\langle \mathrm{b}^1\Sigma^+_g \middle| H_{\mathrm{SO}} \middle| \mathrm{X}^3\Sigma^-_{g,0} \right\rangle}{E(\mathrm{X}^3\Sigma^-_{g,0}) - E(\mathrm{b}^1\Sigma^+_g)} \left\langle \mathrm{a}^1\Delta_g \middle| Q^{(2)}_{\pm 2} \middle| \mathrm{b}^1\Sigma^+_g \right\rangle + \sum_{\xi} \frac{\langle \xi^3\Pi_{g,2} | H_{\mathrm{SO}} | \mathrm{a}^1\Delta_g \rangle^*}{E(\mathrm{a}^1\Delta_g) - E(\xi^3\Pi_{g,2})} \left\langle \xi^3\Pi_{g,2} \middle| Q^{(2)}_{\pm 2} \middle| \mathrm{X}^3\Sigma^-_{g,0} \right\rangle \tag{5.2.5}$$

$$= \alpha_{\mathrm{b,X}} \left\langle \mathrm{a}^1\Delta_{g,2} \middle| Q^{(2)}_{\pm 2} \middle| \mathrm{b}^1\Sigma^+_{g,0} \right\rangle + \sum_{\xi} \alpha^*_{\xi,\mathrm{a}} \left\langle \xi^3\Pi_{g,2} \middle| Q^{(2)}_{\pm 2} \middle| \mathrm{X}^3\Sigma^-_{g,0} \right\rangle \tag{5.2.6}$$

$$\left\langle \mathrm{a}^1\Delta_g \middle| Q^{(2)}_{\pm 1} \middle| \mathrm{X}^3\Sigma^-_{g,1} \right\rangle_p = \sum_{\zeta} \frac{\left\langle \zeta^1\Pi_g \middle| H_{\mathrm{SO}} \middle| \mathrm{X}^3\Sigma^-_{g,1} \right\rangle}{E(\mathrm{X}^3\Sigma^-_{g,1}) - E(\zeta^1\Pi_g)} \left\langle \mathrm{a}^1\Delta_g \middle| Q^{(2)}_{\pm 1} \middle| \zeta^1\Pi_g \right\rangle + \sum_{\xi} \frac{\langle \xi^3\Pi_{g,2} | H_{\mathrm{SO}} | \mathrm{a}^1\Delta_g \rangle^*}{E(\mathrm{a}^1\Delta_g) - E(\xi^3\Pi_{g,2})} \left\langle \xi^3\Pi_{g,2} \middle| Q^{(2)}_{\pm 1} \middle| \mathrm{X}^3\Sigma^-_{g,1} \right\rangle \tag{5.2.7}$$

$$= \sum_{\zeta} \alpha_{\zeta,\mathrm{X}} \left\langle \mathrm{a}^1\Delta_g \middle| Q^{(2)}_{\pm 1} \middle| \zeta^1\Pi_g \right\rangle + \sum_{\xi} \alpha^*_{\xi,\mathrm{a}} \left\langle \xi^3\Pi_{g,2} \middle| Q^{(2)}_{\pm 1} \middle| \mathrm{X}^3\Sigma^-_{g,1} \right\rangle \tag{5.2.8}$$

The dominant contribution to the $\mathrm{a}\,^1\Delta_g - \mathrm{X}\,^3\Sigma^-_g$ intensities comes from the Noxon band, due to the fact that the $\mathrm{b}\,^1\Sigma^+_g$ state and $\mathrm{a}\,^1\Delta_g$ state are closely separated in energy, and the transition quadrupole moment between them is reasonably strong. This hypothesis is supported by the work of Mishra et al. [136], in which the ratio $Q^{(2)}_{\pm 1}/Q^{(2)}_{\pm 2}$ is calculated for various lines with a value in the range 0.012–0.055.

5.2.2 Magnetic Dipole Transitions

The strongest of the $^{16}O_2$ atmospheric transitions are the magnetic dipole transitions in the $\mathrm{b}\,^1\Sigma^+_g - \mathrm{X}\,^3\Sigma^-_g$ band. Magnetic dipole transitions are composed of both spin and orbital angular moments. However the relative strengths of the spin-orbit couplings imply that the primary contribution arises as a result of intensity borrowing from the spin-flip transitions between the $\Sigma = 0$ and $\Sigma = \pm 1$ sub-levels of the $\mathrm{X}\,^3\Sigma^-_g$ state through spin-orbit coupling between the $\mathrm{b}\,^1\Sigma^+_g$ and $\mathrm{X}\,^3\Sigma^-_g$ states. Electronic orbital magnetic moments contribute only weakly to this branch through spin-orbit mixing of the $\mathrm{X}\,^3\Sigma^-_g$ and $^1\Pi_g$ states, and of the $\mathrm{b}\,^1\Sigma^+_g$ and $^3\Pi_g$ states.

$$\begin{aligned}\left\langle \mathrm{b}^1\Sigma_g^+\middle|d_{\pm1}\middle|\mathrm{X}^3\Sigma_{g,1}^-\right\rangle_p &= \frac{\left\langle \mathrm{X}^3\Sigma_{g,0}^-\middle|H_{\mathrm{SO}}\middle|\mathrm{b}^1\Sigma_g^+\right\rangle^*}{E(\mathrm{b}^1\Sigma_g^+)-E(\mathrm{X}^3\Sigma_{g,0}^-)}\left\langle \mathrm{X}^3\Sigma_{g,0}^-\middle|\hat{S}_{\pm1}\middle|\mathrm{X}^3\Sigma_{g,1}^-\right\rangle \\ &\quad+\sum_\zeta \frac{\left\langle \zeta^1\Pi_g\middle|H_{\mathrm{SO}}\middle|\mathrm{X}^3\Sigma_{g,1}^-\right\rangle}{E(\mathrm{X}^3\Sigma_{g,1}^-)-E(\zeta^1\Pi_g)}\left\langle \mathrm{b}^1\Sigma_g^+\middle|\hat{L}_{\pm1}\middle|\zeta^1\Pi_g\right\rangle \\ &\quad+\sum_\xi \frac{\left\langle \xi^3\Pi_{g,0}\middle|H_{\mathrm{SO}}\middle|\mathrm{b}^1\Sigma_g^+\right\rangle^*}{E(\mathrm{b}^1\Sigma_g^+)-E(\xi^3\Pi_{g,0})}\left\langle \xi^3\Pi_{g,0}\middle|\hat{L}_{\pm1}\middle|\mathrm{X}^3\Sigma_{g,1}^-\right\rangle \end{aligned} \tag{5.2.9}$$

$$\begin{aligned}&= -\alpha_{\mathrm{X,b}}\left\langle \mathrm{X}^3\Sigma_{g,0}^-\middle|\hat{S}_{\pm1}\middle|\mathrm{X}^3\Sigma_{g,1}^-\right\rangle+\sum_\zeta \alpha_{\zeta,\mathrm{X}}\left\langle \mathrm{b}^1\Sigma_g^+\middle|\hat{L}_{\pm1}\middle|\zeta^1\Pi_g\right\rangle \\ &\quad+\sum_\xi \alpha^*_{\xi,\mathrm{b}}\left\langle \xi^3\Pi_{g,1}\middle|\hat{L}_{\pm1}\middle|\mathrm{X}^3\Sigma_{g,1}^-\right\rangle \end{aligned} \tag{5.2.10}$$

Magnetic dipole transitions in the $\mathrm{a}\,^1\Delta_g$ – $\mathrm{X}\,^3\Sigma_g^-$ band are considerably weaker, and enabled only through spin-orbit coupling of the $\mathrm{a}\,^1\Delta_g$ and $\mathrm{X}\,^3\Sigma_g^-$ states with the $^3\Pi_g$ and $^1\Pi_g$ states, respectively.

$$\begin{aligned}\left\langle \mathrm{a}^1\Delta_g\middle|d_{\pm1}\middle|\mathrm{X}^3\Sigma_{g,1}^-\right\rangle_p &= \sum_\xi \frac{\langle \xi^3\Pi_{g,2}|H_{\mathrm{SO}}|\mathrm{a}^1\Delta_g\rangle^*}{E(\mathrm{a}^1\Delta_g)-E(\xi^3\Pi_{g,2})}\left\langle \xi^3\Pi_{g,2}\middle|\hat{L}_{\pm1}\middle|\mathrm{X}^3\Sigma_{g,1}^-\right\rangle \\ &\quad+\sum_\zeta \frac{\left\langle \zeta^1\Pi_g\middle|H_{\mathrm{SO}}\middle|\mathrm{X}^3\Sigma_{g,1}^-\right\rangle}{E(\mathrm{X}^3\Sigma_{g,1}^-)-E(\zeta^1\Pi_g)}\left\langle \mathrm{a}^1\Delta_g\middle|\hat{L}_{\pm1}\middle|\zeta^1\Pi_g\right\rangle \end{aligned} \tag{5.2.11}$$

$$= \sum_\xi \alpha^*_{\xi,a}\left\langle \xi^3\Pi_{g,2}\middle|\hat{L}_{\pm1}\middle|\mathrm{X}^3\Sigma_{g,1}^-\right\rangle+\sum_\zeta \alpha_{\zeta,X}\left\langle a^1\Delta_g\middle|\hat{L}_{\pm1}\middle|\zeta^1\Pi_g\right\rangle \tag{5.2.12}$$

Finally, the $\mathrm{X}\,^3\Sigma_g^-$ – $\mathrm{X}\,^3\Sigma_g^-$, composed of rotation-vibration and pure rotational transitions arises as a result of two magnetic dipole moments. The first couples spin sublevels in the $\mathrm{X}\,^3\Sigma_g^-$ state, and the second is composed of the diagonal spin magnetic moment.

$$\left\langle \mathrm{X}^3\Sigma_{g,1}^-\middle|d_{\pm1}\middle|\mathrm{X}^3\Sigma_{g,0}^-\right\rangle_p = \left\langle \mathrm{X}^3\Sigma_{g,1}^-\middle|S_{\pm1}\middle|\mathrm{X}^3\Sigma_{g,0}^-\right\rangle \tag{5.2.13}$$

$$\left\langle \mathrm{X}^3\Sigma_{g,\Omega}^-\middle|d_0\middle|\mathrm{X}^3\Sigma_{g,\Omega}^-\right\rangle_p = \left\langle \mathrm{X}^3\Sigma_{g,\Omega}^-\middle|\hat{S}_z\middle|\mathrm{X}^3\Sigma_{g,\Omega}^-\right\rangle \tag{5.2.14}$$

5.3 Electronic Structure Calculations

5.3.1 Previous Work

A considerable amount of effort has been devoted to establishing highly accurate potential energy curves for a range of electronic states of $^{16}O_2$. In this section we will briefly outline some of the most accurate state-of-the-art calculations conducted for relevant states before detailing the electronic structure calculations conducted in the present work.

In 2010 Bytautas et al. [145] employed Dunning's correlation-consistent triple and quadruple-zeta basis sets to determine the full configuration interaction energy for the three lowest-lying electronic states; $X\,^3\Sigma_g^-$, $a\,^1\Delta_g$, and $b\,^1\Sigma_g^+$, including core-valence correlations and relativistic contributions. Using a method developed in earlier work, which they term *correlation energy extrapolation by intrinsic scaling*, they extrapolate these energies to the complete basis set limit [145, 146]. In 2014 Liu et al. [13] produced accurate PECs for 22 electronic states as well 54 spin-orbit coupling curves via the complete active space self-consistent field (CASSCF) method, and a subsequent internally contracted multireference configuration interaction calculation including the Davidson correction (icMRCIQ).

By comparison there are few *ab initio* calculations of the electric quadrupole moment functions. The earliest calculations of the E2 moment for $^{16}O_2$ were made by Kotani et al. [147] in 1957, followed by Sarangi and Varanasi [148] in 1974. In recent years accurate multipole moment calculations at room temperature were made by Bartolomei et al. [149], and Couling and Ntombela [150]. In each case however, the quadrupole moment is given for only a single geometry. As far as the author is aware, the only calculation of a complete quadrupole moment curve across a range of internuclear geometries was performed in 1997 by Lawson and Harrison [151]. They use the aug-cc-pVQZ basis and MRCI method to obtain the permanent E2 moment of the $X\,^3\Sigma_g^-$ state in the range 2–12 a_0. The need for further calculations of electric quadrupole moments in order to obtain a spectroscopic model of the $^{16}O_2$ infrared bands is evident, particularly transition moments and the diagonal moments for excited states

A challenge arises in evaluating the accuracy of *ab initio* quadrupole moment curves due to a dearth of experimental data. Typically such measurements consist of only a single value, usually vibrationally averaged over the $v = 0$ ground state. In 1968 Buckingham et al. [124] obtained a value $Q_0^{(2)} = -0.3 \pm 0.1\ e\,{a_0}^2$ via pressure induced birefringence. Cohen and Birnbaum [152], and Birnbaum and Cohen [153] obtain $|Q_0^{(2)}| = 0.25\ e\,{a_0}^2$ via far-infrared spectra, which is in agreement with the measurement of $|Q_0^{(2)}| = 0.22\ e\,{a_0}^2$ made by Evans [154]. More recently Couling and Ntombela [150] ac-

curately measured the quadrupole moment via electric-field-gradient-induced birefringence (EFGIB) to be $Q_0^{(2)} = -0.230 \pm 0.006\ e\,{a_0}^2$. The effective transition quadrupole moments responsible for the $\mathrm{b}\,^1\Sigma_g^+ - \mathrm{X}\,^3\Sigma_g^-$ band were calculated empirically by Long et al. [140].

5.3.2 Infrared Bands

The necessary set of electric quadrupole moment curves (EQMCs), spin-orbit coupling curves (SOCs), orbital electronic angular momentum curves (EAMCs), and potential energy curves (PECs), are obtained with electronic structure calculations using the Molpro program. Preliminary calculations using the MRCI program for varying basis sets sizes were used to assess the convergence. Whilst the energies obtained with smaller basis sets differed significantly, comparison of the calculations using aug-cc-pV5Z and aug-cc-pV6Z basis sets with and without the Davidson correction showed close agreement, suggesting that the uncorrected aug-cc-pV5Z energies closely approximate the full configuration interaction energy.

To obtain the complete set of potential energy and coupling curves MCSCF calculations were performed with CAS(12,12) and a diffusion augmented, correlation-consistent, polarized quintuple-zeta basis set (aug-cc-pV5Z). The optimized orbitals from this MCSCF calculation were then used as the reference orbitals for a subsequent MRCI calculation in the same active space.

Symmetry	$(2S+1)$	No. States	State(s)
A_g	1	2	$\mathrm{b}\,^1\Sigma_g^+$, $\mathrm{a}\,^1\Delta_g(xx)$
B_{1g}	3	1	$\mathrm{X}\,^3\Sigma_g^-$
B_{1g}	1	1	$\mathrm{a}\,^1\Delta_g(xy)$
B_{2g}	1	2	$\mathrm{I}\,^1\Pi_g(x)$, $\mathrm{II}\,^1\Pi_g(x)$
B_{3g}	1	2	$\mathrm{I}\,^1\Pi_g(y)$, $\mathrm{II}\,^1\Pi_g(y)$
B_{2g}	3	2	$\mathrm{I}\,^3\Pi_g(x)$, $\mathrm{II}\,^3\Pi_g(x)$
B_{3g}	3	2	$\mathrm{I}\,^3\Pi_g(y)$, $\mathrm{II}\,^3\Pi_g(y)$

Table 5.1: This table details the number of states calculated for a given combination of irreducible symmetry group and spin multiplicity. It also shows the label of the corresponding states obtained from each calculation.

The MRCI calculations include a variety of symmetry groups and spin multiplicities in order to obtain a complete set of wavefunctions and potential energy curves for the required electronic states, and are detailed in Tab. 5.1. Calculations are made for a number of geometries in the range 0.090–0.300 nm for the $\mathrm{X}\,^3\Sigma_g^-$, $\mathrm{a}\,^1\Delta_g$ and $\mathrm{b}\,^1\Sigma_g^+$ states, and in the range 0.094–0.300 nm for the $1^1\Pi_g$, $2^1\Pi_g$ $1^3\Pi_g$, and $2^3\Pi_g$ states.

The wavefunctions obtained are used in subsequent MRCI calculations of the seven spin-orbit couplings, nine quadrupole moments, and the six orbital angular momentum curves required to reproduce the matrix elements in Eqs. (5.2.1) - (5.2.10). In addition to the quadrupole moments present in Eqs. (5.2.1) - (5.2.8), the diagonal quadrupole moments of the a $^1\Delta_g$, and the four Π states are also obtained.

The calculation at each geometry is performed independently, and for this reason we find that the CI program fails to converge at certain geometries. Additionally, some coupling curves exhibit phase differences with respect to neighbouring geometries due a phase ambiguity in the internal representation of the wavefunction. These phase flips are resolved by post processing the electronic structure properties to preserve the relative phases between different quantities. Additionally, for calculations involving multiple states in the same irreducible representation, the state that is assigned to a given quantity can vary between geometries. For example, a quadrupole moment at neighbouring geometries may alternately be assigned to either the I $^1\Pi_g$or the II $^1\Pi_g$. Similarly, this 'label switching' behaviour can also be corrected by post-processing the potential energy and coupling curves. Finally, curves involving the Π states are transformed to the diabatic representation using the numerical procedure described in Sec. 3.2.3. These diabatic *ab initio* curves are represented by the dots in Figs. 5.1 - 5.5.

5.4 Analytic Representation

After transforming to the diabatic representation, we obtain a set of bound potential energy curves and corresponding diabatic coupling curves. In order to fill in gaps in the *ab initio* data where the MOLPRO calculations fail to converge, and also to eliminate discontinuities that are characteristic of *ab initio* calculations across multiple geometries, we subsequently fit analytic functions for each of the curves described in Sec. 5.3. This also allows one to obtain spectroscopic parameters for the potential energy curves, and other characteristic quantities. The fitted parameters for this analytic representation of the *ab initio* data can also be used as a starting point for empirical refinement to experimental state energies.

5.4.1 Potential Energy Curves

To begin we fit the Morse/long-range (MLR) potential energy function to the five bound states under consideration. The Morse/long-range function was introduced by Le Roy et al. [155] and later refined by Le Roy et al. [156], and improves on the well-known Morse potential by accounting for the long-range

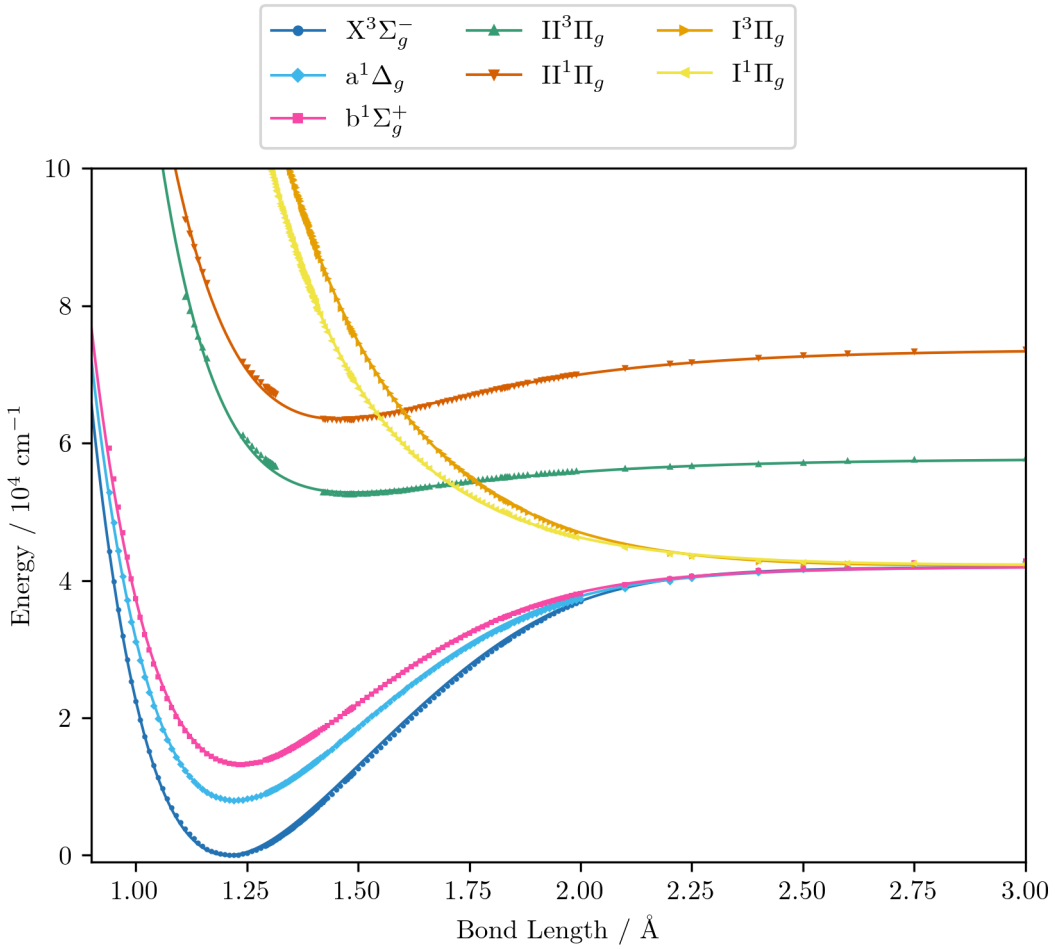

Figure 5.1: The PECs obtained from *ab initio* electronic structure calculations (dots) along with the continuous curves (solid lines) obtained by fitting the analytic potential energy functions to these *ab initio* data.

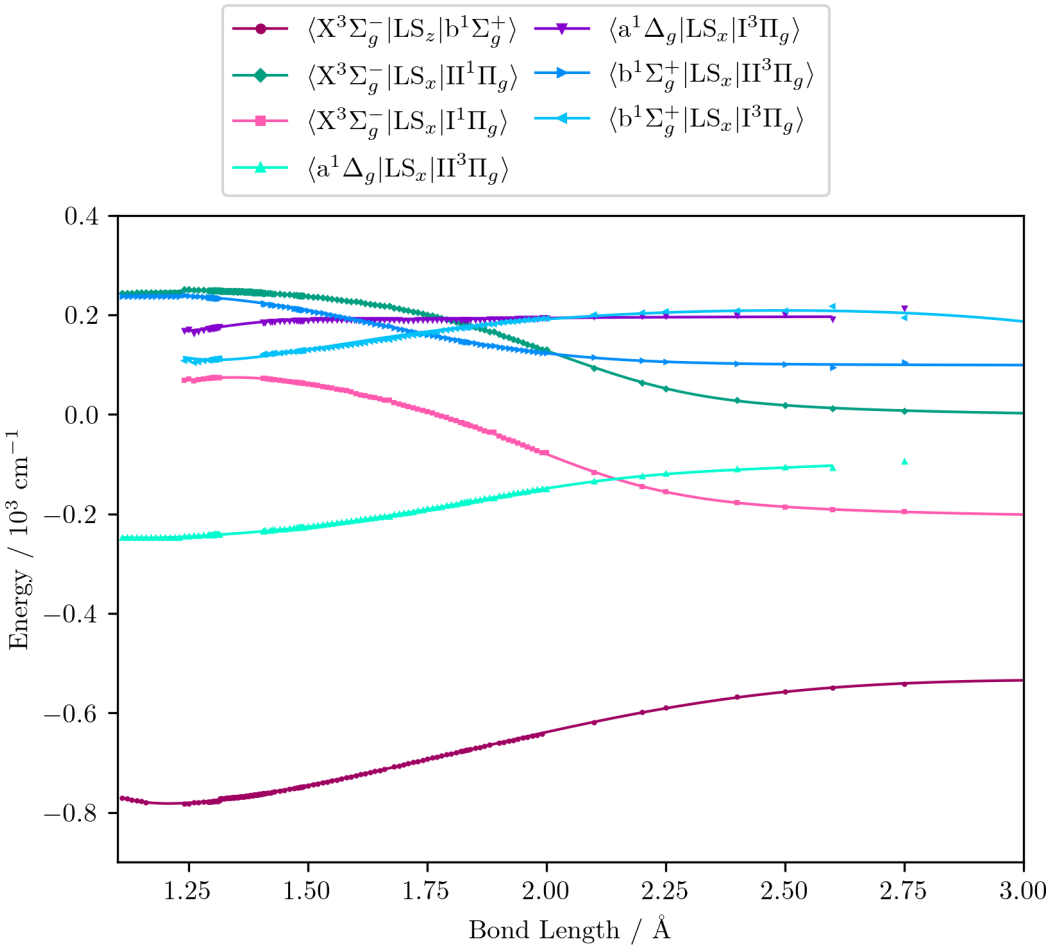

Figure 5.2: The SOCs obtained from *ab initio* electronic structure calculations (dots) along with the continuous curves (solid lines) obtained by fitting the analytic coupling functions to these *ab initio* data.

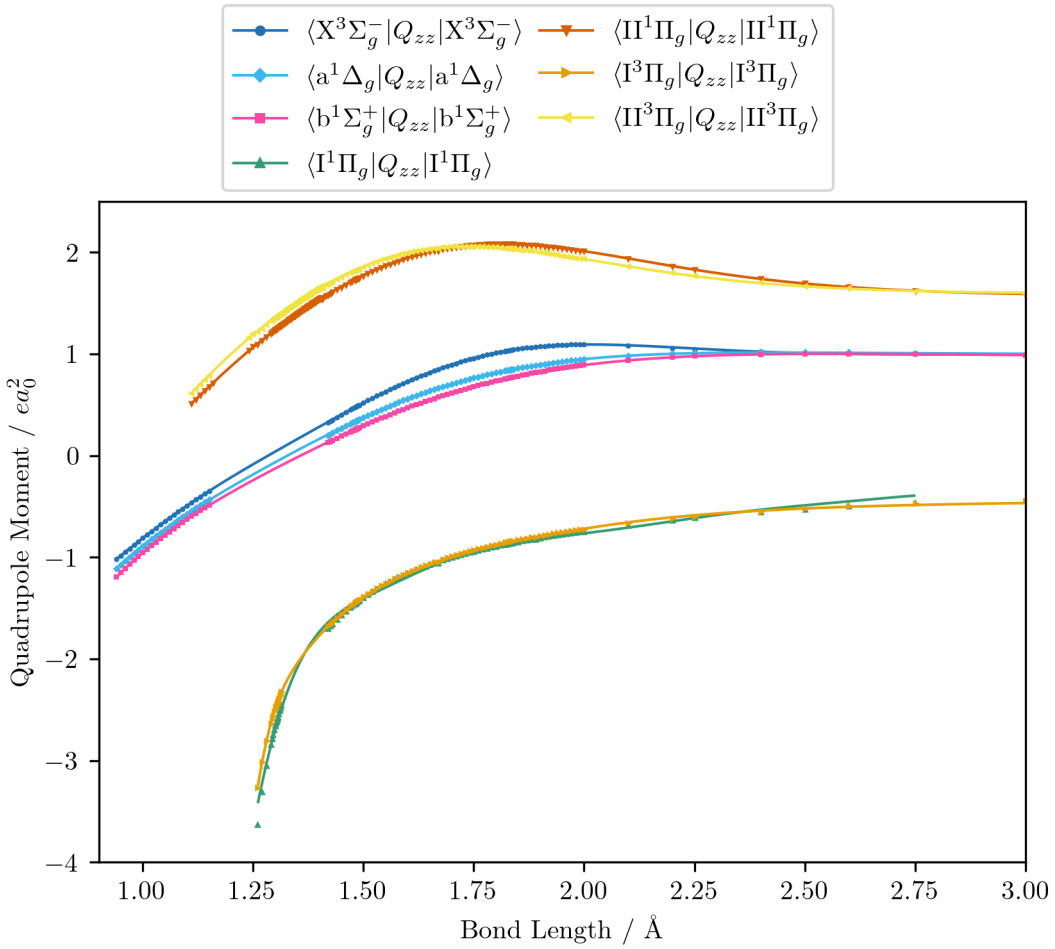

Figure 5.3: The diagonal EQCs obtained from *ab initio* electronic structure calculations (dots) along with the continuous curves (solid lines) obtained by fitting the analytic coupling functions to these *ab initio* data.

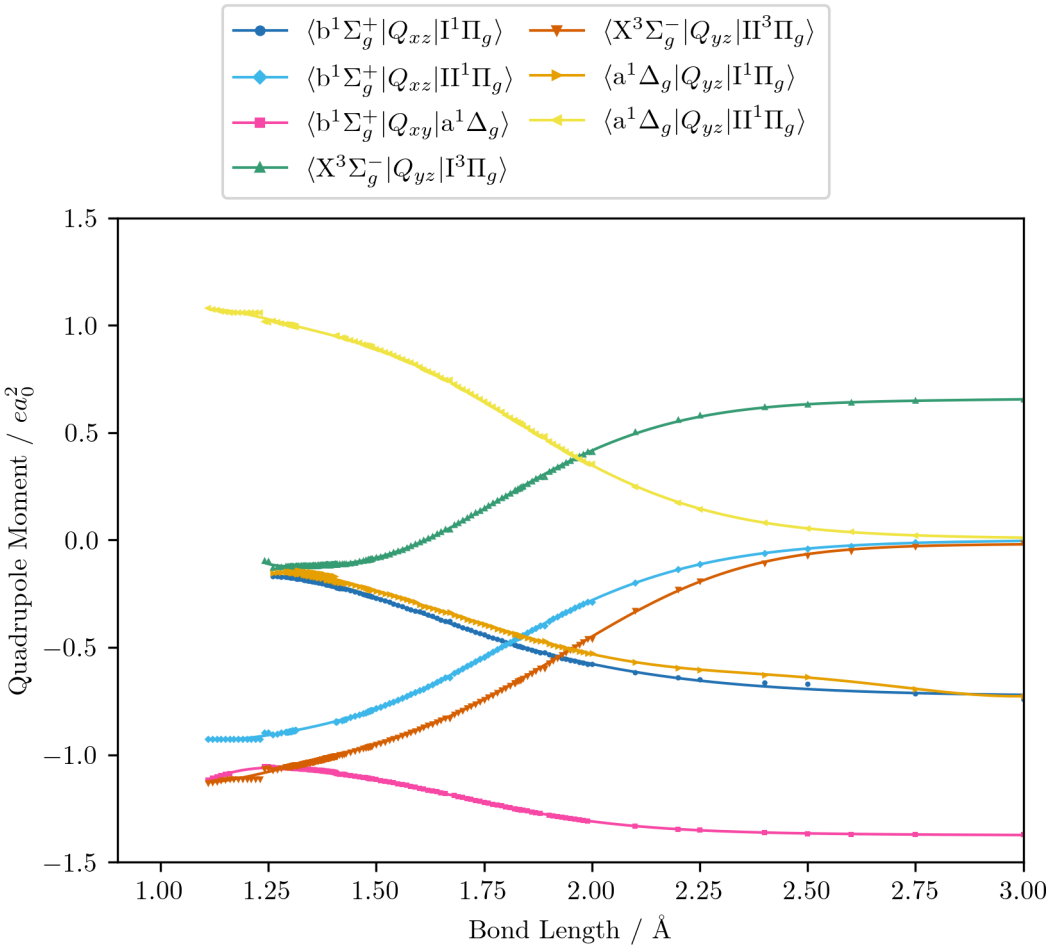

Figure 5.4: The off-diagonal EQCs obtained from *ab initio* electronic structure calculations (dots) along with the continuous curves (solid lines) obtained by fitting the analytic coupling functions to these *ab initio* data.

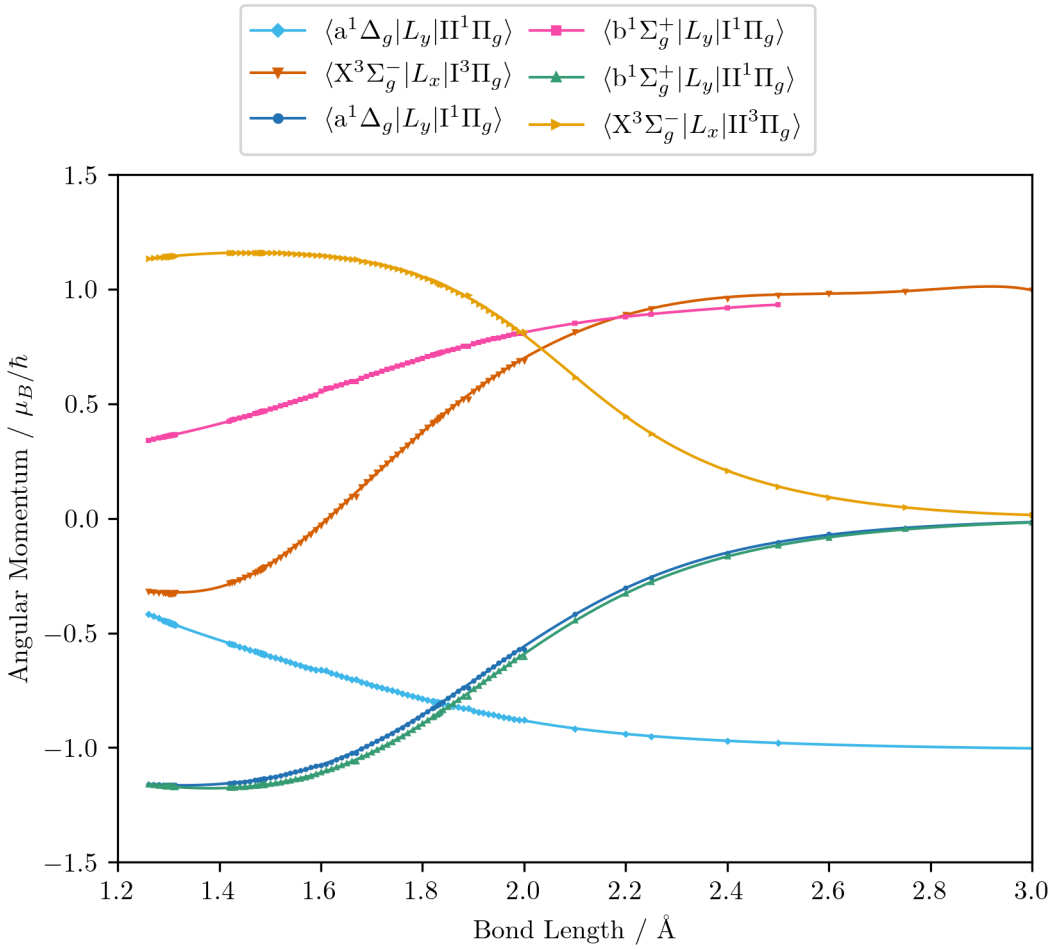

Figure 5.5: The EAMCs obtained from *ab initio* electronic structure calculations (dots) along with the continuous curves (solid lines) obtained by fitting the analytic coupling functions to these *ab initio* data.

behaviour of molecular potential energy surfaces. We fit a form of the MLR potential described by the following expression,

$$V(r) = T_e + (A_e - T_e)\left(1 - \frac{u(r)}{u(r_e)} e^{-\beta(r) y_p^{r_e}(r)}\right)^2 \tag{5.4.1}$$

with T_e the potential minimum (at spatial coordinate r_e) and A_e the dissociation energy, relative to the zero-point energy. The polynomial function $\beta(r)$ and the long-range function $u(r)$ ensure the function has the correct long-range behaviour,

$$\beta(r) = y_p^{r_{\text{ref}}}(r)\beta_\infty \left(1 - y_p^{r_{\text{ref}}}(r)\right) \sum_{i=0}^{N_\beta} \beta_i (y_q^{r_{\text{ref}}})^i \tag{5.4.2}$$

$$y_p^{r_x}(r) = \frac{r^p - r_x^p}{r^p + r_x^p} \tag{5.4.3}$$

where p is an integer greater than 1, the value of which is a hyper-parameter of the fitting procedure. The long-range function is $u(r) = \sum_n \frac{C_n}{r^n}$, where one or more of the coefficients C_n may be equal to zero. In the limit $r \to \infty$, the function approaches the $\beta_\infty = \ln\left(\frac{2\mathcal{D}_e}{u(r_e)}\right)$ where r_e is the equilibrium bond length, and r_{ref} is some reference geometry. In all fits $r_{\text{ref}} := r_e$ is selected for simplicity.

For the two dissociative potentials ($\mathrm{I}\,^1\Pi_g$ and $\mathrm{I}\,^3\Pi_g$) we fit a repulsive potential in the form of a Laurent power series in the radial distance,

$$V(r) = T_e + \sum_i \frac{a_i}{r^i} \tag{5.4.4}$$

where a_i are the fitted coefficients. The fits for all potential energy curves are performed with the Python library `scipy`, using the Levenberg-Marquadt (LM) algorithm in the case of the dissociative potentials and the *trust region reflective* (TRF) algorithm with a soft L1 loss function in the case of the bound potentials. For each of the bound potentials we set a single dispersion parameter, namely C_6, to be non-zero and fix the value as $C_6 = 2.95 \times 10^5\, E_\mathrm{h}\mathrm{cm}^{-6}$ [157]. The equilibrium bond length is bounded to remain within the range 0.9–3.0 Å, and the dissociation and excitation energies are bounded in the range of positive real numbers.

In Table 5.2 we compare several key spectroscopic parameters obtained from the bound potentials obtained in this work to experimental and other *ab initio* values, whilst Tables 5.3 and 5.4 provide the values of the potential parameters obtained during the fitting procedure for the five electronic states.

	D_e (eV)	T_e (cm^{-1})	R_e (nm)	ω_e (cm^{-1})	B_e (cm^{-1})	$10^2\alpha_e$ (cm^{-1})
$X\,^3\Sigma_g^-$	5.2146	0.0	0.12078	1590.16	1.4478	1.6207
Exp. [14]	5.2142	0.0	–	–	–	–
Exp. [15]	5.2132	0.0	0.12075	1580.19	1.4456	1.59
Cal. [13]	5.2203	0.0	0.12068	1581.61	1.4376	1.2539
$a\,^1\Delta_g$	4.2313	7930.39	0.12229	1495.69	1.4083	1.4283
Exp. [158]	4.2258	7918.11	0.12157	(1509.3)	1.4263	1.71
Exp. [15]	–	7918.1	–	[1483.5]	1.4264	1.71
Cal. [13]	4.2258	7776.43	0.12147	1491.07	1.3814	0.4238
$b\,^1\Sigma_g^+$	3.5786	13195.4	0.12366	1423.20	1.3798	1.6138
Exp. [158]	3.5772	13195.31	0.12268	(1432.67)	1.4005	1.8169
Cal. [13]	3.6058	13099.92	0.12258	1438.65	1.4030	1.8018
$II\,^3\Pi_g$	0.6135	52800.3	0.14880	625.40	0.9520	4.1312
$II\,^1\Pi_g$	1.2633	63500.6	0.14540	880.86	0.9964	2.0501

Table 5.2: Key spectroscopic parameters obtained for the bound *ab initio* potentials presented in this work, compared to those obtained by Liu et al. [13] and experimental parameters from Ruscic et al. [14] and Huber and Herzberg [15]. Values in square brackets indicate uncertain data, and those in rounded brackets indicate vibrationally averaged values obtained for the ground $v = 0$ state.

	$X\,^3\Sigma_g^-$	$a\,^1\Delta_g$	$b\,^1\Sigma_g^+$	$II\,^3\Pi_g$	$II\,^1\Pi_g$
r_e (Å)	1.208	1.223	1.237	1.488	1.454
D_e (cm^{-1})	4.206×10^4	4.206×10^4	4.206×10^4	5.775×10^4	7.369×10^4
T_e (cm^{-1})	1.000×10^{-10}	7.930×10^3	1.320×10^4	5.280×10^4	6.350×10^4
β_0	-1.899	-1.791	-1.721	-2.433	-2.622
β_1	-1.447	-1.124	-8.766×10^{-1}	-8.444×10^{-1}	-2.224×10^{-1}
β_2	-1.385	-1.206	-1.017	-1.524	-1.562
β_3	-1.207×10^1	-4.265	-2.894	-1.206×10^1	-1.204×10^1
β_4	7.266×10^1	1.470×10^1	9.736	7.266×10^1	7.267×10^1
β_5	-2.678×10^2	-3.039×10^1	-1.947×10^1	-2.678×10^2	-2.678×10^2
β_6	5.451×10^2	2.222×10^1	1.464×10^1	5.451×10^2	5.451×10^2
β_7	-5.985×10^2	–	–	-5.985×10^2	-5.985×10^2
β_8	2.781×10^2	–	–	2.781×10^2	2.781×10^2
C_6	2.950×10^5	2.950×10^5	2.950×10^5	2.950×10^5	2.950×10^5

Table 5.3: Fitted parameters for the *ab initio* MLR potential energy curves for the bound electronic states.

	$I\,^1\Pi_g$	$I\,^3\Pi_g$
C_0	1.028×10^4	4.526×10^4
C_1	3.159×10^5	-2.865×10^4
C_2	-1.065×10^6	1.510×10^5
C_3	1.328×10^6	-4.654×10^5
C_4	-3.351×10^5	5.716×10^5

Table 5.4: Fitted repulsive potential parameters for the *ab initio* PECs of the two dissociative Π states.

5.4.2 Spin-Orbit Coupling Curves

The use of a polynomial decay expansion as an analytic representation of the spin-orbit coupling interaction was introduced by Prajapat et al. [159] and has been used in a number of diatomic spectroscopic models (see e.g Semenov et al. [160] or Yurchenko et al. [161]). The polynomial decay function has the form

$$F(r) = \sum_{i=0}^{N_B} B_i z^i \left(1 - y_p^{r_{\rm ref}}\right) + y_p^{r_{\rm ref}} B_\infty \tag{5.4.5}$$

where y_p is the Šurkus variable defined by equation (5.4.3), and z is taken as the damped coordinate

$$z = (r - r_{\rm ref}) e^{-\beta_2 (r - r_{\rm ref})^2 - \beta_4 (r - r_{\rm ref})^4} \tag{5.4.6}$$

We use the same representation to parameterize all seven SOCs in the present work, and the parameters are presented in Table 5.5. Initially we attempted a 3rd order polynomial fit for all SOCs, using TRF and a linear loss function. For each SOC the order of the polynomial is then increased until the fit converges with an R^2 value greater than 0.95. This ensures a good fit whilst minimizing the degree of overfitting.

5.4.3 Quadrupole and Angular Momentum Curves

Analytic representations of the EQMCs have not been widely used in the existing literature. We find that the LM algorithm is successful in parameterizing the fourteen quadrupole moment curves with the same polynomial decay function, although higher order polynomials are often required in order to ensure convergence.

To obtain good fits of the EAMCs we find a variety of analytic forms are needed. The polynomial decay function defined by Eqs. (5.4.3) and (5.4.6) is used to represent the $\langle \mathrm{a}\,^1\Delta_g | L_y | \mathrm{II}\,^1\Pi_g \rangle$ curve, with a 6-th order polynomial. The $\left\langle \mathrm{X}\,^3\Sigma_g^- \middle| L_x \middle| \mathrm{I}\,^3\Pi_g \right\rangle$ EAMC is represented by a simple polynomial expansion of the 10-th order with the form

$$F(r) = T_e + a_1 (r - r_{\rm ref}) + a_2 (r - r_{\rm ref})^2 + \cdots \tag{5.4.7}$$

For all other EAMCs we find a good fit is possible using the so-called irregular Chebyshev polynomial, which was originally introduced by Medvedev and Ushakov [162] to represent electronic dipole moment curves and has the form

$$F(r) = \frac{\left(1 - e^{c_2 r}\right)^3}{\sqrt{\left(r^2 - c_3^2\right)^2 + c_4^2}\sqrt{\left(r^2 - c_5^2\right)^2 + c_6^2}} \sum_{k=0}^{6} b_k T_k \left(z_1(r)\right) \tag{5.4.8}$$

where $T_k(z)$ are the Chebyshev polynomials of the first kind, b_k are the expansion coefficients and

$$z_1(r) = 1 - 2e^{-c_1 r} \tag{5.4.9}$$

maps the $r \in [0, \infty]$ half-infinite interval to the $z \in [-1, +1]$ finite interval. The parameters b_i and c_i are the fitting parameters. As with the SOCs, we find a variety of polynomial orders are required to fit individual EAMCs. The fitted parameters for each of the EAMCs and EQMCs are given in Tables 5.6 - 5.9.

5.4.4 Spin-Spin Curves

In addition to the *ab initio* curves given above, we must also account for the spin splitting of the triplet ground state, which is crucial for the production of the $b\,^1\Sigma_g^+$ – $X\,^3\Sigma_g^-$ magnetic dipole transitions Eq. (5.2.10). Tinkham and Strandberg [163] [164] estimated the magnitude of the separation as $1.17\,\mathrm{cm}^{-1}$. In Duo the spin splitting can produced by the inclusion of the phenomenological spin-spin operator[64]. In the absence of *ab initio* data for the spin-spin coupling curve, the strength of the coupling is usually obtained by fitting a functional form to experimental data. Commonly a Šurkus polynomial is used, of the form

$$F(r) = \left(1 - y_p^{r_{\mathrm{ref}}}\right) \sum_{i=0}^{N_A} A_i \left(y_p^{r_{\mathrm{ref}}}\right) + y_p^{r_{\mathrm{ref}}} A_\infty \tag{5.4.10}$$

where $y_p^{r_{\mathrm{ref}}}$ is given by Eq. (5.4.9) with $r_{\mathrm{ref}} := r_e$, the equilibrium bond length. Initially we obtain the spin-spin splitting by manually defining a zeroth order polynomial such that the energy of the phenomenological operator at the equilibrium bond length matches the experimentally measured energy separation, and decays to zero for long bond lengths. This polynomial is parameterised in Table 5.10.

5.5 The Ab Initio Spectroscopic Model

Using the analytic representation of the *ab initio* curves obtained in section 5.4, we build a spectroscopic model for the electric quadrupole and magnetic dipole transitions of $^{16}O_2$ in the infrared and visible region of the electromagnetic spectrum. We include transitions between all states lower in energy than $80\,000\,\mathrm{cm}^{-1}$. In solving the nuclear Schrödinger equation, a vibrational sinc-DVR basis set for each electronic state is defined on a grid of 1001 points in the range 0.90–3.00 Å. The vibronic basis sets are then truncated to the lowest 30 vibrational levels in the case of the $X\,^3\Sigma_g^-$, $a\,^1\Delta_g$, and $b\,^1\Sigma_g^+$ states, and to the lowest 300 vibrational levels for the $II\,^1\Pi_g$, $II\,^3\Pi_g$, $I\,^1\Pi_g$, and $I\,^3\Pi_g$states. We then solve for rotational levels up to $J = 50$. A large number of vibrational

	$\langle \mathrm{X}\,^3\Sigma_g^- \vert LS_z \vert \mathrm{b}\,^1\Sigma_g^+ \rangle$	$\langle \mathrm{X}\,^3\Sigma_g^- \vert LS_x \vert \mathrm{II}\,^1\Pi_g \rangle$	$\langle \mathrm{X}\,^3\Sigma_g^- \vert LS_x \vert \mathrm{I}\,^1\Pi_g \rangle$	$\langle \mathrm{a}\,^1\Delta_g \vert LS_x \vert \mathrm{II}\,^3\Pi_g \rangle$	$\langle \mathrm{a}\,^1\Delta_g \vert LS_x \vert \mathrm{I}\,^3\Pi_g \rangle$	$\langle \mathrm{b}\,^1\Sigma_g^+ \vert LS_x \vert \mathrm{II}\,^3\Pi_g \rangle$	$\langle \mathrm{b}\,^1\Sigma_g^+ \vert LS_x \vert \mathrm{I}\,^3\Pi_g \rangle$
r_e (Å)	5.486×10^{-1}	1.512	1.479	4.951×10^{-1}	1.252	1.122	4.355×10^{-1}
β_2	1.913×10^{-3}	8.349×10^{-1}	1.053	-2.715×10^{-1}	9.549	5.933×10^{-1}	-4.094×10^{-1}
β_4	3.211×10^{-2}	2.753	2.429	6.886×10^{-2}	−4.234	6.401×10^{-1}	4.894×10^{-3}
B_∞	-5.327×10^{-4}	-5.428×10^{-6}	-2.091×10^{-4}	-9.199×10^{-5}	1.969×10^{-4}	9.833×10^{-5}	3.026×10^{-4}
B_0	2.064×10^{-2}	2.358×10^{-4}	6.420×10^{-5}	2.723×10^{-2}	1.684×10^{-4}	2.374×10^{-4}	1.012×10^{-1}
B_1	-8.905×10^{-2}	3.825×10^{-4}	4.149×10^{-4}	-1.160×10^{-1}	2.998×10^{-5}	3.962×10^{-4}	-1.422×10^{-1}
B_2	1.349×10^{-1}	4.535×10^{-4}	2.607×10^{-4}	1.845×10^{-1}	5.566×10^{-4}	8.052×10^{-4}	-2.062×10^{-3}
B_3	-1.248×10^{-1}	2.741×10^{-4}	6.368×10^{-4}	-1.694×10^{-1}	–	–	–
B_4	–	-9.760×10^{-4}	–	4.355×10^{-2}	–	–	–

Table 5.5: Fitted parameters for the polynomial decay functions representing the *ab initio* SOCs.

	$\langle \mathrm{a}\,^1\Delta_g \vert L_y \vert \mathrm{I}\,^1\Pi_g \rangle$	$\langle \mathrm{b}\,^1\Sigma_g^+ \vert L_y \vert \mathrm{I}\,^1\Pi_g \rangle$	$\langle \mathrm{b}\,^1\Sigma_g^+ \vert L_y \vert \mathrm{II}\,^1\Pi_g \rangle$	$\langle \mathrm{X}\,^3\Sigma_g^- \vert L_x \vert \mathrm{II}\,^3\Pi_g \rangle$
B_0	1.375	3.982×10^{-1}	1.197	2.003×10^{-1}
B_1	9.872×10^{-1}	1.625	9.279	5.673×10^{-1}
B_2	1.991	1.485	1.955	1.804
B_3	1.972	1.226	1.788	1.845
B_4	1.651	2.705	1.667	2.017
B_5	1.514	−1.050	1.495	1.434
B_6	−7.964	6.473×10^2	-2.386×10^2	3.168×10^2
B_7	−2.436	4.028×10^2	2.321×10^2	-8.852×10^1
B_8	1.355	9.993×10^2	2.287×10^2	2.229×10^2
B_9	1.077×10^1	2.260×10^2	-4.623×10^2	-3.072×10^2
B_{10}	1.713×10^1	4.468×10^2	3.699×10^2	-1.496×10^2
B_{11}	-2.996×10^1	5.853×10^1	-1.610×10^2	-1.546×10^2
B_{12}	1.161×10^1	8.969×10^1	3.288×10^1	-5.828×10^1

Table 5.6: The fitted parameters for the irregular Chebyshev polynomial functions representing some of the *ab initio* EAMCs.

$\langle \mathrm{a}\,^1\Delta_g \vert L_y \vert \mathrm{II}\,^1\Pi_g \rangle$		$\langle \mathrm{X}\,^3\Sigma_g^- \vert L_y \vert \mathrm{I}\,^3\Pi_g \rangle$	
r_{ref} (Å)	1.485	r_{ref} (Å)	1.443
β_2	4.062	B_0	-2.657×10^{-1}
β_4	2.182	B_1	9.715×10^{-1}
B_∞	−1.016	B_2	4.254
B_0	-5.910×10^{-1}	B_3	−2.404
B_1	1.667×10^{-1}	B_4	-2.060×10^1
B_2	3.980×10^{-1}	B_5	5.022×10^1
B_3	2.756	B_6	-5.535×10^1
B_4	4.030	B_7	3.324×10^1
B_5	-7.903×10^1	B_8	-1.041×10^1
		B_9	1.318

Table 5.7: The fitted parameters for the polynomial decay function representing the *ab initio* $\langle \mathrm{a}\,^1\Delta_g \vert L_y \vert \mathrm{II}\,^1\Pi_g \rangle$ EAMC and the polynomial function representing the *ab initio* $\left\langle \mathrm{X}\,^3\Sigma_g^- \middle\vert L_y \middle\vert \mathrm{I}\,^3\Pi_g \right\rangle$.

	$\langle X\,^3\Sigma_g^- \vert Q_{zz} \vert X\,^3\Sigma_g^- \rangle$	$\langle a\,^1\Delta_g \vert Q_{zz} \vert a\,^1\Delta_g \rangle$	$\langle b\,^1\Sigma_g^+ \vert Q_{zz} \vert b\,^1\Sigma_g^+ \rangle$	$\langle I\,^1\Pi_g \vert Q_{zz} \vert I\,^1\Pi_g \rangle$	$\langle II\,^1\Pi_g \vert Q_{zz} \vert II\,^1\Pi_g \rangle$	$\langle I\,^3\Pi_g \vert Q_{zz} \vert I\,^3\Pi_g \rangle$	$\langle II\,^3\Pi_g \vert Q_{zz} \vert II\,^3\Pi_g \rangle$
r_e (Å)	1.352	1.257	1.326	6.422×10^{-1}	1.408	1.426	1.326
β_2	7.118×10^{-1}	3.476×10^{-1}	1.647×10^{-1}	1.077	8.833×10^{-1}	5.684	9.386×10^{-1}
β_4	1.065×10^{-1}	-3.688×10^{-2}	-2.203×10^{-3}	-1.511×10^{-1}	-1.426×10^{-1}	2.673×10^{1}	-1.492×10^{-1}
B_∞	1.011	9.879×10^{-1}	9.648×10^{-1}	-3.465×10^{-1}	1.549	-4.390×10^{-1}	1.576
B_0	1.687×10^{-1}	-1.674×10^{-1}	-6.842×10^{-2}	3.732×10^{3}	1.559	−1.656	1.442
B_1	5.726×10^{-1}	-3.340×10^{-1}	-1.213×10^{-1}	-2.664×10^{4}	2.650	1.625	2.756
B_2	1.710	-4.038×10^{-1}	-1.712×10^{-1}	-2.706×10^{4}	2.502	−4.695	2.702
B_3	6.305	4.999	3.484	4.053×10^{5}	5.370	3.841×10^{1}	6.643
B_4	–	–	-9.653×10^{-1}	-6.285×10^{2}	–	-3.231×10^{2}	–
B_5	–	–	–	-2.557×10^{6}	–	-4.050×10^{3}	–
B_6	–	–	–	8.399×10^{3}	–	1.589×10^{4}	–
B_7	–	–	–	1.128×10^{7}	–	3.881×10^{5}	–
B_8	–	–	–	-1.084×10^{7}	–	-1.926×10^{6}	–

Table 5.8: The fitted parameters for the polynomial decay functions representing the *ab initio* diagonal EQMCs.

	$\langle b\,^1\Sigma_g^+ \vert Q_{xz} \vert I\,^1\Pi_g \rangle$	$\langle b\,^1\Sigma_g^+ \vert Q_{xz} \vert II\,^1\Pi_g \rangle$	$\langle b\,^1\Sigma_g^+ \vert Q_{xy} \vert a\,^1\Delta_g \rangle$	$\langle X\,^3\Sigma_g^- \vert Q_{yz} \vert I\,^3\Pi_g \rangle$	$\langle X\,^3\Sigma_g^- \vert Q_{yz} \vert II\,^3\Pi_g \rangle$	$\langle a\,^1\Delta_g \vert Q_{yz} \vert I\,^1\Pi_g \rangle$	$\langle a\,^1\Delta_g \vert Q_{yz} \vert II\,^1\Pi_g \rangle$
r_e (Å)	8.817×10^{-1}	1.160	1.249	6.788×10^{-1}	1.070	1.082	1.162
β_2	4.383×10^{-1}	7.516×10^{-1}	1.431	3.396×10^{-1}	1.649×10^{-1}	5.445×10^{-2}	6.856×10^{-1}
β_4	-4.011×10^{-2}	4.139×10^{-2}	4.539×10^{-1}	-1.238×10^{-4}	2.096×10^{-1}	-8.297×10^{-6}	5.925×10^{-2}
B_∞	-7.336×10^{-1}	3.733×10^{-3}	−1.377	6.542×10^{-1}	-1.447×10^{-2}	2.276	2.203×10^{-3}
B_0	-1.792×10^{-1}	-9.281×10^{-1}	−1.060	3.453×10^{2}	−1.123	-4.511×10^{-1}	1.066
B_1	1.903×10^{-4}	−2.325	8.294×10^{-1}	-1.975×10^{3}	−3.411	−5.007	2.429
B_2	1.194×10^{1}	−2.875	-2.960×10^{-1}	3.825×10^{3}	−2.358	−7.757	2.913
B_3	1.391×10^{1}	-1.002×10^{1}	2.645	-2.618×10^{3}	-1.599×10^{1}	-8.816×10^{1}	1.296×10^{1}
B_4	–	–	–	–	1.516	1.349×10^{2}	–
B_5	–	–	–	–	–	-1.548×10^{2}	–
B_6	–	–	–	–	–	1.507×10^{1}	–
B_7	–	–	–	–	–	1.891×10^{1}	–
B_8	–	–	–	–	–	1.881×10^{1}	–
B_9	–	–	–	–	–	-1.763×10^{1}	–

Table 5.9: The fitted parameters for the polynomial decay functions representing the *ab initio* off-diagonal EQMCs.

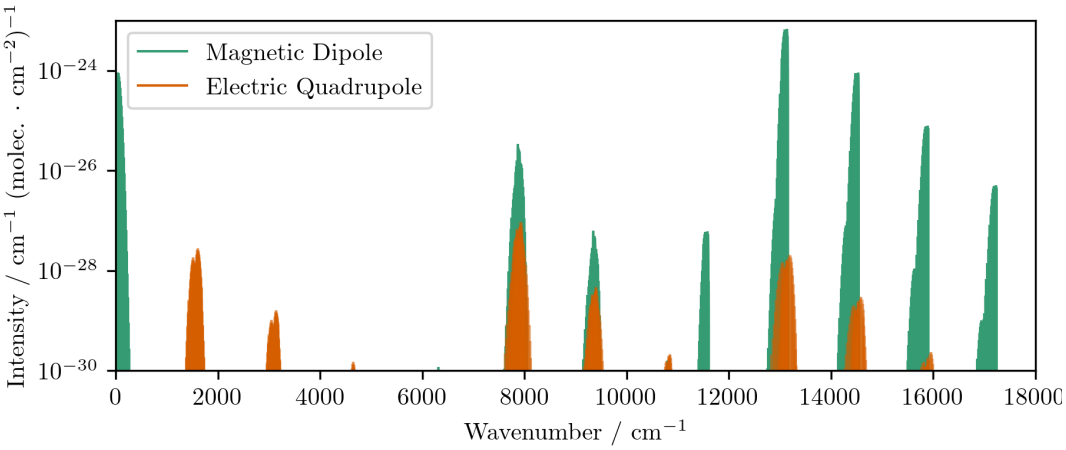

Figure 5.6: The *ab initio* electric quadrupole and magnetic dipole line list at 296 K for $^{16}O_2$ in the wavenumber range 0–1800 cm^{-1}.

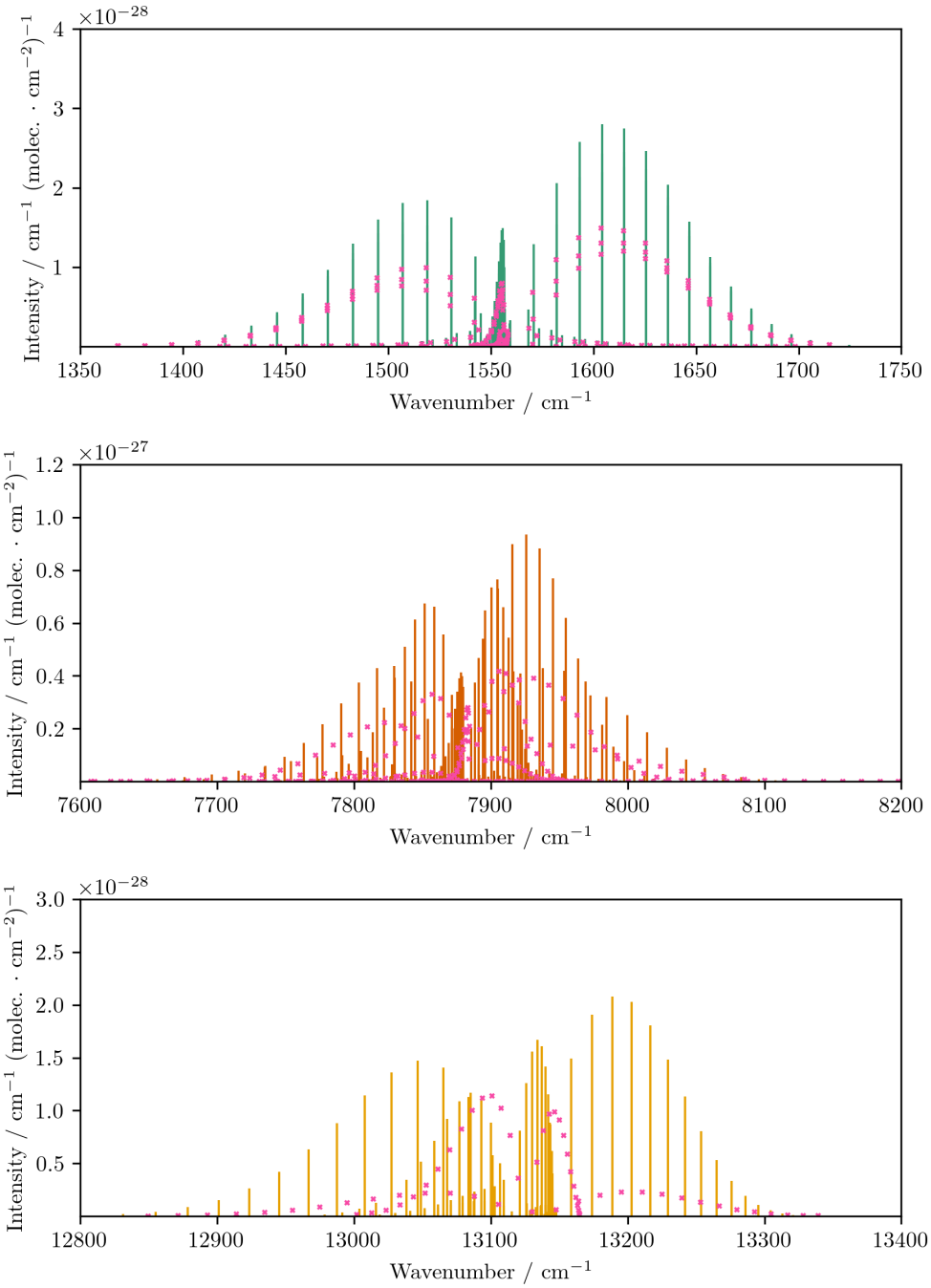

Figure 5.7: Comparison of the most intense electric quadrupole transitions in the $X\,^3\Sigma_g^-$ – $X\,^3\Sigma_g^-$ (top), $a\,^1\Delta_g$ – $X\,^3\Sigma_g^-$ (middle) and $b\,^1\Sigma_g^+$ – $X\,^3\Sigma_g^-$ (bottom) bands. Vertical lines indicate the intensities predicted by the *ab initio* Duo model, and the pink markers the transition intensities recorded in the HITRAN database.

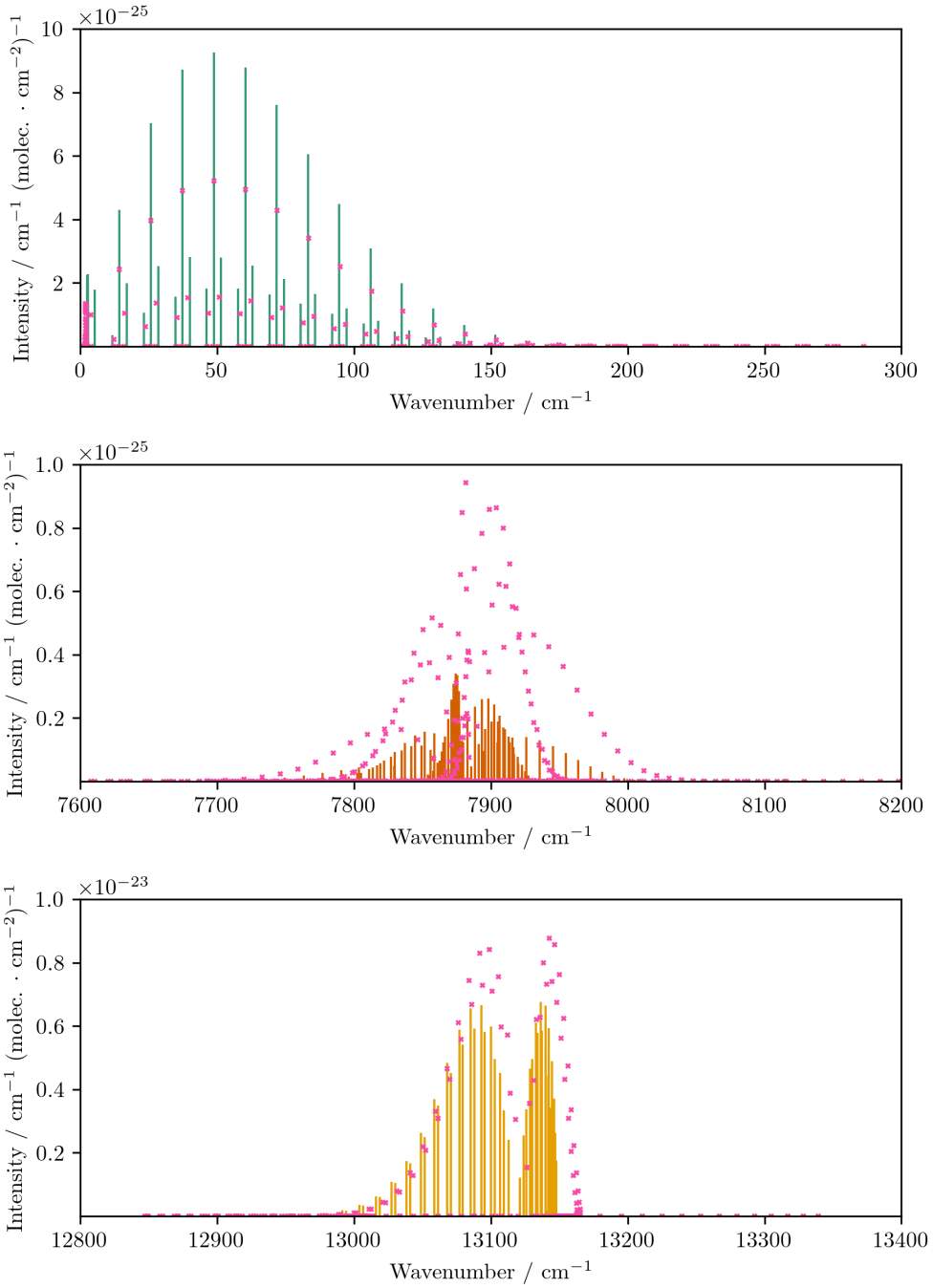

Figure 5.8: Comparison of the most intense magnetic dipole transitions in the $X\,^3\Sigma_g^-$ – $X\,^3\Sigma_g^-$ (top), $a\,^1\Delta_g$ – $X\,^3\Sigma_g^-$ (middle) and $b\,^1\Sigma_g^+$ – $X\,^3\Sigma_g^-$ (bottom) bands. Vertical lines indicate the intensities predicted by the *ab initio* Duo model, and the pink markers the transition intensities recorded in the HITRAN database.

	$\left\langle \mathrm{X}^3\Sigma_{g,0}^- \middle\vert H_{SS} \middle\vert \mathrm{X}^3\Sigma_{g,1}^- \right\rangle$
r_{ref}	1.2075
p	4
A_0	1.0570
A_∞	0.0000

Table 5.10: The fitted parameters for the Šurkus polynomial function representing the spin-spin splitting of the *ab initio* $\mathrm{X}\,^3\Sigma_g^-$ state.

basis states are retained for the weakly bound and dissociative Π state in order to represent continuum states above the dissociation energy [165, 166].

Initially I present a line list using a purely *ab initio* model, without empirical refinement of the potential energy or coupling curves. In Fig. 5.6 we show the absorption intensities for the electric quadrupole and magnetic dipole moments, respectively, above a threshold of $10^{-30}\,\mathrm{cm\,molecule^{-1}}$. In Figs. 5.7 and 5.8 we compare the calculated intensities and line positions to accurate known data from the HITRAN database [167], namely the $\mathrm{X}\,^3\Sigma_g^-(v=1) \rightarrow \mathrm{X}\,^3\Sigma_g^-(v=0)$ (E2), $\mathrm{X}\,^3\Sigma_g^-(v=0) \rightarrow \mathrm{X}\,^3\Sigma_g^-(v=0)$ (M1), $\mathrm{a}\,^1\Delta_g(v=0) \rightarrow \mathrm{X}\,^3\Sigma_g^-(v=0)$, and $\mathrm{b}\,^1\Sigma_g^+(v=0) \rightarrow \mathrm{X}\,^3\Sigma_g^-(v=0)$ transitions. In addition to the six bands vibrational bands present in the HITRAN database, we also obtain intensities for 14 additional vibrational bands above the threshold intensity of $10^{-30}\,\mathrm{cm\,molecule^{-1}}$.

The *ab initio* model reproduces the expected intensities to the correct order of magnitude, with the largest discrepancies observed for the $^{\mathrm{N}}\mathrm{O}$ and $^{\mathrm{T}}\mathrm{S}$ branches of the $\mathrm{b}\,^1\Sigma_g^+ - \mathrm{X}\,^3\Sigma_g^-$ electric quadrupole transitions. These branches correspond to $\Delta N = -3$, $\Delta J = -2$ and $\Delta N = +3$, $\Delta J = +2$ transitions, respectively. Crucially, the combination of PECs and couplings present in the model successfully reproduces all of the observed rotational bands. To illustrate the role of the excited Π states we also reduce the model to a simple three state model that contains only the $\mathrm{X}\,^3\Sigma_g^-$, $\mathrm{a}\,^1\Delta_g$, and $\mathrm{b}\,^1\Sigma_g^+$ with their respective couplings. Without the inclusion of the four Π states, we find that no intensities for the $\mathrm{a}\,^1\Delta_g - \mathrm{X}\,^3\Sigma_g^-$ magnetic dipole transitions are produced, and the $^{\mathrm{P}}\mathrm{O}$ and $^{\mathrm{R}}\mathrm{S}$ branches ($\Delta N = -1$, $\Delta J = -2$ and $\Delta N = +1$, $\Delta J = +2$) of the $\mathrm{b}\,^1\Sigma_g^+ - \mathrm{X}\,^3\Sigma_g^-$ electric quadrupole transitions are also not reproduced. In Fig. 5.9 we compare the intensities obtained with and without the inclusion of the Π states.

5.6 Empirical Refinement

Whilst the *ab initio* spectroscopic model presented in Sec. 5.5 is sufficient to generate each of the bands observed experimentally, it can only provide a

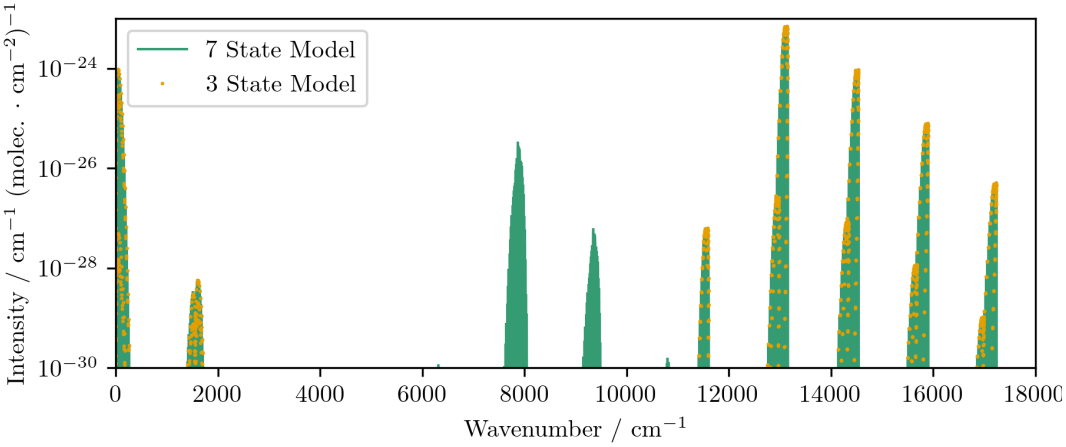

Figure 5.9: A comparison of the magnetic dipole line list obtained using the only the three low-lying electronic states to that obtained when the excited Π states are included, which demonstrates the importance of the Π states in producing intensities for the a $^1\Delta_g$ – X $^3\Sigma_g^-$ transitions.

qualitative agreement. In particular, the line positions and intensities of purely *ab initio* models tend to compare poorly to experimental measurements owing to the large number of interactions which can compound inaccuracies in the various curves, or subtle deviations due to higher order interactions that are not accounted for. In order to improve the model, and to more confidently predict the line position and intensity of novel, experimentally *unobserved* absorption lines, the model must be empirically refined. This can be done by iteratively refining the parameters of the analytic potential energy curves and couplings introduced in Sec. 5.4. The Duo program's fitting routine allows one to perform a least-squares fit of the calculated rovibronic state energies to accurately known state energies, usually derived from experimental data.

In many cases however, it is not possible to obtain direct measurements of state energies from experimental studies. Instead, experimental spectroscopy produces a set of accurate *transition frequencies*. Thus, reconstructing the state energies becomes an exercise in building a self consistent so-called *spectroscopic network* (SN). A spectroscopic network is an undirected weighted graph in which state energies are the graph nodes, and transition frequencies the edges. The MARVEL program [168] is able to perform precisely this task, namely to create a self-consistent network, or set of networks, of state energies from experimentally measured transitions frequencies. Crucially, the MARVEL code is also able to assign uncertainties to the state energies, based on the uncertainty of the transition frequencies used to reconstruct the energy. This is invaluable for the purpose of empirically refining the spectroscopic

model as it allows the data points in the fit to be weighted according to their accuracy.

In this section I outline the SN used in the empirical refinement of the spectroscopic model outlined in Sec. 5.5. I then elaborate on the refinement procedure and the additional variables introduced to improve the expressivity of the spectroscopic model. I also present the optimised parameters of the refined spectroscopic model and provide an analysis of the predicted absorption lines.

5.6.1 The Oxygen Spectroscopic Network

The task of producing an accurate spectroscopic model for $^{16}O_2$ is greatly aided by the work of Furtenbacher et al. [9] which contains a database of some 15 946 rovibronic energy levels for the $X\,^3\Sigma_g^-$, $a\,^1\Delta_g$, $b\,^1\Sigma_g^+$, $c\,^1\Sigma_u^+$, $A\,^3\Sigma_u^+$, $A'\,^3\Delta_u$, and $B\,^3\Sigma_u^-$ states. These energy levels were largely produced through the MARVEL program. In particular, the SN they present contains a large number of highly accurate rovibrational energies for the $X\,^3\Sigma_g^-$, $a\,^1\Delta_g$, and $b\,^1\Sigma_g^+$ electronic states. Ordinarily, databases created using the MARVEL methodology contain energy levels determined exclusively from experimentally measured transitions. However, in the case of $^{16}O_2$, Furtenbacher et al. found it was necessary to include data obtained by two additional methods. In this section I will briefly describe the structure of this SN network and outline the elements that were used in the empirical refinement of the $^{16}O_2$ spectroscopic model presented in Sec. 5.5.

Effective Hamiltonian Levels

The first additional source of energy levels in the Furtenbacher database is an effective Hamiltonian. In addition to the 4279 energy levels obtained by applying the usual MARVEL methodology, the database was supplemented by 11 667 energy levels determined from effective Hamiltonians for the $X\,^3\Sigma_g^-$, $a\,^1\Delta_g$, $b\,^1\Sigma_g^+$, $c\,^1\Sigma_u^+$, $A\,^3\Sigma_u^+$, and $A'\,^3\Delta_u$ electronic states. These effective Hamiltonian levels were included to aid the calculation of partition and thermochemical functions. Crucially, they favoured completeness over accuracy for this purpose. As a result, their effective Hamiltonians were parameterised by the spectroscopic constants presented by Mérienne et al. [169], which may be less accurate than parameters with less coverage from other authors, such as Yoshino et al. [170].

Many of the state energies obtained via effective Hamiltonians have large uncertainties associated with them and these are illustrated in Fig. (5.10). More than 70 % of the energies have an associated uncertainty greater than $1\,cm^{-1}$, with more than 60 % greater than $10\,cm^{-1}$. Since large uncertainties tend to destabilise the refinement procedure the energies in the Furtenbacher

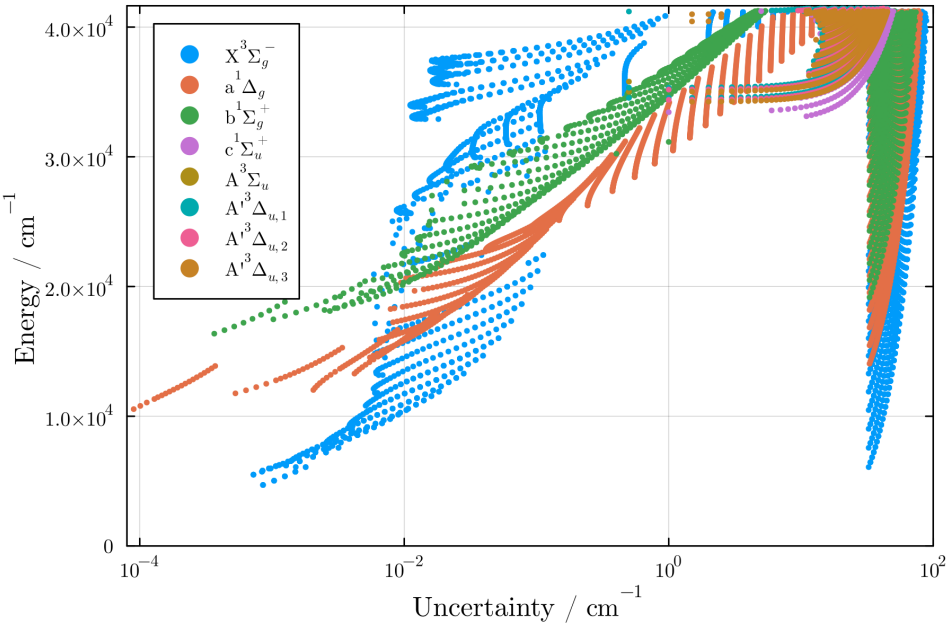

Figure 5.10: Distribution of uncertainities associated with the energy levels in the $^{16}O_2$ database of Furtenbacher et al. [9] that were obtained from an effective Hamiltonian.

et al. database ascribed to an effective Hamiltonian were excluded from the dataset used to perform the empirical refinement.

Artificial Transitions

The second technique employed by Furtenbacher et al. to improve the connectivity of the SN was the introduction of so-called 'artifical transitions' to the database. These are transitions that were reconstructed from the the energy levels of Yu et al. [171] by taking their difference from the ground $(J, N, v) = (0, 1, 0)$ $X\,^3\Sigma_g^-$ state. The artifical transitions were included in order to increase the size of the SN for the three lowest electronic states, which in turn allowed them to determine the energies of the highly excited electronic levels. Of the 30 671 transition that contributed to the MARVEL SN, 6295 are so-called artifical transitions. As a consequence, these artificial transitions do not have associated intensities, but their frequencies generally have a small uncertainty due to the accurate energy levels used to produce them. These artificial transitions are retained in the fitting procedure.

Relevant States

The majority of energy levels that appear in the database presented by Furtenbacher et al. are those of highly excited ungerade electronic states. Since these states do not play a role in the infrared electric quadrupole and magnetic dipole spectra, they are of little value in refining the *ab initio* spectroscopic model. Only 11 335 of their energy levels correspond to states relevant to the refinement procedure, and all of these are for the three lowest electronic states, namely the $X\,^3\Sigma_g^-$, $a\,^1\Delta_g$, and $b\,^1\Sigma_g^+$. The primary limitation of the database presented by Furtenbacher et al. [9] is thus the absence of energies for any rovibrational levels of the four $^3\Pi_g$ and $^1\Pi_g$ states. Moreover, to the author's knowledge, there is no experimental data for transitions involving these Π states, and thus their inclusion in *any* SN is not possible at present.

However, because these levels contribute to the energy and intensity of the infrared bands only indirectly, obtaining accurate potential energy curves for these states highly excited states is not essential to the production of an accurate linelist. Instead, the required corrections to the state energies can usually be absorbed into the empirical refinement of the coupling terms (namely spin-orbit) that connect the Π states to the lower electronic levels.

5.6.2 Spectroscopic Model

In this section I present the empirically refined spectroscopic model, including the refined analytic representation of the various *ab initio* curves introduced previously, as well as the parameterisation of additional correction terms introduced to account for interactions that are not fully described by the *ab initio* model. The empirical refinement of *ab initio* curves takes two forms. For many curves, it is possible to perform a straightforward fit of some analytic function that completely parameterises the energy levels, this is usually the case when the curve in question has good support in the dataset being used to perform the fitting. When this is not the case, and the dataset is insufficient to constrain an analytic function, a so-called 'morphing' function can be parameterised instead. In this case the fitted function is convolved with the *ab initio* data to produce an empirical curve that can improve the calculated energies. The advantage of the latter approach is that it allows for additional support for the empirical model to come from the *ab initio* data when there is insufficient coverage in the state energy dataset.

The empirical model is obtained by performing a weighted non-linear least-squares fit of the state energies predicted by Duo to those contained in the MARVEL spectroscopic database outlined in Sec. 5.6.1 In all cases the non-linear least-squares fit is obtained using the LAPACK DGELSS routine which is supported natively in the Duo program [64]. The least-squares fit is weighted according to the uncertainties of the energies levels which

are calculated according to the MARVEL procedure in order to produce a self-consistent spectroscopic network.

Due to the large number of total parameters available across all PECs and couplings, and the high degree of correlation between them, it is not usually possible to perform a simultaneous fit of all the curves. Instead each curve or a small subset of the curves is usually fitted sequentially on a carefully selected subset of the dataset that provides greatest support for the selected curve. Once a reasonable fit has been obtained across multiple curves, the parameters can be freely varied together for a simultaneous fit of two or more curves in order to obtain a high-quality self-consistent model.

Potential Energy Curves

The three low-lying electronic states, $\mathrm{X}\,^3\Sigma_g^-$, $\mathrm{a}\,^1\Delta_g$, and $\mathrm{b}\,^1\Sigma_g^+$, are parameterised in the empirical model using the same MLR function that was introduced in Eq. (5.4.1). The parameters obtained by fitting to the *ab initio* data (Table 5.3) are used as initial parameters. The dissociation energy of these states is well quantified by experimental data, and so the value of D_e, the dissociation energy relative to the zero point energy of the $\mathrm{X}\,^3\Sigma_g^-$ state is initially fixed according to the value provided by Ruscic et al. [14]. Similarly the minimum electronic energies of the $\mathrm{a}\,^1\Delta_g$ and $\mathrm{b}\,^1\Sigma_g^+$ states, and the equilibrium bond lengths of the $\mathrm{X}\,^3\Sigma_g^-$, $\mathrm{a}\,^1\Delta_g$, and $\mathrm{b}\,^1\Sigma_g^+$ states are initially fixed at the values provided by Krupenie [158] and Huber and Herzberg [15]. The remaining parameters are allowed to vary freely in the non-linear least squares fit which is obtained using the LAPACK DGELSS routine [64]. The dissipative coefficient C_6 is similarly held constant at the value $C_6 = 2.95 \times 10^5\,E_\mathrm{h}\mathrm{cm}^{-6}$ introduced in Sec. 5.4.1 [157]. Once a stable parameterisation of the polynomial coefficients β_i is obtained, further curves are fitted, as outlined below and finally the parameters r_e, D_e and T_e are allowed to vary freely only after no further improvement in the residuals can be achieved by varying other, empirically determined, parameters. We note that the final parameterisation of the state $\mathrm{X}\,^3\Sigma_g^-$, $\mathrm{a}\,^1\Delta_g$, and $\mathrm{b}\,^1\Sigma_g^+$, is remarkably consistent with the parameterisation obtained from the *ab initio* data, with a mean difference in the absolute value of the potential across the 1001 vibrational grid points of just 0.0022 %, 0.13 %, and 0.18 % for the $\mathrm{X}\,^3\Sigma_g^-$, $\mathrm{a}\,^1\Delta_g$, and $\mathrm{b}\,^1\Sigma_g^+$ states, respectively.

As outlined previously, the MARVEL dataset used to perform the empirical refinement contains no data about the Π states. The PECs for these states must therefore be excluded from the refinement procedure, and they are represented in the empirical model by the same PECs presented in Sec. 5.5. The close agreement of the empirical and *ab initio* PECs for the three low lying states suggests that the MRCI calculations provide an accurate characterisation of these properties. We can reasonably expect the parameterisation of the $\mathrm{I}\,^1\Pi_g$, $\mathrm{II}\,^1\Pi_g$, $\mathrm{I}\,^3\Pi_g$, and $\mathrm{II}\,^3\Pi_g$ to be be similarly accurate. Moreover, none

of the bands of interest involve the Π states directly, and so we expect that small errors in their energies will not significantly impact the predicted line positions. The energies of the Π states do, however, appear in the reciprocal of the coupling coefficients for Eqs (5.2.1)-(5.2.14). Thus we expect any shifts in the energy of the rovibrational Π states to have some small effect on the predicted intensity of certain bands where this contribution is not negligible.

	$X\,^3\Sigma_g^-$	$a\,^1\Delta_g$	$b\,^1\Sigma_g^+$
r_e (Å)	1.207	1.216	1.227
D_e (cm^{-1})	4.206×10^4	4.205×10^4	4.205×10^4
T_e (cm^{-1})	0.000×10^1	7.930×10^3	1.319×10^4
β_0	-1.898	-1.790	-1.719
β_1	-1.481	-1.114	-9.098×10^{-1}
β_2	-1.844	-1.172	-1.024
β_3	-1.211	-4.779	-2.788
β_4	-9.054×10^{-1}	1.671×10^1	9.212
β_5	-1.516×10^1	-3.392×10^1	-1.860×10^1
β_6	6.995×10^1	2.456×10^1	1.405×10^1
β_7	-1.335×10^2	–	–
β_8	9.314×10^1	–	–
C_6	2.950×10^5	2.950×10^5	2.950×10^5

Table 5.11: Fitted MLR parameters for the empirical PECs of the three low lying states.

Spin-Spin Curves

Once a reasonable fit to the state energies has been obtained by varying the parameters of the MLR PECs, one can begin to refine the model by varying the parameters of some coupling curves that contribute to the state energies. Particularly important in predicting the line positions of the $X\,^3\Sigma_g^-$ state rovibrational transitions is the magnitude of the spin splitting for this state. In Sec.5.4.4 a phenomenological spin-spin operator was introduced with an approximate parameterisation based on experimental measurements. To obtain a good qualitative characterisation of the spin splitting in the $X\,^3\Sigma_g^-$, the parameters of this coupling curve can be varied freely whilst fitting exclusively the energies of the spin sub-levels in the $X\,^3\Sigma_g^-$ state. Since the MARVEL dataset includes only the quantum numbers J, N and v, the assignment of the

	$\left\langle \mathrm{X}^3\Sigma_{g,0}^- \middle\vert H_{SS} \middle\vert \mathrm{X}^3\Sigma_{g,1}^- \right\rangle$
r_{ref}	1.2075
p	4
A_0	6.125×10^{-1}
A_1	-1.997×10^{-1}
A_∞	0.0000

Table 5.12: The fitted parameters for the empirical Šurkus polynomial function representing the spin-spin splitting of the $\mathrm{X}\,^3\Sigma_g^-$.

Σ quantum numbers, which are required to perform the Duo refinement, is done according to the energy ordering of the three spin sub-levels for a give J state. To obtain good agreement with the MARVEL dataset, a first order Šurkus polynomial of the form given by Eq. (5.4.10) is used, with parameters given in Table 5.12.

Spin-Orbit Curves

The spin-orbit coupling plays an important role in determining both the energy levels and transition intensities of the $^{16}O_2$ infrared system. This is especially true of the $\mathrm{X}\,^3\Sigma_g^-$– $\mathrm{b}\,^1\Sigma_g^+$spin-orbit coupling, which has a strong effect on the energies of the $\mathrm{X}\,^3\Sigma_g^-$ and $\mathrm{b}\,^1\Sigma_g^+$ states, and on the intensity of the $\Delta M = 0$ $\mathrm{X}\,^3\Sigma_g^-$ – $\mathrm{b}\,^1\Sigma_g^+$ band, Eq. (5.2.1). A good fit is found without recourse to varying the parameters of the spin-orbit curves relative to those obtained by fitting to the *ab initio* data, which are presented in Table 5.5.

Electronic Angular Momentum Curves

The primary role of the L_x and L_y operators in the infrared system of $^{16}O_2$ is their contribution to the intensities of these transitions via the magnetic dipole moments outlined in Sec. 5.2.2. However, they also play a role in determining the energy of the states involved. Specifically, the coupling of the electronic orbital angular momentum with the rotational motion of the nuclei results in so-called Λ-doubling, in which the $\pm\Lambda$ degeneracy of states with $|\Lambda| > 0$ is lifted [172]. In the case of $^{16}O_2$ this Λ-doubling effect is small, particularly for the $\mathrm{a}\,^1\Delta_g$ state [173]. Nonetheless, it is important to highlight the dual role that these coupling curves play in the the spectroscopic model, as it means that changes to the EAMCs in order to improve the prediction of state energies will also have implications for the intensity calculations, and vice versa.

The *ab initio* data obtained in Sec. 5.3 indicates that the strongest EAMC contribution to the $\mathrm{b}\,^1\Sigma_g^+$ – $\mathrm{X}\,^3\Sigma_g^-$ magnetic dipole bands arises from the magnetic moment between the $\mathrm{X}\,^3\Sigma_g^-$ and $\mathrm{II}\,^3\Pi_g$states, which lends intensity via the strong spin-orbit coupling between the $\mathrm{II}\,^3\Pi_g$ and $\mathrm{b}\,^1\Sigma_g^+$ states. The *ab initio*

model presented previously underestimates the strength of the $b\,^1\Sigma_g^+$ – $X\,^3\Sigma_g^-$ magnetic dipole transitions. In the empirical model, a morphing function of the form given by Eq. (5.4.5) is applied to the $\left\langle X\,^3\Sigma_g^-\middle|L_x\middle|II\,^3\Pi_g\right\rangle$ EAMC to improve the intensity predictions of this band. The parameters for this morphing function are given in Table 5.13.

The same dipole moment is also a contributor to the $a\,^1\Delta_g$ – $X\,^3\Sigma_g^-$ transitions. The intensities of these transitions in the *ab initio* model are also generally weaker than expected. The morphing function applied to the $\left\langle X\,^3\Sigma_g^-\middle|L_x\middle|II\,^3\Pi_g\right\rangle$ is not sufficient to reproduce the expected intensities, and so similar morphing functions are applied to the $\langle a\,^1\Delta_g|L_x|II\,^1\Pi_g\rangle$ and $\langle a\,^1\Delta_g|L_y|I\,^1\Pi_g\rangle$ moments, which contribute to the $a\,^1\Delta_g$ – $X\,^3\Sigma_g^-$ band according to Eq. (5.2.12).

The Duo program does not currently provide support for fitting curves to the transition intensities, and so the form of the morphing function is chosen manually to reproduce the expected intensity of known transitions. In all three cases, a zeroth-order polynomial decay function of the form given by Eq. (5.4.5) with the parameters in Table 5.13. The morphing function specified by these parameters has the essential effect of scaling the dipole moment around the equilibrium bond length, with the scaling approaching unity away from this point.

	Value
r_{ref} (Å)	1.21
β_2	8×10^{-2}
β_4	2×10^{-3}
B_∞	1
B_0	-1.4×10^{-1}

Table 5.13: The polynomial decay morphing function applied to the $\left\langle X\,^3\Sigma_g^-\middle|L_x\middle|II\,^3\Pi_g\right\rangle$, $\langle a\,^1\Delta_g|L_x|II\,^1\Pi_g\rangle$, and $\langle a\,^1\Delta_g|L_y|I\,^1\Pi_g\rangle$ moments to improve the predicted intensities.

Electric Quadrupole Moment Curves

The *ab initio* model in Sec. 5.5 overestimates the intensity of $X\,^3\Sigma_g^-$– $X\,^3\Sigma_g^-$ transitions significantly. Specifically, for the strongest transition in this band, $(v, J) = (1, 9) \leftarrow (0, 7)$ the ratio of the predicted intensity to measured intensity of the *ab initio* model is 1.63. To account for this difference, the diagonal EQMCs are scaled by a constant factor to reduce the intensity of the predicted lines. The $a\,^1\Delta_g$– $X\,^3\Sigma_g^-$ transitions are similarly overestimated by the *ab initio* model, with the most intense line $(v, J) = (0, 8) \leftarrow (0, 8)$, stronger by a factor of 1.76. The primary contribution to this band arises from the $a\,^1\Delta_g$– $b\,^1\Sigma_g^+$

quadrupole moment, Eq. (5.2.6), which is also reduced by a constant factor to improve the agreement of the predicted intensities.

5.7 Results and Discussion

The empirical spectroscopic model described previously can be used with the Duo program to produce a line list with broader spectral coverage than experimental measurements allow, and at a range of temperatures. In this section I present a line list constructed using the Duo and ExoCross programs [64, 127]. First I outline the details of the Duo calculation, including the rotational and vibrational basis used, as well as the thresholds below which calculated lines are discarded. I then provide a discussion of the results and compare a subset of the predicted lines to known transitions in order to benchmark the accuracy of the spectroscopic model and provide estimates of the accuracy of novel lines. Finally I present a temperature dependent line list for a selection of illustrative temperatures between 296–3000 K.

5.7.1 The Oxygen Linelist

The complete line list is presented in two parts in order to separate contributions from the electric quadrupole and magnetic dipole moments. These stick spectra can be combined with appropriate line broadening to produce a global absorption cross-section using the ExoCross program.

ID	E (cm^{-1})	g	J	$+/-$	e/f	State	v	$\lvert\Omega\rvert$	Σ	$\lvert\Lambda\rvert$
1	0.696753	1	0	+	e	X3Sigma-	0	0	0	0
2	1557.062584	1	0	+	e	X3Sigma-	1	0	0	0
3	3089.959814	1	0	+	e	X3Sigma-	2	0	0	0
4	4599.455575	1	0	+	e	X3Sigma-	3	0	0	0
5	6085.707922	1	0	+	e	X3Sigma-	4	0	0	0

Table 5.14: Excerpt from the beginning of the states file for $^{16}O_2$. ID: state counting number; E: state energy in cm^{-1}; g: total state degeneracy; J total rotational quantum number; $+/-$ total parity; e/f rotationless parity; State: electronic state label; v vibrational quantum number; $|\Omega|$: absolute value of the projection of the total angular momentum; Σ: the electronic spin projection; $|\Lambda|$: absolute value of the projection of the electronic orbital angular momentum.

The solution to the vibrational Schrödinger equation is obtained with vibrational grid consisting of 1001 points in the range 0.9–3.0 Å. The contracted

f	i	I_{fi} (cm molecule^{-1})	ν (cm^{-1})
2521	1	1.5744E-23	2.083529
2522	1	3.8711E-19	16.251618
2523	1	1.0116E-09	1558.436839
2524	1	9.0313E-10	1572.451408
2525	1	2.2777E-10	3091.322823

Table 5.15: Excerpt from the beginning of the transitions file for $^{16}O_2$. f: state counting number of the final state; i: state counting number of the initial state; I_{fi} absorption intensity in cm molecule^{-1}; ν transition frequency in cm^{-1}.

basis is then formed from the 40 lowest vibrational states for the X $^3\Sigma_g^-$, a $^1\Delta_g$, b $^1\Sigma_g^+$ states and the 300 lowest vibrational states for the I $^1\Pi_g$, II $^1\Pi_g$, I $^3\Pi_g$, II $^3\Pi_g$ states. A larger vibrational basis is used for the excited Π states in order to account for their dissociative nature. The vibrational wavefunctions for dissociative electronic states is properly treated as a continuum. However, the approach taken by the Duo program, which uses a sinc-DVR vibrational basis, results in particle-in-a-box wavefunctions, and effectively imposes an infinitely strong potential at the edges of the vibrational grid. Previous studies have shown that a large vibrational basis of bound states can recover the properties of overlap integrals associated with continuum states [165, 166]. The coupled rovibronic Schrödinger equation is then subsequently solved for $0 \leq J \leq 300$. Transitions in the range 0–2×10^4 cm^{-1} with an absorption intensity greater than 1×10^{-99} cm molecule^{-1} at 296.0 K are retained. This low intensity threshold is used to account for transitions that increase significantly in intensity at higher temperatures. The resultant line list is stored in two files, according to the ExoMol database format, excerpts from which are given in Tables 5.14 and 5.15 [174].

Before presenting the temperature dependent line list, I benchmark the empirical line list against known transitions. The transitions are compared line by line, with transitions matched first by rotational quantum numbers of the upper and lower state, then by vibrational and electronic levels. Finally, because the HITRAN line list does not assign spin quantum numbers, transitions that are degenerate in these six quantum numbers are sorted by frequency and matched according to the closest frequency transition. I present both qualitative visual comparisons and numerical results and discuss the structure of the predicted bands. The numerical metric used to compare line positions is the absolute difference in frequency, and to compare intensities I use the ratio between intensities predicted by Duo to those predicted by HITRAN [167],

$$\Delta\nu = |\nu^{\text{Duo}} - \nu^{\text{Hit.}}| \tag{5.7.1}$$

$$R_I = \frac{I^{\text{Duo}}}{I^{\text{Hit.}}} \tag{5.7.2}$$

5.7.2 Electric Quadrupole Transitions

The electric quadrupole absorption lines are relatively weak compared to electric dipole absorption in other species, or indeed magnetic dipole absorption in $^{16}O_2$. Nonetheless, they are in important consideration when performing exoplanetary retrievals, particularly as the intensity of Noxon band ($b\,^1\Sigma_g^+$ – $a\,^1\Delta_g$) exhibits a strong temperature dependence, and becomes the dominant electric quadrupole absorption mechanism in the 5000–5500 cm^{-1} region at approximately 1000 K. Figs. 5.11 - 5.13 provide comparisons of the electric quadrupole line positions and intensities at 296 K predicted by the empirical model to those from the HITRAN database. In general, there is good agreement between the line lists, and the empirical model presented in Sec. 5.6 reproduces all of the known electric absorption bands. Fig. 5.14 presents a numerical comparison of the transition frequencies and absorption intensities. In the $X\,^3\Sigma_g^-$– $X\,^3\Sigma_g^-$ $v = 1 \leftarrow 0$ band, the empirical model accurately reproduces the line positions of the three rotational bands, with the mean arithmetic difference of $\Delta\nu = 0.0115\,\text{cm}^{-1}$. The mean ratio of intensities for this band is $R_I = 0.831$. Meanwhile the $b\,^1\Sigma_g^+$– $X\,^3\Sigma_g^-$ $v = 1 \leftarrow 0$ band has a mean frequency difference of $\Delta\nu = 0.008\,72\,\text{cm}^{-1}$ with a mean ratio of intensities R_I 1.31. Thus the spectroscopic model tends to significantly overestimate one electronic band, whilst underestimating another. The matrix element that governs these transitions (Eq. 5.2.1) is formed as the difference of two quadrupole moments that are closely separated (Fig. 5.3), and thus are sensitive to small variations to either quadrupole moment. It is likely that the intensity predictions could be improved significantly by refining the parameters of analytic quadrupole moments via a fit to experimentally measured intensities. This is discussed further in Sec. 6.2. Nonetheless, considering that these electric quadrupole transitions are incredibly weak relative to ordinary electric dipole or even the $^{16}O_2$ magnetic dipole transitions, these results represent a very good quantitative agreement between the model's prediction and known intensities.

At face value, the agreement for the $a\,^1\Delta_g$– $X\,^3\Sigma_g^-$ $v = 0 \leftarrow 0$ band are less impressive, with a mean difference of $\Delta\nu = 0.101\,\text{cm}^{-1}$ in the line positions and a mean intensity ratio of $R_I = 16.4$, almost two orders of magnitude stronger than the HITRAN intensities. However, this strong disagreement is resolved when only considering transitions with intensity greater than $1 \times 10^{-30}\,\text{cm molecule}^{-1}$. The mean difference in line positions for this set of

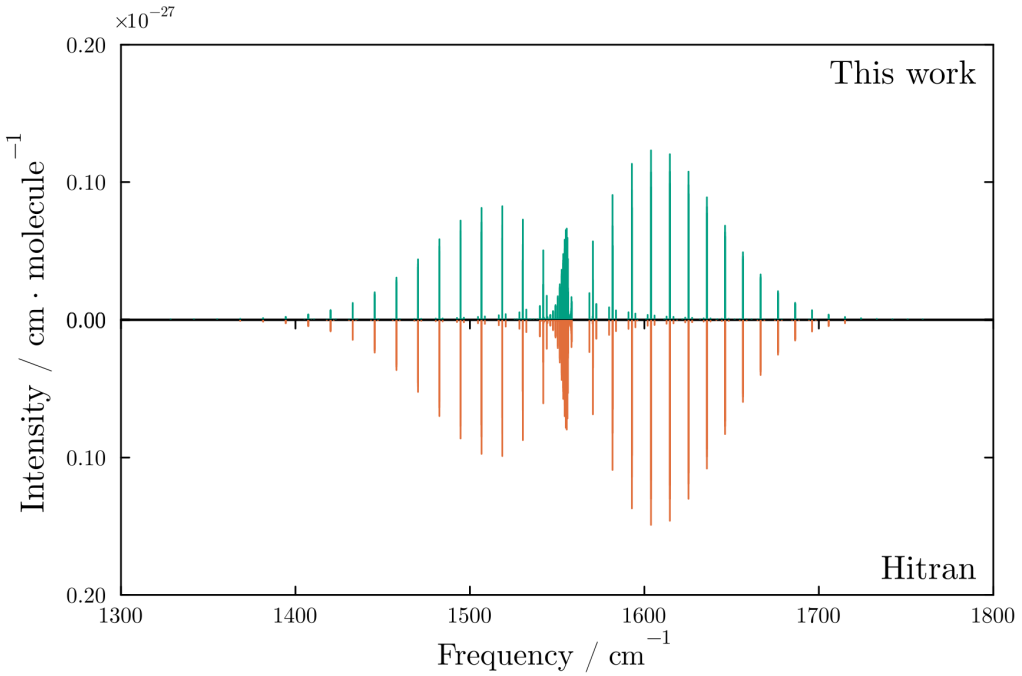

Figure 5.11: The electric quadrupole absorption lines of the $v = 1 \rightarrow 0$ $X\,^3\Sigma_g^- - X\,^3\Sigma_g^-$ transition, with the predicted intensities (top) shown in comparison to known intensities (bottom) from the HITRAN database.

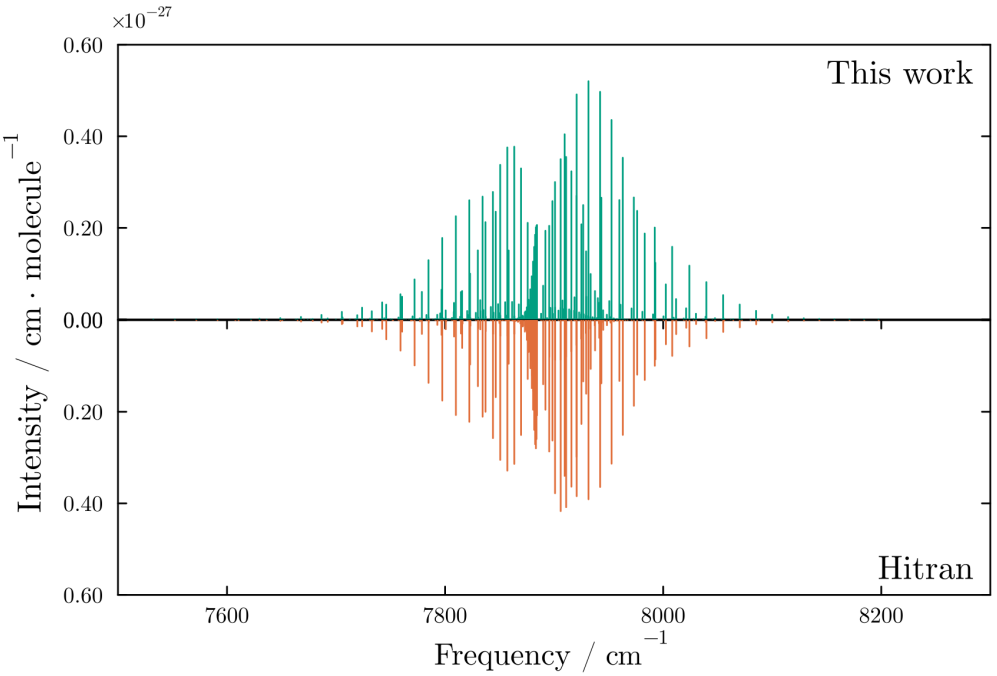

Figure 5.12: The electric quadrupole absorption lines of the $v = 1 \rightarrow 0$ $a\,^1\Delta_g^-$ $X\,^3\Sigma_g^-$ transition, with the predicted intensities (top) shown in comparison to known intensities (bottom) from the HITRAN database.

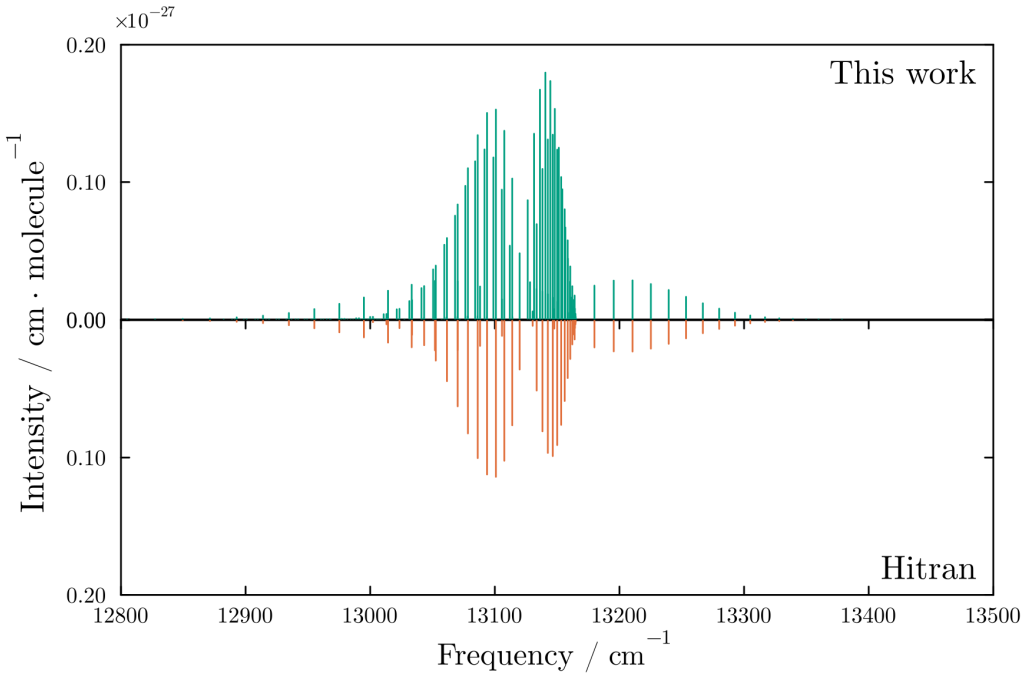

Figure 5.13: The electric quadrupole absorption lines of the $v = 1 \rightarrow 0$ $b\,^1\Sigma_g^+ - X\,^3\Sigma_g^-$ transition, with the predicted intensities (top) shown in comparison to known intensities (bottom) from the HITRAN database.

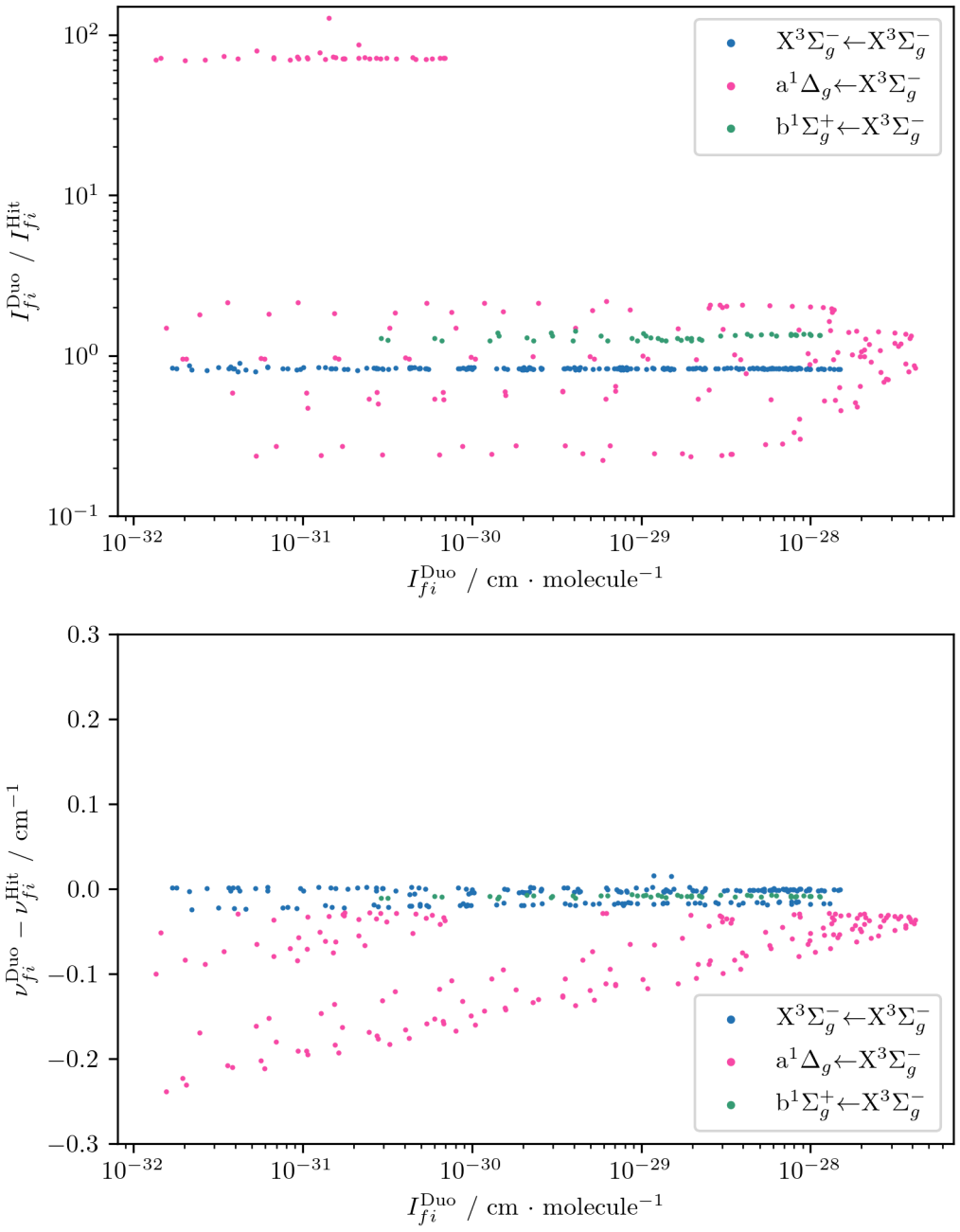

Figure 5.14: Numerical benchmarking of the electric quadrupole absorption intensities (top) and transition frequencies (bottom) predicted by the empirical spectroscopic model across the most intense vibrational bands.

transitions reduces to $\Delta\nu = 0.0744\,\mathrm{cm}^{-1}$ and the ratio of intensities to $R_I = 1.04$. Additionally, closer examination reveals that there is a group of transitions that appear as significant outliers in the ratio of absorption intensities (see the group of points at $R_I \sim 10^2$ in Fig. 5.14). These outliers all correspond to the branches with odd-numbered J_i, which HITRAN suggests are significantly weaker than the even-numbered J_i branches by approximately three orders of magnitude. In the case of these weaker transitions it is possible that second-order coupling terms may play a role in determining the absorption strength. Another possibility is that the 15 overlapping rotational branches for the $\mathrm{a}\,^1\Delta_g - \mathrm{X}\,^3\Sigma_g^-$ $v = 0 \leftarrow 0$ band make experimental measurements of these transitions challenging and that the intensities have been significantly overestimated.

5.7.3 Magnetic Dipole Transitions

The magnetic dipole transitions dominate the $^{16}O_2$ infrared and atmospheric bands, with the $\mathrm{b}\,^1\Sigma_g^+ - \mathrm{X}\,^3\Sigma_g^-$ band being approximately four orders of magnitude stronger than the most intense electric quadrupole lines. In Figs. 5.15 – 5.17 I provide comparisons of the magnetic dipole line positions and intensities at 296 K predicted by the empirical model to those from the HITRAN database. The $\mathrm{X}\,^3\Sigma_g^- - \mathrm{X}\,^3\Sigma_g^-$ $v = 0 \leftarrow 0$ transitions have a mean arithmetic difference in the wavenumber of $\Delta\nu = 0.0084\,\mathrm{cm}^{-1}$ and a mean ratio of intensities $R_I = 1.03$. The comparison presented in Fig. 5.15 illustrates this exceptionally good agreement. These transitions include also the microwave region around $2\,\mathrm{cm}^{-1}$ that result from zeroth order pure spin-flip transitions. The dominant contribution to these transitions is, in both cases, the spin magnetic moment (Eqs. (5.2.13) and (5.2.14)), which are evaluated analytically in Duo, thus it is unsurprising that excellent agreement with known intensities is found for these transition.

The $\mathrm{a}\,^1\Delta_g - \mathrm{X}\,^3\Sigma_g^-$ $v = 0 \leftarrow 0$ transitions have a mean wavenumber difference of $\Delta\nu = 0.0991$ and an intensity ratio of $R_I = 0.760$. This is the most complicated magnetic dipole band, with intensities that derive strength entirely from the coupling of the $\mathrm{X}\,^3\Sigma_g^-$ and $\mathrm{a}\,^1\Delta_g$ states to the highly excited Π states via two spin-orbit interactions. This complex coupling scheme is sensitive to not only the EAMCs, but also the SOCs, which could not be refined empirically due to a lack of data for the state energies of the Π states, thus it is unsurprising that we see weaker agreement for these absorption lines.

Finally, the $\mathrm{b}\,^1\Sigma_g^+ - \mathrm{X}\,^3\Sigma_g^-$ $v = 0 \leftarrow 0$ transitions, which constitute the strongest absorption band in this region of the EM spectrum (the oxygen A-band), have a mean wavenumber difference of $\Delta\nu = 0.0322\,\mathrm{cm}^{-1}$ and an intensity ratio $R_I = 1.16$. The dominant contribution to these intensities is from the same spin flips that generate the $\mathrm{X}\,^3\Sigma_g^- - \mathrm{X}\,^3\Sigma_g^-$ absorption lines, and

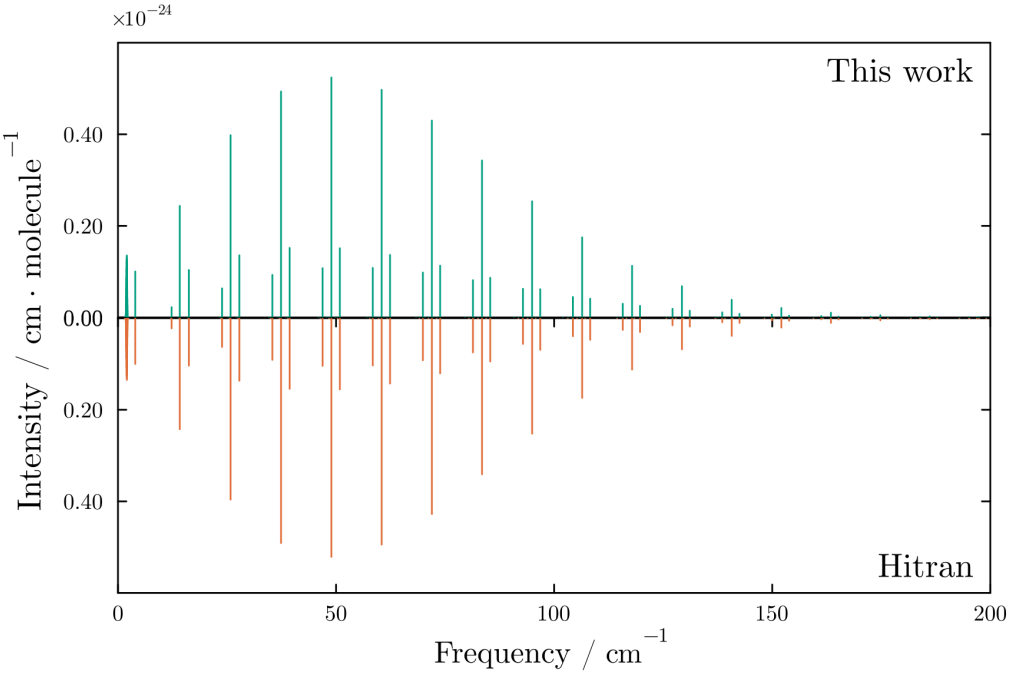

Figure 5.15: The magnetic dipole absorption lines of the $v = 0 \rightarrow 0$ $X\,^3\Sigma_g^-$–$X\,^3\Sigma_g^-$ transition, with the predicted intensities (top) shown in comparison to known intensities (bottom) from the HITRAN database.

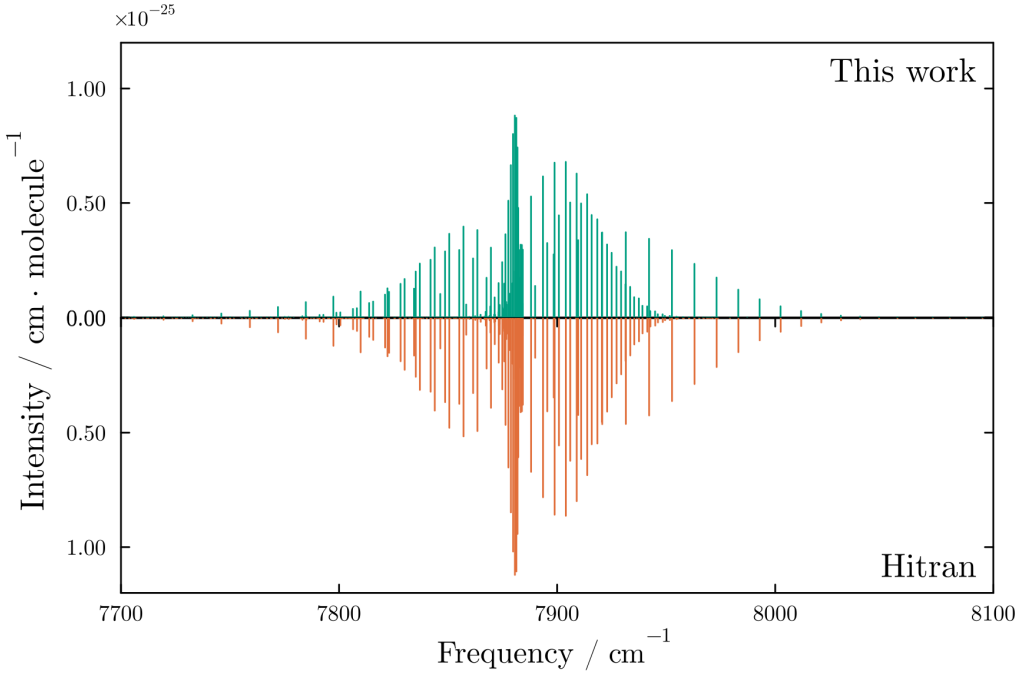

Figure 5.16: The magnetic dipole absorption lines of the $v = 1 \rightarrow 0$ a $^1\Delta_g$– X $^3\Sigma_g^-$ transition, with the predicted intensities (top) shown in comparison to known intensities (bottom) from the HITRAN database.

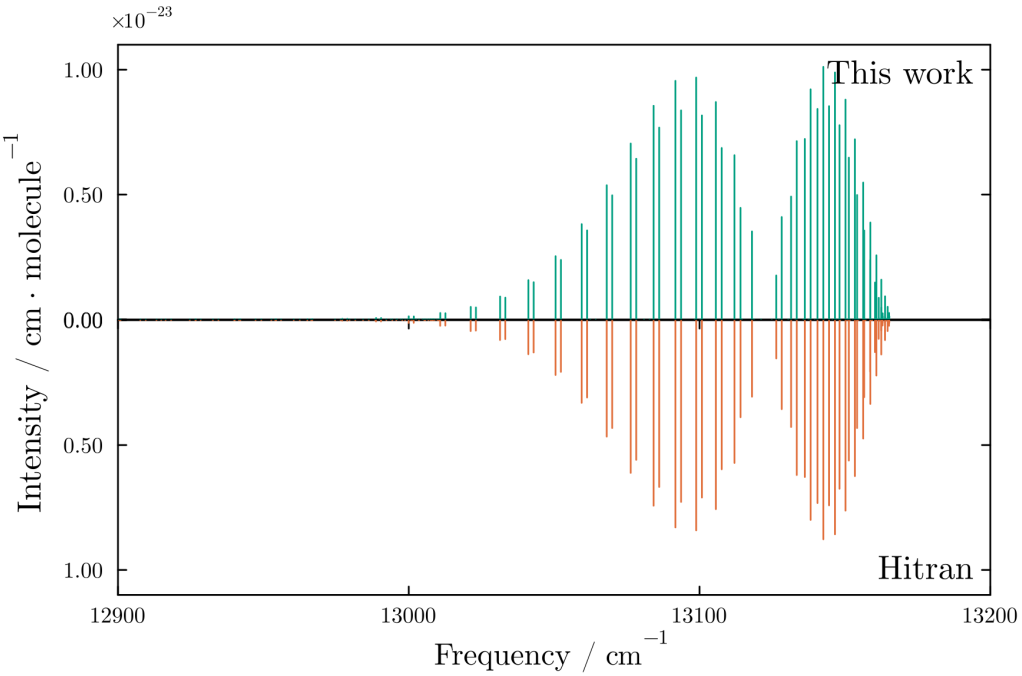

Figure 5.17: The magnetic dipole absorption lines of the $v = 1 \rightarrow 0$ b $^1\Sigma_g^+$– X $^3\Sigma_g^-$ transition, with the predicted intensities (top) shown in comparison to known intensities (bottom) from the HITRAN database.

lend strength to the A-band through spin-orbit of the $b\,^1\Sigma_g^+$ state. Additional weaker contributions come from the EAMCs connecting the $X\,^3\Sigma_g^-$ and $b\,^1\Sigma_g^+$ to the Π states. The EAMCs and SOCs that govern these contributions were not included in the refinement procedure so, similarly to the argument previously for the quadrupole absorption lines, we may expect a greater degree of accuracy with a more energy dataset and empirical refinement of the EAMCs.

5.7.4 Temperature Dependence

I have previously established that one of the primary objectives for producing a spectroscopic model for $^{16}O_2$ is the ability to provide absorption cross-sections for arbitrary temperatures across a wide range of spectral frequencies, a task that is not straightforward to achieve experimentally. The specific temperatures and line profiles that determine the absorption cross-section must be selected on a case-by-case basis according to the relevant application and physical context. However, for completeness in demonstrating the goal of this thesis, I provide in this section a demonstrative cross-section for $^{16}O_2$ in the infrared region.

In Fig. 5.19 I present a temperature dependent absorption cross section using a Lorentzian line profile with a HWHM of $0.1\,\mathrm{cm}^{-1}$ for a range of temperatures between 296–3000 K. Here the cross-sections due to the magnetic dipole and electric quadrupole moments have been summed to accurately predict the total absorption of closely separated lines with finite line width. As temperature increases we observe the usual pattern of increasing intensity for the overtone and hot vibrational bands, accompanied by increasing intensity for transitions to higher rotational levels.

However, of particular interest is the strong temperature dependence of the absorption cross in the region 3×10^3–$7 \times 10^3\,\mathrm{cm}^{-1}$. These transitions form the so-called Noxon band ($b\,^1\Sigma_g^+ - a\,^1\Delta_g$), which becomes the dominant quadrupolar absorption mechanism at temperatures of 1500 K or higher. Indeed, the absorption strength of the fundamental Noxon band $v = 0 \leftarrow 0$, centred around $5 \times 10^3\,\mathrm{cm}^{-1}$ increases by approximately five orders of magnitude between 296 K and 3000 K. This is because the Noxon band arises as a result of a direct quadrupole coupling between the two excited states, and does not rely on spin-orbit coupling to borrow intensity. Thus, as temperature increases, and a a sizeable population of molecules are excited to the $a\,^1\Delta_g$, the strength of this absorption mechanism quickly dominates over the weaker transition quadrupole moments that rely on spin-orbit coupling. This temperature dependence will be an important consideration for retrievals of the class of hot rocky super-Earth planets, which can often experience temperatures well in excess of 1000 K [175–177].

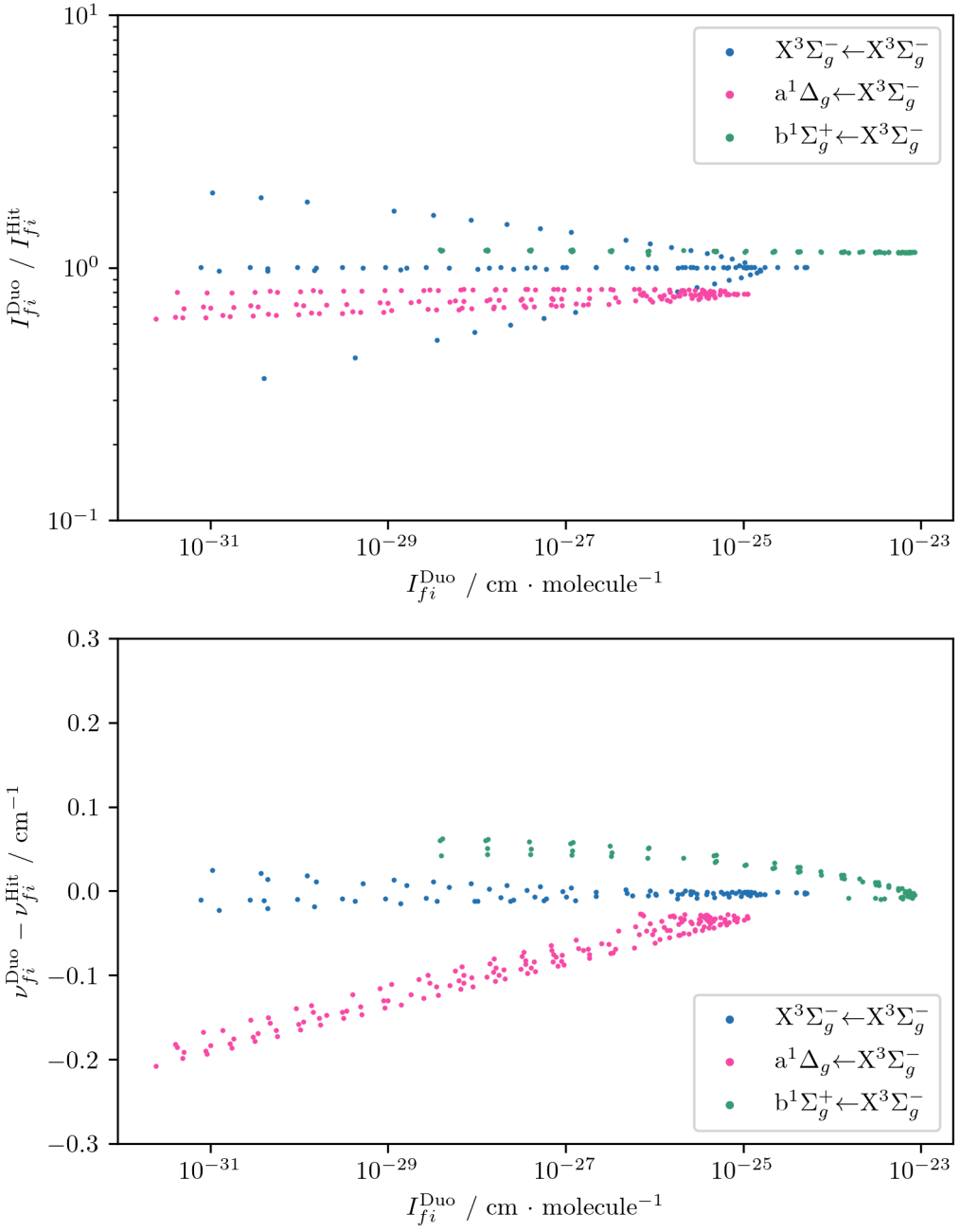

Figure 5.18: Numerical benchmarking of the magnetic dipole transition frequencies (top) and absorption intensities (bottom) predicted by the empirical spectroscopic model across the most intense vibrational bands.

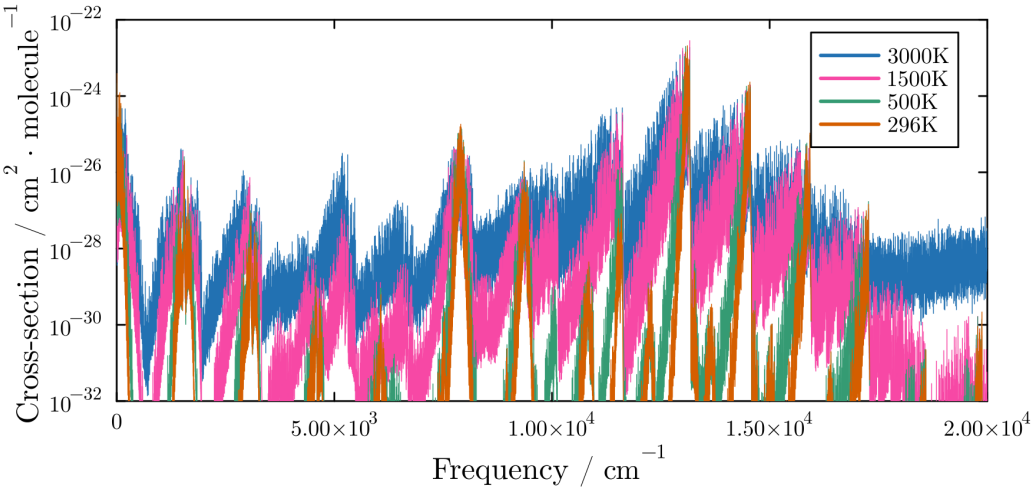

Figure 5.19: The magnetic dipole and electric quadrupole absorption cross section for a range of temperatures between 296–3000 K. The cross section was computed using a representative Lorentzian line profile with a HWHM of 0.1 cm^{-1}.

Chapter 6

Conclusion and Outlook

6.1 Conclusions

The aim of this thesis was primarily to develop a computational methodology for calculating electric quadrupole and magnetic dipole transition probabilities of diatomic molecules. The system and molecule chosen to demonstrate this methodology was molecular oxygen ($^{16}O_2$), specifically the infrared and atmospheric bands composed of transitions between the three lowest-lying electronic states. The objective in this example is a temperature-dependent line list with complete spectral coverage of transitions greater than 1×10^{-30} cm molecule^{-1} in the region 0–2×10^4 cm^{-1}.

Chapter 2 describes a unified treatment of the electric quadrupole and magnetic dipole line strengths and derives expressions for the intensity of these transitions in the basis of Hund's case (a) functions. The calculation of these quantities was implemented and tested in the Duo program. This methodology allows the user to solve the coupled rovibronic Schrödinger equation of a system with any number of PECs and couplings. These properties can calculated *ab initio* using electronic structure programs or obtained through empirical methods, and represented internally with either an analytic form or as a 1D grid of values. The method has been demonstrated not only for the $^{16}O_2$ system presented in this thesis, but also for H_2, CO and HF, the results of which were published in Somogyi et al. [178]. This new methodology presents the scientific community with the most powerful computational tool available for calculating higher order transition intensities of diatomic molecules and will enable the calculation of these transition intensities for other diatomic molecules in the future.

Chapter 3 outlines the internal methodology employed by the Duo program for solving the coupled Schrödinger equation and computing the temperature dependent line list. The procedure for solving the Schrödinger equation has been extensively used in previous ExoMol publications to produce electric

dipole transition probabilities, but this thesis has introduced a novel step in the methodology that was crucial to a successful $^{16}O_2$ line list. Namely, a procedure and associated computer code for transforming to the diabatic representation of the electronic structure properties.

Many diatomic molecules exhibit strong non-adiabatic interactions, where the nuclear motion evolves on more than one electronic state and as a result the PECs exhibit strong avoided crossings. The method of solving the vibrational Schrödinger equation employed by the Duo program is ill-suited to the treatment of quasi-bound PECs which can slow or prevent convergence. By contrast, the sinc-DVR method is known to converge exponentially for smooth PECs. Thus a transformation to the diabatic representation is clearly beneficial in solving the vibrational Schrödinger equation. The code developed for performing this transformation has already yielded novel scientific research an an accurate linelist for the SO molecule by Brady et al. [97, 93, 105].

Chapter 5 represents the major result of this work. The first part of this result is the detailed electronic structure calculations of previously unreported electronic structure properties. These include a number of electric quadrupole and orbital angular momentum curves for seven electronic states of molecular oxygen, as well as the potential energy and spin-orbit coupling curves of those electronic states. These calculations provide the scientific community with new data that may find application across a range of fields such as materials science, molecular dynamics, atmospheric and astrophysical chemistry and biochemistry.

This chapter also provides an empirical spectroscopic model of this molecule, for which the electronic structure properties presented in Sec. 5.3 were empirically refined by fitting analytic representations to accurate state energies from the MARVEL database. This in turn has been used to produce a temperature dependent line list consisting of 375 362 absorption lines of $^{16}O_2$ in the region 0–$2 \times 10^4\,\mathrm{cm}^{-1}$ with sub-percent accuracy in the predicted frequency. This represents an order of magnitude increase in the number of absorption lines over existing databases, with several previously unmeasured vibrational bands. It also provides predictions for the absorption intensities of these transitions across a range of temperatures and has shed light on the temperature dependence of the absorption cross section. As part of this work I have presented a complete account of the various first-order contributions to the intensity of these bands, and shown that the inclusion of highly excited states is crucial to accurately characterising the infrared and visible spectrum of $^{16}O_2$. The predictions made by the empirical model presented in Chapter 5 have been validated by new experimental measurements performed by NIST for the $\mathrm{b}\,^1\Sigma_g^+ - \mathrm{X}\,^3\Sigma_g^-(0,\,0)$ transitions up to $J = 40$. Previous work published during the course of this PhD project has already been applied to atmospheric retrievals, and this new, more complete line list will undoubtedly find utility

in the astrophysics community [179, 1–3].

6.2 Outlook

The work of this thesis has shown that the computational methodology I developed as part of the Duo program can confidently predict absorption intensities for higher order transition moments in diatomic molecules. This has been demonstrated through the production of a line list for the microwave, infrared, and atmospheric absorption bands of $^{16}O_2$.

The line list presented in Chapter 5 using the empirical model obtained in this thesis represents a step change in the spectroscopic data available to the astrophysics community for use in exoplanetary retrievals. It is hoped that investigation into this species will continue and that further refinement of the model will follow.

There are three major avenues that may be explored for subsequent spectroscopic models of these absorption bands. Firstly, the addition of higher order contributions, such as the $^5\Pi_g$ excited states of $^{16}O_2$. Secondly, the inclusion of additional, as yet unavailable, state energy data for the $^1\Pi_g$ and $^3\Pi_g$ states, which would facilitate an empirical model for their PECs and SOCs. Lastly, empirical refinement of the electric quadrupole and magnetic dipole moment curves by fitting to the absorption intensities. This would require substantial additions to the Duo spectroscopic program, but would undoubtedly provide a valuable tool for future spectroscopic studies.

The software contribution of this thesis, which forms a large portion of the work undertaken, will also facilitate similar studies of other diatomic species. Of particular importance are N_2 and H_2. The N_2 molecule plays an important role in characterising Earth-like exoplanets, and has been proposed as a partner molecule to $^{16}O_2$ for detection as a bio-signature [180–182]. Arguments have also been made for H_2 as a biosignature [183], and it's presence plays an important role in characterising a wide array of exoplanets [45, 184]. There are also a number of heteronuclear diatomic molecules, such as CO and HF, that exhibit strong quadrupolar absorption and similar systems would be key target molecules for future investigations of higher order transition moments [178].

Appendix A

Symmetry Groups and Term Symbols

Tables A.1 and A.2 are versions of Tables 3.3 and 3.4 with the addition of Molpro enumerations for the irreducible representations. Which can be used to simplify the conversion of Molpro output data to Duo input.

Symmetry	Function	Molpro No.	Components
A_g	s	1	Σ_g^+, $(\Delta_g)_{xx}$
B_{1g}	xy	4	Σ_g^-, $(\Delta_g)_{xy}$
B_{2g}	xz	6	$(\Pi_g)_x$
B_{3g}	yz	7	$(\Pi_g)_y$
A_u	xyz	8	Σ_u^-, $(\Delta_u)_{xy}$
B_{1u}	z	5	Σ_u^+, $(\Delta_u)_{xx}$
B_{2u}	y	3	$(\Pi_u)_y$
B_{3u}	x	2	$(\Pi_u)_x$

Table A.1: Irreducible representations for homonuclear symmetry groups, the functions that transform according to the irreducible representations, their Molpro enumeration, and corresponding components of electronic states.

Symmetry	Function(s)	Molpro No.	Components
A_1	s, z	1	Σ^+, Δ_{xx}
A_2	xy	4	Σ^-, Δ_{xy}
B_1	x, xz	2	Π_x
B_2	y, yz	3	Π_y

Table A.2: Irreducible representations for heteronuclear symmetry groups, the functions that transform according to the irreducible representations, their Molpro enumeration, and corresponding components of electronic states.

References

[1] Napaporn A-thano, Supachai Awiphan, Ing-Guey Jiang, Eamonn Kerins, Akshay Priyadarshi, Iain McDonald, Yogesh C. Joshi, Thansuda Chulikorn, Joshua J. C. Hayes, Stephen Charles, Chung-Kai Huang, Ronnakrit Rattanamala, Li-Chin Yeh, and Vik S. Dhillon. Revisiting the Transit Timing and Atmosphere Characterization of the Neptune-mass Planet HAT-P-26 b. *The Astronomical Journal*, 166(6):223, 2023. ISSN 1538-3881. doi: 10.3847/1538-3881/acfeea.

[2] Amy J. Louca, Yamila Miguel, and Daria Kubyshkina. Metallicity and Spectral Evolution of WASP 39b: The Limited Role of Hydrodynamic Escape. *The Astrophysical Journal Letters*, 956(1):L19, 2023. ISSN 2041-8205. doi: 10.3847/2041-8213/acfaec.

[3] C. Sandin, L. Mattsson, K. L. Chubb, M. Ergon, and P. M. Weilbacher. Three-component modelling of O-rich AGB star winds: I. Effects of drift using forsterite. *Astronomy & Astrophysics*, 677:A27, 2023. ISSN 0004-6361, 1432-0746. doi: 10.1051/0004-6361/202345841.

[4] D. Truhlar. Vibrational matrix-elements of quadrupole-moment functions of H_2 N_2 and CO. *IJQC*, 6:975–988, 1972. doi: 10.1002/qua.560060515.

[5] Gang Li, Iouli E. Gordon, Laurence S. Rothman, Yan Tan, Shui-Ming Hu, Samir Kassi, Alain Campargue, and Emile S. Medvedev. Rovibrational line lists for nine isotopologues of the CO molecule in the X $^1\Sigma^+$ ground electronic state. *ApJS*, 216:15, 2015. doi: 10.1088/0067-0049/216/1/15.

[6] George Maroulis. Electric multipole moment, dipole and quadrupole (hyper)polarizability derivatives for HF ($X^1\Sigma^+$). *Journal of Molecular Structure: THEOCHEM*, 633(2):177–197, 2003. ISSN 0166-1280. doi: 10.1016/S0166-1280(03)00273-2.

[7] Piotr Piecuch, Anne E. Kondo, Vladimír Špirko, and Josef Paldus. Molecular quadrupole moment functions of HF and N_2. I. Ab initio

linear-response coupled-cluster results. *The Journal of Chemical Physics*, 104(12):4699–4715, 1996. ISSN 0021-9606. doi: 10.1063/1.471164.

[8] John A. Coxon and Photos G. Hajigeorgiou. Improved direct potential fit analyses for the ground electronic states of the hydrogen halides: HF/DF/TF, HCl/DCl/TCl, HBr/DBr/TBr and HI/DI/TI. *Journal of Quantitative Spectroscopy and Radiative Transfer*, 151:133–154, 2015. ISSN 0022-4073. doi: 10.1016/j.jqsrt.2014.08.028.

[9] Tibor Furtenbacher, Mátyás Horváth, Dávid Koller, Panna Sólyom, Anna Balogh, István Balogh, and Attila G. Császár. MARVEL Analysis of the Measured High-Resolution Rovibronic Spectra and Definitive Ideal-Gas Thermochemistry of the $^{16}O_2$ Molecule. *Journal of Physical and Chemical Reference Data*, 48(2):023101, 2019. ISSN 0047-2689, 1529-7845. doi: 10.1063/1.5083135.

[10] Peter J. Mohr, David B. Newell, and Barry N. Taylor. CODATA Recommended Values of the Fundamental Physical Constants: 2014*. *Journal of Physical and Chemical Reference Data*, 45(4):043102, 2016. ISSN 0047-2689. doi: 10.1063/1.4954402.

[11] Sonia Coriani, Asger Halkier, Dan Jonsson, Jürgen Gauss, Antonio Rizzo, and Ove Christiansen. On the electric field gradient induced birefringence and electric quadrupole moment of CO, N_2O, and OCS. *The Journal of Chemical Physics*, 118(16):7329–7339, 2003. ISSN 0021-9606. doi: 10.1063/1.1562198.

[12] Naven Chetty and Vincent W. Couling. Measurement of the electric quadrupole moment of CO. *JCP*, 134:164307, 2011. doi: 10.1063/1.3585605.

[13] Hui Liu, Deheng Shi, Jinfeng Sun, Zunlue Zhu, and Zhang Shulin. Accurate calculations on the 22 electronic states and 54 spin-orbit states of the O_2 molecule: Potential energy curves, spectroscopic parameters and spin-orbit coupling. *Spectrochimica Acta Part A: Molecular and Biomolecular Spectroscopy*, 124:216–229, 2014. ISSN 1386-1425. doi: 10.1016/j.saa.2014.01.003.

[14] B. Ruscic, R.E. Pinzon, M.L. Morton, G. Von Laszevski, S.J. Bittner, S.G. Nijsure, K.A. Amin, M. Minkoff, and A.F. Wagner. Introduction to active thermochemical tables: Several "Key" enthalpies of formation revisited. *Journal of Physical Chemistry A*, 108(45):9979–9997, 2004. ISSN 1089-5639. doi: 10.1021/jp047912y.

[15] K.P. Huber and G. Herzberg. *Molecular Spectra and Molecular Structure. IV. Constants of Diatomic Molecule*, volume 4. Publisher Name Springer, Boston, MA, 1979. doi: 10.1007/978-1-4757-0961-2.

[16] Jonathan Tennyson and Sergei N. Yurchenko. Laboratory spectra of hot molecules: Data needs for hot super-Earth exoplanets. *Molecular Astrophysics*, 8:1–18, 2017. ISSN 2405-6758. doi: 10.1016/j.molap.2017.05.002.

[17] Daniel D. B. Koll, Matej Malik, Megan Mansfield, Eliza M.-R. Kempton, Edwin Kite, Dorian Abbot, and Jacob L. Bean. Identifying Candidate Atmospheres on Rocky M Dwarf Planets via Eclipse Photometry. *The Astrophysical Journal*, 886(2):140, 2019. ISSN 0004-637X. doi: 10.3847/1538-4357/ab4c91.

[18] Robin Wordsworth and Laura Kreidberg. Atmospheres of Rocky Exoplanets. *Annual Review of Astronomy and Astrophysics*, 60(1):159–201, 2022. doi: 10.1146/annurev-astro-052920-125632.

[19] Martin Schlecker, Dániel Apai, Tim Lichtenberg, Galen Bergsten, Arnaud Salvador, and Kevin K. Hardegree-Ullman. Bioverse: The Habitable Zone Inner Edge Discontinuity as an Imprint of Runaway Greenhouse Climates on Exoplanet Demographics. *The Planetary Science Journal*, 5(1):3, 2024. ISSN 2632-3338. doi: 10.3847/PSJ/acf57f.

[20] W. Benz, C. Broeg, A. Fortier, N. Rando, T. Beck, M. Beck, D. Queloz, D. Ehrenreich, P. F. L. Maxted, K. G. Isaak, N. Billot, Y. Alibert, R. Alonso, C. António, J. Asquier, T. Bandy, T. Bárczy, D. Barrado, S. C. C. Barros, W. Baumjohann, A. Bekkelien, M. Bergomi, F. Biondi, X. Bonfils, L. Borsato, A. Brandeker, M.-D. Busch, J. Cabrera, V. Cessa, S. Charnoz, B. Chazelas, A. Collier Cameron, C. Corral Van Damme, D. Cortes, M. B. Davies, M. Deleuil, A. Deline, L. Delrez, O. Demangeon, B. O. Demory, A. Erikson, J. Farinato, L. Fossati, M. Fridlund, D. Futyan, D. Gandolfi, A. Garcia Munoz, M. Gillon, P. Guterman, A. Gutierrez, J. Hasiba, K. Heng, E. Hernandez, S. Hoyer, L. L. Kiss, Z. Kovacs, T. Kuntzer, J. Laskar, A. Lecavelier des Etangs, M. Lendl, A. López, I. Lora, C. Lovis, T. Lüftinger, D. Magrin, L. Malvasio, L. Marafatto, H. Michaelis, D. de Miguel, D. Modrego, M. Munari, V. Nascimbeni, G. Olofsson, H. Ottacher, R. Ottensamer, I. Pagano, R. Palacios, E. Pallé, G. Peter, D. Piazza, G. Piotto, A. Pizarro, D. Pollaco, R. Ragazzoni, F. Ratti, H. Rauer, I. Ribas, M. Rieder, R. Rohlfs, F. Safa, M. Salatti, N. C. Santos, G. Scandariato, D. Ségransan, A. E. Simon, A. M. S. Smith, M. Sordet, S. G. Sousa, M. Steller, G. M. Szabó, J. Szoke, N. Thomas, M. Tschentscher, S. Udry, V. Van Groo-

tel, V. Viotto, I. Walter, N. A. Walton, F. Wildi, and D. Wolter. The CHEOPS mission. *Experimental Astronomy*, 51(1):109–151, 2021. ISSN 1572-9508. doi: 10.1007/s10686-020-09679-4.

[21] Jonathan P. Gardner, John C. Mather, Mark Clampin, Rene Doyon, Matthew A. Greenhouse, Heidi B. Hammel, John B. Hutchings, Peter Jakobsen, Simon J. Lilly, Knox S. Long, Jonathan I. Lunine, Mark J. Mccaughrean, Matt Mountain, John Nella, George H. Rieke, Marcia J. Rieke, Hans-Walter Rix, Eric P. Smith, George Sonneborn, Massimo Stiavelli, H. S. Stockman, Rogier A. Windhorst, and Gillian S. Wright. The James Webb Space Telescope. *Space Science Reviews*, 123(4):485–606, 2006. ISSN 1572-9672. doi: 10.1007/s11214-006-8315-7.

[22] Ian Stotesbury, Billy Edwards, Jean-Francois Lavigne, Vasco Pesquita, James Veilleux, Philip Windred, Ahmed Al-Refaie, Lawrence Bradley, Sushang Ma, Giorgio Savini, Giovanna Tinetti, Til Birnstiel, Sally Dodson-Robinson, Barbara Ercolano, Dax Feliz, Nina Hernitschek, Daniel Holdsworth, Ing-Guey Jiang, Matt Griffin, Nataliea Lowson, Karan Molaverdikhani, Hilding Neilson, Caprice Phillips, Thomas Preibisch, Subhajit Sarkar, Keivan G. Stassun, Derek Ward-Thompson, Duncan Wright, Ming Yang, Li-Chin Yeh, Ji-Lin Zhou, Richard Archer, Yoga Barrathwaj Raman Mohan, Max Joshua, Marcell Tessenyi, Jonathan Tennyson, and Benjamin Wilcock. Twinkle: A small satellite spectroscopy mission for the next phase of exoplanet science. In *Space Telescopes and Instrumentation 2022: Optical, Infrared, and Millimeter Wave*, volume 12180, pages 1117–1130. SPIE, 2022. doi: 10.1117/12.2641373.

[23] H. Rauer, C. Catala, C. Aerts, T. Appourchaux, W. Benz, A. Brandeker, J. Christensen-Dalsgaard, M. Deleuil, L. Gizon, M.-J. Goupil, M. Güdel, E. Janot-Pacheco, M. Mas-Hesse, I. Pagano, G. Piotto, D. Pollacco, Ċ. Santos, A. Smith, J.-C. Suárez, R. Szabó, S. Udry, V. Adibekyan, Y. Alibert, J.-M. Almenara, P. Amaro-Seoane, M. Ammler-von Eiff, M. Asplund, E. Antonello, S. Barnes, F. Baudin, K. Belkacem, M. Bergemann, G. Bihain, A. C. Birch, X. Bonfils, I. Boisse, A. S. Bonomo, F. Borsa, I. M. Brandão, E. Brocato, S. Brun, M. Burleigh, R. Burston, J. Cabrera, S. Cassisi, W. Chaplin, S. Charpinet, C. Chiappini, R. P. Church, Sz. Csizmadia, M. Cunha, M. Damasso, M. B. Davies, H. J. Deeg, R. F. Díaz, S. Dreizler, C. Dreyer, P. Eggenberger, D. Ehrenreich, P. Eigmüller, A. Erikson, R. Farmer, S. Feltzing, F. de Oliveira Fialho, P. Figueira, T. Forveille, M. Fridlund, R. A. García, P. Giommi, G. Giuffrida, M. Godolt, J. Gomes da Silva, T. Granzer, J. L. Grenfell, A. Grotsch-Noels, E. Günther, C. A. Haswell, A. P. Hatzes, G. Hébrard,

S. Hekker, R. Helled, K. Heng, J. M. Jenkins, A. Johansen, M. L. Khodachenko, K. G. Kislyakova, W. Kley, U. Kolb, N. Krivova, F. Kupka, H. Lammer, A. F. Lanza, Y. Lebreton, D. Magrin, P. Marcos-Arenal, P. M. Marrese, J. P. Marques, J. Martins, S. Mathis, S. Mathur, S. Messina, A. Miglio, J. Montalban, M. Montalto, M. J. P. F. G. Monteiro, H. Moradi, E. Moravveji, C. Mordasini, T. Morel, A. Mortier, V. Nascimbeni, R. P. Nelson, M. B. Nielsen, L. Noack, A. J. Norton, A. Ofir, M. Oshagh, R.-M. Ouazzani, P. Pápics, V. C. Parro, P. Petit, B. Plez, E. Poretti, A. Quirrenbach, R. Ragazzoni, G. Raimondo, M. Rainer, D. R. Reese, R. Redmer, S. Reffert, B. Rojas-Ayala, I. W. Roxburgh, S. Salmon, A. Santerne, J. Schneider, J. Schou, S. Schuh, H. Schunker, A. Silva-Valio, R. Silvotti, I. Skillen, I. Snellen, F. Sohl, S. G. Sousa, A. Sozzetti, D. Stello, K. G. Strassmeier, M. Švanda, Gy. M. Szabó, A. Tkachenko, D. Valencia, V. Van Grootel, S. D. Vauclair, P. Ventura, F. W. Wagner, N. A. Walton, J. Weingrill, S. C. Werner, P. J. Wheatley, and K. Zwintz. The PLATO 2.0 mission. *Experimental Astronomy*, 38(1):249–330, 2014. ISSN 1572-9508. doi: 10.1007/s10686-014-9383-4.

[24] Giovanna Tinetti, Paul Eccleston, Carole Haswell, Pierre-Olivier Lagage, Jérémy Leconte, Theresa Lüftinger, Giusi Micela, Michel Min, Göran Pilbratt, Ludovic Puig, Mark Swain, Leonardo Testi, Diego Turrini, Bart Vandenbussche, Maria Rosa Zapatero Osorio, Anna Aret, Jean-Philippe Beaulieu, Lars Buchhave, Martin Ferus, Matt Griffin, Manuel Guedel, Paul Hartogh, Pedro Machado, Giuseppe Malaguti, Enric Pallé, Mirek Rataj, Tom Ray, Ignasi Ribas, Robert Szabó, Jonathan Tan, Stephanie Werner, Francesco Ratti, Carsten Scharmberg, Jean-Christophe Salvignol, Nathalie Boudin, Jean-Philippe Halain, Martin Haag, Pierre-Elie Crouzet, Ralf Kohley, Kate Symonds, Florian Renk, Andrew Caldwell, Manuel Abreu, Gustavo Alonso, Jerome Amiaux, Michel Berthé, Georgia Bishop, Neil Bowles, Manuel Carmona, Deirdre Coffey, Josep Colomé, Martin Crook, Lucile Désjonqueres, José J. Díaz, Rachel Drummond, Mauro Focardi, Jose M. Gómez, Warren Holmes, Matthijs Krijger, Zsolt Kovacs, Tom Hunt, Richardo Machado, Gianluca Morgante, Marc Ollivier, Roland Ottensamer, Emanuele Pace, Teresa Pagano, Enzo Pascale, Chris Pearson, Søren Møller Pedersen, Moshe Pniel, Stéphane Roose, Giorgio Savini, Richard Stamper, Peter Szirovicza, Janos Szoke, Ian Tosh, Francesc Vilardell, Joanna Barstow, Luca Borsato, Sarah Casewell, Quentin Changeat, Benjamin Charnay, Svatopluk Civiš, Vincent Coudé du Foresto, Athena Coustenis, Nicolas Cowan, Camilla Danielski, Olivier Demangeon, Pierre Drossart, Billy N. Edwards, Gabriella Gilli, Therese Encrenaz, Csaba Kiss, Anastasia Kokori, Masahiro Ikoma, Juan Carlos Morales, João Mendonça, Andrea Moneti,

Lorenzo Mugnai, Antonio García Muñoz, Ravit Helled, Mihkel Kama, Yamila Miguel, Nikos Nikolaou, Isabella Pagano, Olja Panic, Miriam Rengel, Hans Rickman, Marco Rocchetto, Subhajit Sarkar, Franck Selsis, Jonathan Tennyson, Angelos Tsiaras, Olivia Venot, Krisztián Vida, Ingo P. Waldmann, Sergey Yurchenko, Gyula Szabó, Rob Zellem, Ahmed Al-Refaie, Javier Perez Alvarez, Lara Anisman, Axel Arhancet, Jaume Ateca, Robin Baeyens, John R. Barnes, Taylor Bell, Serena Benatti, Katia Biazzo, Maria Błęcka, Aldo Stefano Bonomo, José Bosch, Diego Bossini, Jeremy Bourgalais, Daniele Brienza, Anna Brucalassi, Giovanni Bruno, Hamish Caines, Simon Calcutt, Tiago Campante, Rodolfo Canestrari, Nick Cann, Giada Casali, Albert Casas, Giuseppe Cassone, Christophe Cara, Manuel Carmona, Ludmila Carone, Nathalie Carrasco, Quentin Changeat, Paolo Chioetto, Fausto Cortecchia, Markus Czupalla, Katy L. Chubb, Angela Ciaravella, Antonio Claret, Riccardo Claudi, Claudio Codella, Maya Garcia Comas, Gianluca Cracchiolo, Patricio Cubillos, Vania Da Peppo, Leen Decin, Clemence Dejabrun, Elisa Delgado-Mena, Anna Di Giorgio, Emiliano Diolaiti, Caroline Dorn, Vanessa Doublier, Eric Doumayrou, Georgina Dransfield, Luc Dumaye, Emma Dunford, Antonio Jimenez Escobar, Vincent Van Eylen, Maria Farina, Davide Fedele, Alejandro Fernández, Benjamin Fleury, Sergio Fonte, Jean Fontignie, Luca Fossati, Bernd Funke, Camille Galy, Zoltán Garai, Andrés García, Alberto García-Rigo, Antonio Garufi, Giuseppe Germano Sacco, Paolo Giacobbe, Alejandro Gómez, Arturo Gonzalez, Francisco Gonzalez-Galindo, Davide Grassi, Caitlin Griffith, Mario Giuseppe Guarcello, Audrey Goujon, Amélie Gressier, Aleksandra Grzegorczyk, Tristan Guillot, Gloria Guilluy, Peter Hargrave, Marie-Laure Hellin, Enrique Herrero, Matt Hills, Benoit Horeau, Yuichi Ito, Niels Christian Jessen, Petr Kabath, Szilárd Kálmán, Yui Kawashima, Tadahiro Kimura, Antonín Knížek, Laura Kreidberg, Ronald Kruid, Diederik J. M. Kruijssen, Petr Kubelík, Luisa Lara, Sebastien Lebonnois, David Lee, Maxence Lefevre, Tim Lichtenberg, Daniele Locci, Matteo Lombini, Alejandro Sanchez Lopez, Andrea Lorenzani, Ryan MacDonald, Laura Magrini, Jesus Maldonado, Emmanuel Marcq, Alessandra Migliorini, Darius Modirrousta-Galian, Karan Molaverdikhani, Sergio Molinari, Paul Mollière, Vincent Moreau, Giuseppe Morello, Gilles Morinaud, Mario Morvan, Julianne I. Moses, Salima Mouzali, Nariman Nakhjiri, Luca Naponiello, Norio Narita, Valerio Nascimbeni, Athanasia Nikolaou, Vladimiro Noce, Fabrizio Oliva, Pietro Palladino, Andreas Papageorgiou, Vivien Parmentier, Giovanni Peres, Javier Pérez, Santiago Perez-Hoyos, Manuel Perger, Cesare Cecchi Pestellini, Antonino Petralia, Anne Philippon, Arianna Piccialli, Marco Pignatari, Giampaolo Piotto, Linda Podio, Gianluca Polenta, Giampaolo Preti, Theodor Pribulla,

Manuel Lopez Puertas, Monica Rainer, Jean-Michel Reess, Paul Rimmer, Séverine Robert, Albert Rosich, Loic Rossi, Duncan Rust, Ayman Saleh, Nicoletta Sanna, Eugenio Schisano, Laura Schreiber, Victor Schwartz, Antonio Scippa, Bálint Seli, Sho Shibata, Caroline Simpson, Oliver Shorttle, N. Skaf, Konrad Skup, Mateusz Sobiecki, Sergio Sousa, Alessandro Sozzetti, Judit Šponer, Lukas Steiger, Paolo Tanga, Paul Tackley, Jake Taylor, Matthias Tecza, Luca Terenzi, Pascal Tremblin, Andrea Tozzi, Amaury Triaud, Loïc Trompet, Shang-Min Tsai, Maria Tsantaki, Diana Valencia, Ann Carine Vandaele, Mathieu Van der Swaelmen, Adibekyan Vardan, Gautam Vasisht, Allona Vazan, Ciro Del Vecchio, Dave Waltham, Piotr Wawer, Thomas Widemann, Paulina Wolkenberg, Gordon Hou Yip, Yuk Yung, Mantas Zilinskas, Tiziano Zingales, and Paola Zuppella. Ariel: Enabling planetary science across light-years, 2021.

[25] Jonathan Tennyson, Sergei N. Yurchenko, Ahmed F. Al-Refaie, Victoria H. J. Clark, Katy L. Chubb, Eamon K. Conway, Akhil Dewan, Maire N. Gorman, Christian Hill, A. E. Lynas-Gray, Thomas Mellor, Laura K. McKemmish, Alec Owens, Oleg L. Polyansky, Mikhail Semenov, Wilfrid Somogyi, Giovanna Tinetti, Apoorva Upadhyay, Ingo Waldmann, Yixin Wang, Samuel Wright, and Olga P. Yurchenko. The 2020 release of the ExoMol database: Molecular line lists for exoplanet and other hot atmospheres. *Journal of Quantitative Spectroscopy and Radiative Transfer*, 255:107228, 2020. ISSN 0022-4073. doi: 10.1016/j.jqsrt.2020.107228.

[26] Edwin S. Kite and Laura Schaefer. Water on Hot Rocky Exoplanets. *The Astrophysical Journal Letters*, 909(2):L22, 2021. ISSN 2041-8205. doi: 10.3847/2041-8213/abe7dc.

[27] Edward W. Schwieterman, Nancy Y. Kiang, Mary N. Parenteau, Chester E. Harman, Shiladitya DasSarma, Theresa M. Fisher, Giada N. Arney, Hilairy E. Hartnett, Christopher T. Reinhard, Stephanie L. Olson, Victoria S. Meadows, Charles S. Cockell, Sara I. Walker, John Lee Grenfell, Siddharth Hegde, Sarah Rugheimer, Renyu Hu, and Timothy W. Lyons. Exoplanet Biosignatures: A Review of Remotely Detectable Signs of Life. *Astrobiology*, 18(6):663–708, 2018. ISSN 1531-1074. doi: 10.1089/ast.2017.1729.

[28] Victoria S. Meadows, Christopher T. Reinhard, Giada N. Arney, Mary N. Parenteau, Edward W. Schwieterman, Shawn D. Domagal-Goldman, Andrew P. Lincowski, Karl R. Stapelfeldt, Heike Rauer, Shiladitya DasSarma, Siddharth Hegde, Norio Narita, Russell Deitrick, Jacob Lustig-Yaeger, Timothy W. Lyons, Nicholas Siegler, and J. Lee Grenfell. Exoplanet Biosignatures: Understanding Oxygen as a Biosignature in the

Context of Its Environment. *Astrobiology*, 18(6):630–662, 2018. ISSN 1531-1074. doi: 10.1089/ast.2017.1727.

[29] Renyu Hu, Luke Peterson, and Eric T. Wolf. O_2- and CO-rich Atmospheres for Potentially Habitable Environments on TRAPPIST-1 Planets. *The Astrophysical Journal*, 888(2):122, 2020. ISSN 0004-637X. doi: 10.3847/1538-4357/ab5f07.

[30] Robin Wordsworth and Raymond Pierrehumbert. Abiotic Oxygen-dominated Atmospheres on Terrestrial Habitable Zone Planets. *The Astrophysical Journal*, 785:L20, 2014. ISSN 0004-637X. doi: 10.1088/2041-8205/785/2/L20.

[31] Feng Tian, Kevin France, Jeffrey L. Linsky, Pablo J. D. Mauas, and Mariela C. Vieytes. High stellar FUV/NUV ratio and oxygen contents in the atmospheres of potentially habitable planets. *Earth and Planetary Science Letters*, 385:22–27, 2014. ISSN 0012-821X. doi: 10.1016/j.epsl.2013.10.024.

[32] Shawn D. Domagal-Goldman, Antígona Segura, Mark W. Claire, Tyler D. Robinson, and Victoria S. Meadows. Abiotic ozone and oxygen in atmospheres similar to prebiotic earth. *The Astrophysical Journal*, 792(2):90, 2014. ISSN 0004-637X. doi: 10.1088/0004-637X/792/2/90.

[33] C. E. Harman, E. W. Schwieterman, J. C. Schottelkotte, and J. F. Kasting. ABIOTIC O_2 LEVELS ON PLANETS AROUND F, G, K, AND M STARS: POSSIBLE FALSE POSITIVES FOR LIFE? *The Astrophysical Journal*, 812(2):137, 2015. ISSN 0004-637X. doi: 10.1088/0004-637X/812/2/137.

[34] R. Luger and R. Barnes. Extreme Water Loss and Abiotic O_2Buildup on Planets Throughout the Habitable Zones of M Dwarfs. *Astrobiology*, 15:119–143, 2015. ISSN 1531-1074. doi: 10.1089/ast.2014.1231.

[35] C. E. Harman, R. Felton, R. Hu, S. D. Domagal-Goldman, A. Segura, F. Tian, and J. F. Kasting. Abiotic O_2 Levels on Planets around F, G, K, and M Stars: Effects of Lightning-produced Catalysts in Eliminating Oxygen False Positives. *The Astrophysical Journal*, 866(1):56, 2018. ISSN 0004-637X. doi: 10.3847/1538-4357/aadd9b.

[36] Carey M. Lisse, Steven J. Desch, Cayman T. Unterborn, Stephen R. Kane, Patrick R. Young, Hilairy E. Hartnett, Natalie R. Hinkel, Sang-Heon Shim, Eric E. Mamajek, and Noam R. Izenberg. A Geologically Robust Procedure for Observing Rocky Exoplanets to Ensure that Detection of Atmospheric Oxygen Is a Modern Earth-like Biosignature. *The*

Astrophysical Journal Letters, 898(1):L17, 2020. ISSN 2041-8205. doi: 10.3847/2041-8213/ab9b91.

[37] Joshua Krissansen-Totton, Jonathan J. Fortney, Francis Nimmo, and Nicholas Wogan. Oxygen False Positives on Habitable Zone Planets Around Sun-Like Stars. *AGU Advances*, 2(2):e2020AV000294, 2021. ISSN 2576-604X. doi: 10.1029/2020AV000294.

[38] Joshua Krissansen-Totton, Maggie Thompson, Max L. Galloway, and Jonathan J. Fortney. Understanding planetary context to enable life detection on exoplanets and test the Copernican principle. *Nature Astronomy*, 6(2):189–198, 2022. ISSN 2397-3366. doi: 10.1038/s41550-021-01579-7.

[39] Tim Lichtenberg, Dan J. Bower, Mark Hammond, Ryan Boukrouche, Patrick Sanan, Shang-Min Tsai, and Raymond T. Pierrehumbert. Vertically Resolved Magma Ocean–Protoatmosphere Evolution: H_2, H_2O, CO_2, CH_4, CO, O_2, and N_2 as Primary Absorbers. *Journal of Geophysical Research: Planets*, 126(2):e2020JE006711, 2021. ISSN 2169-9100. doi: 10.1029/2020JE006711.

[40] Yanhao Lin, Wim van Westrenen, and Ho-Kwang Mao. Oxygen controls on magmatism in rocky exoplanets. *Proceedings of the National Academy of Sciences of the United States of America*, 118(45):e2110427118, 2021. ISSN 1091-6490. doi: 10.1073/pnas.2110427118.

[41] Hilke E. Schlichting and Edward D. Young. Chemical Equilibrium between Cores, Mantles, and Atmospheres of Super-Earths and Sub-Neptunes and Implications for Their Compositions, Interiors, and Evolution. *The Planetary Science Journal*, 3(5):127, 2022. ISSN 2632-3338. doi: 10.3847/PSJ/ac68e6.

[42] Laura Schaefer and Bruce Fegley. Redox States of Initial Atmospheres Outgassed on Rocky Planets and Planetesimals. *The Astrophysical Journal*, 843(2):120, 2017. ISSN 0004-637X. doi: 10.3847/1538-4357/aa784f.

[43] Alexandra E. Doyle, Edward D. Young, Beth Klein, Ben Zuckerman, and Hilke E. Schlichting. Oxygen fugacities of extrasolar rocks: Evidence for an Earth-like geochemistry of exoplanets. *Science (New York, N.Y.)*, 366 (6463):356–359, 2019. ISSN 1095-9203. doi: 10.1126/science.aax3901.

[44] Jonathan P. Itcovitz, Auriol S. P. Rae, Robert I. Citron, Sarah T. Stewart, Catriona A. Sinclair, Paul B. Rimmer, and Oliver Shorttle. Reduced Atmospheres of Post-impact Worlds: The Early Earth. *The Planetary Science Journal*, 3(5):115, 2022. ISSN 2632-3338. doi: 10.3847/PSJ/ac67a9.

[45] Philippa Liggins, Sean Jordan, Paul B. Rimmer, and Oliver Shorttle. Growth and Evolution of Secondary Volcanic Atmospheres: I. Identifying the Geological Character of Hot Rocky Planets. *JOURNAL OF GEOPHYSICAL RESEARCH-PLANETS*, 127(7):e2021JE007123, 2022. ISSN 2169-9097, 2169-9100. doi: 10.1029/2021JE007123.

[46] Mercedes López-Morales, Sagi Ben-Ami, Gonzalo Gonzalez-Abad, Juliana García-Mejía, Jeremy Dietrich, and Andrew Szentgyorgyi. Optimizing Ground-based Observations of O_2 in Earth Analogs. *The Astronomical Journal*, 158(1):24, 2019. ISSN 1538-3881. doi: 10.3847/1538-3881/ab21d7.

[47] Z. Lin and L. Kaltenegger. High-resolution reflection spectra for Proxima b and Trappist-1e models for ELT observations. *MONTHLY NOTICES OF THE ROYAL ASTRONOMICAL SOCIETY*, 491(2):2845–2854, 2020. ISSN 0035-8711, 1365-2966. doi: 10.1093/mnras/stz3213.

[48] Kevin K. Hardegree-Ullman, Dániel Apai, Galen J. Bergsten, Ilaria Pascucci, and Mercedes López-Morales. Bioverse: A Comprehensive Assessment of the Capabilities of Extremely Large Telescopes to Probe Earth-like O_2 Levels in Nearby Transiting Habitable-zone Exoplanets. *The Astronomical Journal*, 165(6):267, 2023. ISSN 1538-3881. doi: 10.3847/1538-3881/acd1ec.

[49] P. E. Sheese, E. J. Llewellyn, R. L. Gattinger, A. E. Bourassa, D. A. Degenstein, N. D. Lloyd, and I. C. McDade. Temperatures in the upper mesosphere and lower thermosphere from OSIRIS observations of O_2 A-band emission spectra. *Canadian Journal of Physics*, 88(12):919–925, 2010. ISSN 0008-4204. doi: 10.1139/p10-093.

[50] P. E. Sheese, E. J. Llewellyn, R. L. Gattinger, A. E. Bourassa, D. A. Degenstein, N. D. Lloyd, and I. C. McDade. Mesopause temperatures during the polar mesospheric cloud season. *Geophysical Research Letters*, 38(11), 2011. ISSN 1944-8007. doi: 10.1029/2011GL047437.

[51] P. E. Sheese, I. C. McDade, R. L. Gattinger, and E. J. Llewellyn. Atomic oxygen densities retrieved from Optical Spectrograph and Infrared Imaging System observations of O_2 A-band airglow emission in the mesosphere and lower thermosphere. *Journal of Geophysical Research: Atmospheres*, 116(D1), 2011. ISSN 2156-2202. doi: 10.1029/2010JD014640.

[52] Andrew B. Christensen, Jeng-Hwa Yee, Rebecca L. Bishop, Scott A. Budzien, James H. Hecht, Gulamabas Sivjee, and Andrew W. Stephan. Observations of molecular oxygen Atmospheric band emission in the thermosphere using the near infrared spectrometer on the ISS/RAIDS

experiment. *Journal of Geophysical Research: Space Physics*, 117(A4), 2012. ISSN 2156-2202. doi: 10.1029/2011JA016838.

[53] Kang Sun, Iouli E. Gordon, Christopher E. Sioris, Xiong Liu, Kelly Chance, and Steven C. Wofsy. Reevaluating the Use of O_2 $a^1\Delta$ Band in Spaceborne Remote Sensing of Greenhouse Gases. *Geophysical Research Letters*, 45(11):5779–5787, 2018. ISSN 1944-8007. doi: 10.1029/2018GL077823.

[54] Jean-Loup Bertaux, Alain Hauchecorne, Franck Lefèvre, François-Marie Bréon, Laurent Blanot, Denis Jouglet, Pierre Lafrique, and Pavel Akaev. The use of the 1.27µm O_2 absorption band for greenhouse gas monitoring from space and application to MicroCarb. *Atmospheric Measurement Techniques*, 13(6):3329–3374, 2020. ISSN 1867-1381. doi: 10.5194/amt-13-3329-2020.

[55] A. F. Al-Refaie, Q. Changeat, I. P. Waldmann, and G. Tinetti. TauREx 3: A Fast, Dynamic, and Extendable Framework for Retrievals. *The Astrophysical Journal*, 917(1):37, 2021. ISSN 0004-637X. doi: 10.3847/1538-4357/ac0252.

[56] James W. Brault. Detection of electric quadrupole transitions in the oxygen A band at 7600 Å. *Journal of Molecular Spectroscopy*, 80(2):384–387, 1980. ISSN 0022-2852. doi: 10.1016/0022-2852(80)90149-6.

[57] L. S. Rothman and A. Goldman. Infrared electric quadrupole transitions of atmospheric oxygen. *Applied Optics*, 20(13):2182–2184, 1981. ISSN 2155-3165. doi: 10.1364/AO.20.002182.

[58] Iouli E. Gordon, Samir Kassi, Alain Campargue, and Geoffrey C. Toon. First identification of the $a^1\Delta_g$–$X^3\Sigma_g^-$ electric quadrupole transitions of oxygen in solar and laboratory spectra. *Journal of Quantitative Spectroscopy and Radiative Transfer*, 111(9):1174–1183, 2010. ISSN 0022-4073. doi: 10.1016/j.jqsrt.2010.01.008.

[59] Billy Edwards, Lorenzo Mugnai, Giovanna Tinetti, Enzo Pascale, and Subhajit Sarkar. An Updated Study of Potential Targets for Ariel. *The Astronomical Journal*, 157(6):242, 2019. ISSN 1538-3881. doi: 10.3847/1538-3881/ab1cb9.

[60] A. Goldman, C. P. Rinsland, B. Canova, R. Zander, and M. Dang-Nhu. Improved spectral parameters for the $^{16}O_2$ infrared forbidden lines in the $X^3\sum_g^-$ (0–1) band. *Journal of Quantitative Spectroscopy and Radiative Transfer*, 54(5):757–765, 1995. ISSN 0022-4073. doi: 10.1016/0022-4073(95)00114-Z.

[61] Hans-Joachim Werner, Peter J. Knowles, Frederick R. Manby, Joshua A. Black, Klaus Doll, Andreas Heßelmann, Daniel Kats, Andreas Köhn, Tatiana Korona, David A. Kreplin, Qianli Ma, Thomas F. Miller, III, Alexander Mitrushchenkov, Kirk A. Peterson, Iakov Polyak, Guntram Rauhut, and Marat Sibaev. The Molpro quantum chemistry package. *The Journal of Chemical Physics*, 152(14):144107, 2020. ISSN 0021-9606. doi: 10.1063/5.0005081.

[62] M. J. Frisch, G. W. Trucks, H. B. Schlegel, G. E. Scuseria, M. A. Robb, J. R. Cheeseman, G. Scalmani, V. Barone, G. A. Petersson, H. Nakatsuji, X. Li, M. Caricato, A. V. Marenich, J. Bloino, B. G. Janesko, R. Gomperts, B. Mennucci, H. P. Hratchian, J. V. Ortiz, A. F. Izmaylov, J. L. Sonnenberg, D. Williams-Young, F. Ding, F. Lipparini, F. Egidi, J. Goings, B. Peng, A. Petrone, T. Henderson, D. Ranasinghe, V. G. Zakrzewski, J. Gao, N. Rega, G. Zheng, W. Liang, M. Hada, M. Ehara, K. Toyota, R. Fukuda, J. Hasegawa, M. Ishida, T. Nakajima, Y. Honda, O. Kitao, H. Nakai, T. Vreven, K. Throssell, J. A. Montgomery, Jr., J. E. Peralta, F. Ogliaro, M. J. Bearpark, J. J. Heyd, E. N. Brothers, K. N. Kudin, V. N. Staroverov, T. A. Keith, R. Kobayashi, J. Normand, K. Raghavachari, A. P. Rendell, J. C. Burant, S. S. Iyengar, J. Tomasi, M. Cossi, J. M. Millam, M. Klene, C. Adamo, R. Cammi, J. W. Ochterski, R. L. Martin, K. Morokuma, O. Farkas, J. B. Foresman, and D. J. Fox. Gaussian 16, 2016.

[63] J.F. Stanton, J. Gauss, M.E. Harding, and et al. CFOUR, 2019.

[64] Sergei N. Yurchenko, Lorenzo Lodi, Jonathan Tennyson, and Andrey V. Stolyarov. Duo: A general program for calculating spectra of diatomic molecules. *Computer Physics Communications*, 202:262–275, 2016. ISSN 0010-4655. doi: 10.1016/j.cpc.2015.12.021.

[65] Alain Campargue, Samir Kassi, Andrey Yachmenev, Aleksandra A. Kyuberis, Jochen Küpper, and Sergei N. Yurchenko. Observation of electric-quadrupole infrared transitions in water vapor. *Physical Review Research*, 2:023091, 2020. doi: 10.1103/PhysRevResearch.2.023091.

[66] Alain Campargue, Alexander M. Solodov, Alexander A. Solodov, Andrey Yachmenev, and Sergei N. Yurchenko. Detection of electric-quadrupole transitions in water vapour near 5.4 and 2.5 *mu*m. *Physical Chemistry Chemical Physics*, 22(22):12476–12481, 2020. ISSN 1463-9084. doi: 10.1039/D0CP01667E.

[67] A. Goldman, J. Reid, and L. S. Rothman. Identification of electric quadrupole O_2 and N_2 lines in the infrared atmospheric absorp-

tion spectrum due to the vibration-rotation fundamentals. *Geophysical Research Letters*, 8(1):77–78, 1981. ISSN 1944-8007. doi: 10.1029/GL008i001p00077.

[68] R. J. Glinski, J. A. Nuth, M. D. Reese, and M. L. Sitko. Observation of the spin-forbidden cameron bands of CO in the ultraviolet emission spectrum of the red rectangle. *The Astrophysical Journal Letters*, 467: L109–L112, 1996. doi: 10.1086/310205.

[69] J. Domysławska, S. Wójtewicz, P. Masłowski, A. Cygan, K. Bielska, R. S. Trawiński, R. Ciuryło, and D. Lisak. A new approach to spectral line shapes of the weak oxygen transitions for atmospheric applications. *Journal of Quantitative Spectroscopy and Radiative Transfer*, 169: 111–121, 2016. doi: 10.1016/j.jqsrt.2015.10.019.

[70] Brian Harold Bransden and Charles Jean Joachain. *Physics of Atoms and Molecules*. Pearson Education India, 2003.

[71] Nanna Holmgaard List, Joanna Kauczor, Trond Saue, Hans Jørgen Aagaard Jensen, and Patrick Norman. Beyond the electric-dipole approximation: A formulation and implementation of molecular response theory for the description of absorption of electromagnetic field radiation. *The Journal of Chemical Physics*, 142(24):244111, 2015. ISSN 0021-9606, 1089-7690. doi: 10.1063/1.4922697.

[72] Daniil N. Chistikov. Magnetic dipole and quadrupole transitions in the $N_2 + N_3$ vibrational band of carbon dioxide. *The Journal of Chemical Physics*, 158(13):134307, 2023. ISSN 0021-9606. doi: 10.1063/5.0144201.

[73] Ad Buckingham. Molecular Quadrupole Moments. *Quarterly Reviews*, 13(3):183–214, 1959. doi: 10.1039/qr9591300183.

[74] Hans-Joachim Werner, Peter J. Knowles, Gerald Knizia, Frederick R. Manby, and Martin Schütz. Molpro: A general-purpose quantum chemistry program package. *WIREs Computational Molecular Science*, 2(2): 242–253, 2012. ISSN 1759-0884. doi: 10.1002/wcms.82.

[75] Richard Zare. *Angular Momentum: Understanding Spatial Aspects in Chemistry and Physics*. Wiley, New York ; Chichester, 1988. ISBN 978-0-471-85892-8.

[76] D. A. Long. *The Raman Effect: A Unified Treatment of the Theory of Raman Scattering by Molecules*. Wiley, Chichester ; New York, 2002. ISBN 978-0-471-49028-9.

[77] Hajime Katô. Energy Levels and Line Intensities of Diatomic Molecules. Application to Alkali Metal Molecules. *Bulletin of the Chemical Society of Japan*, 66(11):3203–3234, 1993. ISSN 0009-2673. doi: 10.1246/bcsj.66.3203.

[78] Philip R. Bunker and Per Jensen. *Molecular Symmetry and Spectroscopy, Second Edition*. NRC Research Press, Ottawa, Canada, 2006. ISBN 0-660-17519-3.

[79] R. Guardiola and J. Ros. On the numerical integration of the Schrödinger equation in the finite-difference schemes. *Journal of Computational Physics*, 45(3):374–389, 1982. ISSN 0021-9991. doi: 10.1016/0021-9991(82)90110-3.

[80] R. Guardiola and J. Ros. On the numerical integration of the Schrödinger equation: Numerical tests. *Journal of Computational Physics*, 45(3):390–402, 1982. ISSN 0021-9991. doi: 10.1016/0021-9991(82)90111-5.

[81] John R. Lund and Bruce V. Riley. A Sine-Collocation Method for the Computation of the Eigenvalues of the Radial Schrödinger Equation. *IMA Journal of Numerical Analysis*, 4(1):83–98, 1984. ISSN 0272-4979. doi: 10.1093/imanum/4.1.83.

[82] Daniel T. Colbert and William H. Miller. A novel discrete variable representation for quantum mechanical reactive scattering via the S-matrix Kohn method. *The Journal of Chemical Physics*, 96(3):1982–1991, 1992. ISSN 0021-9606. doi: 10.1063/1.462100.

[83] Reza Islampour and Mahsasadat Miralinaghi. An extensive study of transformation of the diatomics Hamiltonian operator from laboratory- to body-fixed frame. *International Journal of Quantum Chemistry*, 115(8):510–522, 2015. ISSN 1097-461X. doi: 10.1002/qua.24881.

[84] Alan Corney. Atomic and laser spectroscopy. In *Atomic and Laser Spectroscopy*, Oxford Classic Texts in the Physical Sciences. Oxford University Press, Oxford, 2006. ISBN 978-0-19-921145-6.

[85] Alec Owens and Andrey Yachmenev. RichMol: A general variational approach for rovibrational molecular dynamics in external electric fields. *JCP*, 148(12):124102, 2018.

[86] Andrey Yachmenev, Linda V. Thesing, and Jochen Küpper. Laser-induced dynamics of molecules with strong nuclear quadrupole coupling. *JCP*, 151(24):244118, 2019. doi: 10.1063/1.5133837.

[87] P. R. Bunker. The electronic isotope shift in diatomic molecules and the partial breakdown of the Born-Oppenheimer approximation. *Journal of Molecular Spectroscopy*, 28(4):422–443, 1968. ISSN 0022-2852. doi: 10.1016/0022-2852(68)90176-8.

[88] Russell T Pack and Joseph O. Hirschfelder. Separation of Rotational Coordinates from the N-Electron Diatomic Schrödinger Equation. *The Journal of Chemical Physics*, 49(9):4009–4020, 2003. ISSN 0021-9606. doi: 10.1063/1.1670711.

[89] Brian T. Sutcliffe. The separation of electronic and nuclear motion in the diatomic molecule. *Theoretical Chemistry Accounts*, 118(3):563–571, 2007. ISSN 1432-2234. doi: 10.1007/s00214-007-0357-8.

[90] Reza Islampour and Mahsasadat Miralinaghi. An extensive study of transformation of the diatomics Hamiltonian operator from laboratory- to body-fixed frame. *International Journal of Quantum Chemistry*, 115 (8):510–522, 2015. ISSN 1097-461X. doi: 10.1002/qua.24881.

[91] Martin P. Bircher, Elisa Liberatore, Nicholas J. Browning, Sebastian Brickel, Cornelia Hofmann, Aurélien Patoz, Oliver T. Unke, Tomáš Zimmermann, Majed Chergui, Peter Hamm, Ursula Keller, Markus Meuwly, Hans-Jakob Woerner, Jiří Vaníček, and Ursula Rothlisberger. Nonadiabatic effects in electronic and nuclear dynamics. *Structural Dynamics*, 4 (6):061510, 2018. ISSN 2329-7778. doi: 10.1063/1.4996816.

[92] Michael Baer. *Beyond Born-Oppenheimer: Electronic Nonadiabatic Coupling Terms and Conical Intersections*. Wiley, Newark, 1 edition, 2006. ISBN 978-0-471-78007-6. doi: 10.1002/0471780081.

[93] Ryan P. Brady, Charlie Drury, Sergei N. Yurchenko, and Jonathan Tennyson. Numerical Equivalence of Diabatic and Adiabatic Representations in Diatomic Molecules. *Journal of Chemical Theory and Computation*, 2024. ISSN 1549-9618. doi: 10.1021/acs.jctc.3c01150.

[94] Wolfgang Domcke, David R. Yarkony, and Horst Köppel. *Conical Intersections: Theory, Computation and Experiment*. World Scientific, 2011. ISBN 978-981-4313-45-2.

[95] M. Guitou, A. Spielfiedel, and N. Feautrier. Accurate potential energy functions and non-adiabatic couplings in the Mg^+H system. *Chemical Physics Letters*, 488(4):145–152, 2010. ISSN 0009-2614. doi: 10.1016/j.cplett.2010.02.031.

[96] Guiying Liang, Xiaoting Liu, Xiaomei Zhang, Haifeng Xu, and Bing Yan. Accurate potential energy functions, non-adiabatic and spin–orbit couplings in the ZnH+ system. *Spectrochimica Acta Part A: Molecular and Biomolecular Spectroscopy*, 156:9–14, 2016. ISSN 1386-1425. doi: 10.1016/j.saa.2015.11.020.

[97] R. P. Brady, S. N. Yurchenko, G.-S. Kim, W. Somogyi, and J. Tennyson. An ab initio study of the rovibronic spectrum of sulphur monoxide (SO): Diabatic vs. adiabatic representation. *Physical Chemistry Chemical Physics*, 24(39):24076–24088, 2022. ISSN 1463-9084. doi: 10.1039/D2CP03051A.

[98] Ahren W. Jasper, Brian K. Kendrick, C. Alden Mead, and Donald G. Truhlar. Non-born-oppenheimer chemistry: Potential surfaces, couplings, and dynamics. In *Modern Trends in Chemical Reaction Dynamics*, volume Volume 14 of *Advanced Series in Physical Chemistry*, pages 329–391. WORLD SCIENTIFIC, 2004. ISBN 978-981-238-568-0. doi: 10.1142/9789812565426_0008.

[99] Yinan Shu, Zoltan Varga, Antonio Gustavo Sampaio de Oliveira-Filho, and Donald G. Truhlar. Permutationally Restrained Diabatization by Machine Intelligence. *Journal of Chemical Theory and Computation*, 17 (2):1106–1116, 2021. ISSN 1549-9618. doi: 10.1021/acs.jctc.0c01110.

[100] Tijs Karman, Matthieu Besemer, Ad van der Avoird, and Gerrit C. Groenenboom. Diabatic states, nonadiabatic coupling, and the counterpoise procedure for weakly interacting open-shell molecules. *The Journal of Chemical Physics*, 148(9):094105, 2018. ISSN 0021-9606. doi: 10.1063/1.5013091.

[101] Rovshan G. Sadygov and David R. Yarkony. On the adiabatic to diabatic states transformation in the presence of a conical intersection: A most diabatic basis from the solution to a Poisson's equation. I. *The Journal of Chemical Physics*, 109(1):20–25, 1998. ISSN 0021-9606. doi: 10.1063/1.476552.

[102] Michael Baer. Adiabatic and diabatic representations for atom-molecule collisions: Treatment of the collinear arrangement. *Chemical Physics Letters*, 35(1):112–118, 1975. ISSN 0009-2614. doi: 10.1016/0009-2614(75)85599-0.

[103] Felix T. Smith. Diabatic and Adiabatic Representations for Atomic Collision Problems. *Physical Review*, 179(1):111–123, 1969. ISSN 0031-899X. doi: 10.1103/PhysRev.179.111.

[104] C. Alden Mead and Donald G. Truhlar. Conditions for the definition of a strictly diabatic electronic basis for molecular systems. *The Journal of Chemical Physics*, 77(12):6090–6098, 1982. ISSN 0021-9606. doi: 10.1063/1.443853.

[105] Ryan P Brady, Sergei N Yurchenko, Jonathan Tennyson, and Gap-Sue Kim. ExoMol line lists – LVI. The SO line list, MARVEL analysis of experimental transition data and refinement of the spectroscopic model. *Monthly Notices of the Royal Astronomical Society*, 527(3):6675–6690, 2024. ISSN 0035-8711. doi: 10.1093/mnras/stad3508.

[106] W. Domcke and C. Woywod. Direct construction of diabatic states in the CASSCF approach. Application to the conical intersection of the $^1A_2$ and $^1B_1$ excited states of ozone. *Chemical Physics Letters*, 216(3): 362–368, 1993. ISSN 0009-2614. doi: 10.1016/0009-2614(93)90110-M.

[107] W. Domcke, C. Woywod, and M. Stengle. Diabatic CASSCF orbitals and wavefunctions. *Chemical Physics Letters*, 226(3):257–262, 1994. ISSN 0009-2614. doi: 10.1016/0009-2614(94)00726-8.

[108] David Simah, Bernd Hartke, and Hans-Joachim Werner. Photodissociation dynamics of H_2S on new coupled ab initio potential energy surfaces. *The Journal of Chemical Physics*, 111(10):4523–4534, 1999. ISSN 0021-9606. doi: 10.1063/1.479214.

[109] Hisao Nakamura and Donald G. Truhlar. The direct calculation of diabatic states based on configurational uniformity. *The Journal of Chemical Physics*, 115(22):10353–10372, 2001. ISSN 0021-9606. doi: 10.1063/1.1412879.

[110] Hisao Nakamura and Donald G. Truhlar. Direct diabatization of electronic states by the fourfold way. II. Dynamical correlation and rearrangement processes. *The Journal of Chemical Physics*, 117(12): 5576–5593, 2002. ISSN 0021-9606. doi: 10.1063/1.1500734.

[111] Hisao Nakamura and Donald G. Truhlar. Extension of the fourfold way for calculation of global diabatic potential energy surfaces of complex, multiarrangement, non-Born–Oppenheimer systems: Application to HNCO(S,S1). *The Journal of Chemical Physics*, 118(15):6816–6829, 2003. ISSN 0021-9606. doi: 10.1063/1.1540622.

[112] Abigail J. Dobbyn and Peter J. Knowles. A comparative study of methods for describing non-adiabatic coupling: Diabatic representation of the 1Sigma +/1Pi HOH and HHO conical intersections. *Molecular Physics*, 91(6):1107–1124, 1997. ISSN 0026-8976. doi: 10.1080/002689797170842.

[113] H. Köppel, J. Gronki, and S. Mahapatra. Construction scheme for regularized diabatic states. *The Journal of Chemical Physics*, 115(6): 2377–2388, 2001. ISSN 0021-9606, 1089-7690. doi: 10.1063/1.1383986.

[114] Chad E. Hoyer, Xuefei Xu, Dongxia Ma, Laura Gagliardi, and Donald G. Truhlar. Diabatization based on the dipole and quadrupole: The DQ method. *The Journal of Chemical Physics*, 141(11):114104, 2014. ISSN 0021-9606. doi: 10.1063/1.4894472.

[115] Tijs Karman, Ad van der Avoird, and Gerrit C. Groenenboom. Communication: Multiple-property-based diabatization for open-shell van der Waals molecules. *The Journal of Chemical Physics*, 144(12):121101, 2016. ISSN 0021-9606. doi: 10.1063/1.4944744.

[116] Kyoung Koo Baeck and Heesun An. Practical approximation of the non-adiabatic coupling terms for same-symmetry interstate crossings by using adiabatic potential energies only. *The Journal of Chemical Physics*, 146 (6):064107, 2017. ISSN 0021-9606. doi: 10.1063/1.4975323.

[117] D. Goorvitch. Infrared CO line list for the $X^1\Sigma^+$ state. *ApJS*, 95:535–552, 1994. doi: 10.1086/192110.

[118] J. M. Huré and E. Roueff. Analytic representations of rovibrational dipole matrix elements for the CO molecule and its isotopomers. *les annales archéologiques arabes syriennes*, 117:561–568, 1996. doi: 10.1051/aas:1996174.

[119] C. Chackerian Jr., R. Farrenq, G. Guelachvili, C. Rossetti, and W. Urban. Experimental determination of the $^1\Sigma^+$ state electric dipole moment function of carbon monoxide up to a large internuclear separation. *CJP*, 62:1579–1585, 1984. doi: 10.1139/p84-202.

[120] Stephen R. Langhoff and Charles W. Bauschlicher. Global dipole moment function for the X $^1\Sigma^+$ ground state of CO. *JCP*, 102:5220–5225, 1995. doi: 10.1063/1.469247.

[121] John A. Coxon and Photos G. Hajigeorgiou. Direct potential fit analysis of the X $^1\Sigma^+$ ground state of CO. *JCP*, 121:2992–3008, 2004. doi: 10.1063/1.1768167.

[122] W. L. Meerts, F. H. De Leeuw, and A. Dymanus. Electric and magnetic properties of carbon monoxide by molecular-beam electric-resonance spectroscopy. *classical philology*, 22:319–324, 1977. doi: 10.1016/0301-0104(77)87016-X.

[123] C. Graham, D. A. Imrie, and R. E. Raab. Measurement of the electric quadrupole moments of CO_2, CO, N_2, Cl_2 and BF_3. *MP*, 93:49–56, 1998. doi: 10.1080/002689798169429.

[124] A. D. Buckingham, R. L. Disch, and D. A. Dunmur. Quadrupole moments of some simple molecules. *Journal of the American Chemical Society*, 90(12):3104–3107, 1968. ISSN 0002-7863. doi: 10.1021/ja01014a023.

[125] Vladimir V. Meshkov, Andrey V. Stolyarov, Aleksander Yu. Ermilov, Emile S. Medvedev, Vladimir G. Ushakov, and Iouli E. Gordon. Semi-empirical ground-state potential of carbon monoxide with physical behavior in the limits of small and large inter-atomic separations. *JQSRT*, 217:262–273, 2018. doi: 10.1016/j.jqsrt.2018.06.001.

[126] Emile S. Medvedev, Vladimir V. Meshkov, Andrey V. Stolyarov, and Iouli E. Gordon. Peculiarities of high-overtone transition probabilities in carbon monoxide revealed by high-precision calculation. *JCP*, 143: 154301, 2015. doi: 10.1063/1.4933136.

[127] Sergei N. Yurchenko, Ahmed F. Al-Refaie, and Jonathan Tennyson. EXOCROSS: A general program for generating spectra from molecular line lists. *Astronomy & Astrophysics*, 614:A131, 2018. ISSN 0004-6361, 1432-0746. doi: 10.1051/0004-6361/201732531.

[128] J.M. Brown, J.T. Hougen, K.-P. Huber, J.W.C. Johns, I. Kopp, H. Lefebvre-Brion, A.J. Merer, D.A. Ramsay, J. Rostas, and R.N. Zare. The labeling of parity doublet levels in linear molecules. *Journal of Molecular Spectroscopy*, 55(1-3):500–503, 1975. ISSN 00222852. doi: 10.1016/0022-2852(75)90291-X.

[129] Rainer Weiss. Stark effect and hyperfine structure of hydrogen fluoride. *PR*, 131:659–665, 1963. doi: 10.1103/PhysRev.131.659.

[130] F. H. de Leeuw and A. Dymanus. Magnetic properties and molecular quadrupole moment of HF and HCl by molecular-beam electric-resonance spectroscopy. *JMS*, 48:427–445, 1973. doi: 10.1016/0022-2852(73)90107-0.

[131] James F. Harrison. Dipole and quadrupole moment functions of the hydrogen halides HF, HCl, HBr, and HI: A Hirshfeld interpretation. *JCP*, 128:114320, 2008. doi: 10.1063/1.2897445.

[132] Andrzej J. Sadlej. Medium-size polarized basis sets for high-level correlated calculations of molecular electric properties. *Collection of Czechoslovak Chemical Communications*, 53(9):1995–2016, 1988. ISSN 1212-6950, 0010-0765. doi: 10.1135/cccc19881995.

[133] B. F. Minaev. Effect of spin-orbit coupling on the intensity of magnetic dipole transitions in molecular oxygen. *Soviet Physics Journal*, 21(9): 1205–1209, 1978. ISSN 1573-9228. doi: 10.1007/BF00894576.

[134] B. F. Minaev. Intensities of spin-forbidden transitions in molecular oxygen and selective heavy-atom effects. *International Journal of Quantum Chemistry*, 17(2):367–374, 1980. ISSN 1097-461X. doi: 10.1002/qua.560170219.

[135] T K Balasubramanian and Omana Narayanan. Magnetic dipole and electric quadrupole line strengths for the atmospheric oxygen ($b^1\Sigma_g^+$ $X^3\Sigma_g^-$) system. *Acta Physica Hungarica*, 74(4):341–353, 1994.

[136] A. P. Mishra, T. K. Balasubramanian, and B. J. Shetty. Generalized electric quadrupole branch linestrengths for the $a^1\Delta_g$–$X^3\Sigma_g^-$ infrared atmospheric oxygen bands. *Journal of Quantitative Spectroscopy and Radiative Transfer*, 112(14):2303–2309, 2011. ISSN 0022-4073. doi: 10.1016/j.jqsrt.2011.05.013.

[137] Boris F. Minaev, N. Arul Murugan, and Hans Ågren. Dioxygen spectra and bioactivation. *International Journal of Quantum Chemistry*, 113 (14):1847–1867, 2013. ISSN 1097-461X. doi: 10.1002/qua.24390.

[138] J. F. Noxon. Observation of the ($b^1\Sigma_g^+$–$X^3\Sigma_g^-$) transition in O_2. *Canadian Journal of Physics*, 39(8):1110–1119, 1961. ISSN 0008-4204. doi: 10.1139/p61-126.

[139] E. H. Fink, H. Kruse, D. A. Ramsay, and M. Vervloet. An electric quadrupole transition: The emission system of oxygen. *Canadian Journal of Physics*, 64(3):242–245, 1986. ISSN 0008-4204. doi: 10.1139/p86-044.

[140] D. A. Long, D. K. Havey, M. Okumura, H. M. Pickett, C. E. Miller, and J. T. Hodges. Laboratory measurements and theoretical calculations of O_2 *A* band electric quadrupole transitions. *Physical Review A*, 80(4): 042513, 2009. doi: 10.1103/PhysRevA.80.042513.

[141] Rainer Klotz and Sigrid D. Peyerimhoff. Theoretical study of the intensity of the spin- or dipole forbidden transitions between the $c^1\Sigma^-_u$, A' $^3\Delta_u$, A $^3\Sigma^+_u$ and X $^3\Sigma^-_g$, $a^1\Delta_g$, $b^1\Sigma^+_g$ states in O_2. *Molecular Physics*, 1986. doi: 10.1080/00268978600100421.

[142] L. Veseth. Spin-orbit and spin-other-orbit interaction in diatomic molecules. *Theoretica chimica acta*, 18(4):368–384, 1970. ISSN 1432-2234. doi: 10.1007/BF00526455.

[143] L Veseth. Spin-rotation interaction in diatomic molecules. *Journal of Physics B: Atomic and Molecular Physics*, 4(1):20–27, 1971. ISSN 0022-3700. doi: 10.1088/0022-3700/4/1/005.

[144] W. G. (William Graham) Richards, H. P. Trivedi, and D. L. Cooper. *Spin-Orbit Coupling in Molecules*. International Series of Monographs on Chemistry. Clarendon Press and Oxford University Press, 1981.

[145] Laimutis Bytautas, Nikita Matsunaga, and Klaus Ruedenberg. Accurate ab initio potential energy curve of O_2. II. Core-valence correlations, relativistic contributions, and vibration-rotation spectrum. *The Journal of Chemical Physics*, 132(7):074307, 2010. ISSN 0021-9606. doi: 10.1063/1.3298376.

[146] Laimutis Bytautas and Klaus Ruedenberg. Accurate ab initio potential energy curve of O_2. I. Nonrelativistic full configuration interaction valence correlation by the correlation energy extrapolation by intrinsic scaling method. *The Journal of Chemical Physics*, 132(7):074109, 2010. ISSN 0021-9606. doi: 10.1063/1.3298373.

[147] Masao Kotani, Yukio Mizuno, Kunihusa Kayama, and Eiichi Ishiguro. Electronic Structure of Simple Homonuclear Diatomic Molecules I. Oxygen Molecule. *Journal of the Physical Society of Japan*, 12(6):707–736, 1957. ISSN 0031-9015. doi: 10.1143/JPSJ.12.707.

[148] Sunil Sarangi and Prasad Varanasi. On the determination of the quadrupole moment of oxygen from self-broadened line widths in the microwave spectrum. *Journal of Quantitative Spectroscopy and Radiative Transfer*, 14(10):989–993, 1974. ISSN 0022-4073. doi: 10.1016/0022-4073(74)90082-X.

[149] Massimiliano Bartolomei, Estela Carmona-Novillo, Marta I. Hernández, José Campos-Martínez, and Ramón Hernández-Lamoneda. Long-range interaction for dimers of atmospheric interest: Dispersion, induction and electrostatic contributions for O_2–O_2, N_2–N_2 and O_2–N_2. *Journal of Computational Chemistry*, 32(2):279–290, 2011. ISSN 1096-987X. doi: 10.1002/jcc.21619.

[150] Vincent W. Couling and Siyabonga S. Ntombela. The electric quadrupole moment of O_2. *Chemical Physics Letters*, 614:41–44, 2014. ISSN 0009-2614. doi: 10.1016/j.cplett.2014.09.006.

[151] D. B. Lawson and J. F. Harrison. Distance Dependence and Spatial Distribution of the Molecular Quadrupole Moments of H_2, N_2, O_2, and F_2. *The Journal of Physical Chemistry A*, 101(26):4781–4792, 1997. ISSN 1089-5639. doi: 10.1021/jp9703420.

[152] E. Richard Cohen and George Birnbaum. Influence of the potential function on the determination of multipole moments from pressure-induced far-infrared spectra. *The Journal of Chemical Physics*, 66(6):2443–2447, 1977. ISSN 0021-9606. doi: 10.1063/1.434283.

[153] George Birnbaum and E. Richard Cohen. Determination of molecular multipole moments and potential function parameters of non-polar molecules from far infra-red spectra. *Molecular Physics*, 32(1):161–167, 1976. ISSN 0026-8976. doi: 10.1080/00268977600101691.

[154] Myron Evans. Some equations for multipole-induced dipole absorption in linear molecules. *Molecular Physics*, 29(5):1345–1351, 1975. ISSN 0026-8976. doi: 10.1080/00268977500101171.

[155] Robert J. Le Roy, Yiye Huang, and Calvin Jary. An accurate analytic potential function for ground-state N_2 from a direct-potential-fit analysis of spectroscopic data. *The Journal of Chemical Physics*, 125(16):164310, 2006. ISSN 0021-9606. doi: 10.1063/1.2354502.

[156] Robert J. Le Roy, Nikesh S. Dattani, John A. Coxon, Amanda J. Ross, Patrick Crozet, and Colan Linton. Accurate analytic potentials for $Li_2(XX^1\Sigma_g{}^+)$ and $Li_2(A^1\Sigma_u{}^+)$ from 2 to 90 Å, and the radiative lifetime of Li(2p). *The Journal of Chemical Physics*, 131(20):204309, 2009. ISSN 0021-9606. doi: 10.1063/1.3264688.

[157] W. Rijks, M. van Heeringen, and P. E. S. Wormer. The frequency-dependent polarizability of O_2 and the dispersion interaction in dimers containing O_2 from a single, double, triple configuration interaction perturbation approach. *The Journal of Chemical Physics*, 90(11):6501–6506, 1989. ISSN 0021-9606. doi: 10.1063/1.456316.

[158] Paul H. Krupenie. The Spectrum of Molecular Oxygen. *Journal of Physical and Chemical Reference Data*, 1(2):423–534, 1972. ISSN 0047-2689. doi: 10.1063/1.3253101.

[159] Laxmi Prajapat, Pawel Jagoda, Lorenzo Lodi, Maire N. Gorman, Sergei N. Yurchenko, and Jonathan Tennyson. ExoMol molecular line lists - XXIII. Spectra of PO and PS. *Monthly Notices of the Royal Astronomical Society*, 472:3648–3658, 2017. doi: 10.1093/mnras/stx2229.

[160] Mikhail Semenov, Nicholas Clark, Sergei N Yurchenko, Gap-Sue Kim, and Jonathan Tennyson. ExoMol line lists - XLVI. Empirical rovibronic spectra of silicon mononitrate (SiN) covering the six lowest electronic states and four isotopologues. *Monthly Notices of the Royal Astronomical Society*, 516:1158–1169, 2022. doi: 10.1093/mnras/stac2004.

[161] Sergei N Yurchenko, Emma Nogué, Ala'a A A Azzam, and Jonathan Tennyson. ExoMol line lists - XLVII. Rovibronic spectrum of aluminium monochloride (AlCl). *Monthly Notices of the Royal Astronomical Society*, 520(4):5183–5191, 2022. doi: 10.1093/mnras/stac3757.

[162] Emile S. Medvedev and Vladimir G. Ushakov. Irregular semi-empirical dipole-moment function for carbon monoxide and line lists for all its isotopologues verified for extremely high overtone transitions. *Journal of Quantitative Spectroscopy and Radiative Transfer*, 288:108255, 2022. ISSN 0022-4073. doi: 10.1016/j.jqsrt.2022.108255.

[163] M. Tinkham and M. W. P. Strandberg. Theory of the Fine Structure of the Molecular Oxygen Ground State. *Physical Review*, 97(4):937–951, 1955. doi: 10.1103/PhysRev.97.937.

[164] M. Tinkham and M. W. P. Strandberg. Interaction of Molecular Oxygen with a Magnetic Field. *Physical Review*, 97(4):951–966, 1955. doi: 10.1103/PhysRev.97.951.

[165] Marco Pezzella, Jonathan Tennyson, and Sergei N Yurchenko. ExoMol photodissociation cross-sections – I. HCl and HF. *Monthly Notices of the Royal Astronomical Society*, 514(3):4413–4425, 2022. ISSN 0035-8711. doi: 10.1093/mnras/stac1634.

[166] Sergei N Yurchenko, Wojciech Szajna, Rafał Hakalla, Mikhail Semenov, Andrei Sokolov, Jonathan Tennyson, Robert R Gamache, Yakiv Pavlenko, and Mirek R Schmidt. ExoMol line lists – LIV. Empirical line lists for AlH and AlD and experimental emission spectroscopy of AlD in A1Π (v = 0, 1, 2). *Monthly Notices of the Royal Astronomical Society*, 527(4):9736–9756, 2024. ISSN 0035-8711. doi: 10.1093/mnras/stad3802.

[167] I. E. Gordon, L. S. Rothman, R. J. Hargreaves, R. Hashemi, E. V. Karlovets, F. M. Skinner, E. K. Conway, C. Hill, R. V. Kochanov, Y. Tan, P. Wcisło, A. A. Finenko, K. Nelson, P. F. Bernath, M. Birk, V. Boudon, A. Campargue, K. V. Chance, A. Coustenis, B. J. Drouin, J. M. Flaud, R. R. Gamache, J. T. Hodges, D. Jacquemart, E. J. Mlawer, A. V. Nikitin, V. I. Perevalov, M. Rotger, J. Tennyson, G. C. Toon, H. Tran, V. G. Tyuterev, E. M. Adkins, A. Baker, A. Barbe, E. Canè, A. G. Császár, A. Dudaryonok, O. Egorov, A. J. Fleisher, H. Fleurbaey, A. Foltynowicz, T. Furtenbacher, J. J. Harrison, J. M. Hartmann, V. M. Horneman, X. Huang, T. Karman, J. Karns, S. Kassi, I. Kleiner, V. Kofman, F. Kwabia–Tchana, N. N. Lavrentieva, T. J. Lee, D. A. Long, A. A. Lukashevskaya, O. M. Lyulin, V. Yu. Makhnev, W. Matt, S. T. Massie, M. Melosso, S. N. Mikhailenko, D. Mondelain, H. S. P.

Müller, O. V. Naumenko, A. Perrin, O. L. Polyansky, E. Raddaoui, P. L. Raston, Z. D. Reed, M. Rey, C. Richard, R. Tóbiás, I. Sadiek, D. W. Schwenke, E. Starikova, K. Sung, F. Tamassia, S. A. Tashkun, J. Vander Auwera, I. A. Vasilenko, A. A. Vigasin, G. L. Villanueva, B. Vispoel, G. Wagner, A. Yachmenev, and S. N. Yurchenko. The HITRAN2020 molecular spectroscopic database. *Journal of Quantitative Spectroscopy and Radiative Transfer*, 277:107949, 2022. ISSN 0022-4073. doi: 10.1016/j.jqsrt.2021.107949.

[168] Tibor Furtenbacher, Attila G. Császár, and Jonathan Tennyson. MARVEL: Measured active rotational–vibrational energy levels. *Journal of Molecular Spectroscopy*, 245(2):115–125, 2007. ISSN 00222852. doi: 10.1016/j.jms.2007.07.005.

[169] Marie-France Mérienne, Alain Jenouvrier, Bernard Coquart, Michel Carleer, Sophie Fally, Reginald Colin, A. C. Vandaele, and Christian Hermans. Improved Data Set for the Herzberg Band Systems of $^{16}O_2$. *Journal of Molecular Spectroscopy*, 207(1):120, 2001. ISSN 0022-2852. doi: 10.1006/jmsp.2001.8314.

[170] K. Yoshino, J. R. Esmond, W. H. Parkinson, A. P. Thorne, R. C. M. Learner, G. Cox, and A. S.-C. Cheung. Fourier transform spectroscopy and cross section measurements of the Herzberg III bands of O_2 at 295 K. *The Journal of Chemical Physics*, 112(22):9791–9801, 2000. ISSN 0021-9606. doi: 10.1063/1.481702.

[171] Shanshan Yu, Brian J. Drouin, and Charles E. Miller. High resolution spectral analysis of oxygen. IV. Energy levels, partition sums, band constants, RKR potentials, Franck-Condon factors involving the $X^3\Sigma_g^-$, $a^1\Delta_g$ and $b^1\Sigma_g^+$ states. *The Journal of Chemical Physics*, 141(17): 174302, 2014. ISSN 0021-9606. doi: 10.1063/1.4900510.

[172] P. W. Atkins and Ronald Friedman. *Molecular Quantum Mechanics*. Oxford University Press, New York, 4th ed edition, 2005. ISBN 978-0-19-927498-7.

[173] Igor V. Khudyakov and Boris F. Minaev. Molecular Terms of Dioxygen and Nitric Oxide. *Physchem*, 1(2):121–132, 2021. ISSN 2673-7167. doi: 10.3390/physchem1020008.

[174] Jonathan Tennyson, Christian Hill, and Sergei N. Yurchenko. Data structures for ExoMol: Molecular line lists for exoplanet and other atmospheres. *AIP Conference Proceedings*, 1545(1):186–195, 2013. ISSN 0094-243X. doi: 10.1063/1.4815853.

[175] C Dorn, J H D Harrison, A Bonsor, and T O Hands. A new class of Super-Earths formed from high-temperature condensates: HD219134 b, 55 Cnc e, WASP-47 e. *Monthly Notices of the Royal Astronomical Society*, 484(1):712–727, 2019. ISSN 0035-8711. doi: 10.1093/mnras/sty3435.

[176] T Giang Nguyen, Nicolas B Cowan, Agnibha Banerjee, and John E Moores. Modelling the atmosphere of lava planet K2-141b: Implications for low- and high-resolution spectroscopy. *Monthly Notices of the Royal Astronomical Society*, 499(4):4605–4612, 2020. ISSN 0035-8711. doi: 10.1093/mnras/staa2487.

[177] Samson J. Mercier, Lisa Dang, Alexander Gass, Nicolas B. Cowan, and Taylor J. Bell. Revisiting the Iconic Spitzer Phase Curve of 55 Cancri e: Hotter Dayside, Cooler Nightside, and Smaller Phase Offset. *The Astronomical Journal*, 164(5):204, 2022. ISSN 1538-3881. doi: 10.3847/1538-3881/ac8f22.

[178] W. Somogyi, S. N. Yurchenko, and A. Yachmenev. Calculation of electric quadrupole linestrengths for diatomic molecules: Application to the H_2, CO, HF, and O_2 molecules. *The Journal of Chemical Physics*, 155(21):214303, 2021. ISSN 0021-9606, 1089-7690. doi: 10.1063/5.0063256.

[179] Paola Marigo, Bernhard Aringer, Léo Girardi, and Alessandro Bressan. Updated Low-temperature Gas Opacities with ÆSOPUS 2.0. *The Astrophysical Journal*, 940(2):129, 2022. ISSN 0004-637X. doi: 10.3847/1538-4357/ac9b40.

[180] A. L. Zerkle and S. Mikhail. The geobiological nitrogen cycle: From microbes to the mantle. *Geobiology*, 15(3):343–352, 2017. ISSN 1472-4669. doi: 10.1111/gbi.12228.

[181] Helmut Lammer, Laurenz Sproß, John Lee Grenfell, Manuel Scherf, Luca Fossati, Monika Lendl, and Patricio E. Cubillos. The Role of N_2 as a Geo-Biosignature for the Detection and Characterization of Earth-like Habitats. *Astrobiology*, 19(7):927–950, 2019. ISSN 1557-8070. doi: 10.1089/ast.2018.1914.

[182] Sawyer Hall, Joshua Krissansen-Totton, Tyler Robinson, Arnaud Salvador, and Jonathan J. Fortney. Constraining Background N_2 Inventories on Directly Imaged Terrestrial Exoplanets to Rule Out O_2 False Positives. *The Astronomical Journal*, 166(6):254, 2023. ISSN 1538-3881. doi: 10.3847/1538-3881/ad03e9.

[183] S. Seager, J. Huang, J. J. Petkowski, and M. Pajusalu. Laboratory studies on the viability of life in H_2-dominated exoplanet atmospheres.

Nature Astronomy, 4(8):802–806, 2020. ISSN 2397-3366. doi: 10.1038/s41550-020-1069-4.

[184] Quentin Changeat. On Spectroscopic Phase-curve Retrievals: H_2 Dissociation and Thermal Inversion in the Atmosphere of the Ultrahot Jupiter WASP-103 b. *The Astronomical Journal*, 163(3):106, 2022. ISSN 1538-3881. doi: 10.3847/1538-3881/ac4475.